Science
AAAS

Supplementary Materials for

Trends in serotype-specific immunity explain the incidence patterns of diseases caused by human enteroviruses

Margarita Pons-Salort, Nicholas C. Grassly

Correspondence to: m.pons-salort@imperial.ac.uk

This PDF file includes:

S1 Materials and methods

S1.1 Epidemiological data

The National Epidemiological Surveillance of Infectious Diseases (NESID) in Japan consists of a laboratory-based surveillance system for pathogen reporting, and a disease-based surveillance system for patient reporting. A detailed description of NESID, including its structure and diseases covered can be found in *(20)*.

The Japanese enterovirus sentinel surveillance system isolates and identifies enteroviruses from specimens of patients diagnosed with four target diseases representative of enterovirus infections: aseptic meningitis, hand-foot-and-mouth disease (HFMD), herpangina and acute haemorrhagic conjunctivitis (AHC), although sometimes specimens from other severe cases (e.g. with encephalitis or myocarditis) or from patients with minor illnesses (e.g. with upper respiratory tract inflammation or fever) are also included *(9)*. In 2000, the disease-based sentinel system counted about 460 sentinel points for the surveillance of aseptic meningitis *(21)*, about 3,000 for the surveillance of pediatric diseases (including HFMD and herpangina) *(22)*, and 625 for the surveillance of ophthalmic diseases (including AHC), but these numbers slightly increased between 2000 and 2014 (Fig. S1). The number of cases of each disease diagnosed through the disease sentinel sites is shown in Fig. S2. All sentinel sites for the surveillance of aseptic meningitis, but only about 10% of sentinel sites for the surveillance of HFMD, herpangina and AHC are pathogen sentinels *(20,23)*. This means that specimens from cases of aseptic meningitis diagnosed in all sentinel sites, and only specimens from cases of HFMD, herpangina and AHC diagnosed in about 10% of the sentinel sites for these diseases are tested for infectious agents *(20)*. The clinical specimens from which enteroviruses are mostly isolated are nasopharyngeal, stool and cerebrospinal fluid (CSF), and the number and type of samples collected is performed on an ad-hoc basis (there is no systematic sampling). In addition, severe or unusual cases may be more likely to be submitted for laboratory testing. Positive results for virus isolation and typing are reported to the Central Infectious Disease Surveillance Center, at the National Institute of Infectious Diseases (NIID).

The National Institute of Infectious Diseases (NIID) issues an Infectious Agents Surveillance Report (IASR) on a monthly basis to publish information acquired through the NESID. Here, we extracted the number of serotype-specific enterovirus isolations from clinical samples reported each month in Japan from January 2000 to December 2016 from the IASR and available at https://www.niid.go.jp/niid/ja/iasr.html. Note that for simplicity, we use the word "incidence" to refer to notification rates of serotype-specific enterovirus isolations.

A list of all the non-polio enterovirus serotypes reported between January 2000 and December 2014, with the total number of isolations and their species is given in Table S1.

S1.2 Demographic data

Estimates of the annual number of births, deaths and population size were obtained from the Japan Statistical Yearbook 2016 report provided by the Bureau of Statistics of Japan and available at http://www.stat.go.jp *(24)*. Those values were used to estimate annual birth and death rates, by dividing the estimates of the total number of live births and deaths in a given year by the population size of that year. Annual birth and death rates were smoothed using splines to obtain the covariates for the transmission model (Fig. S3).

S1.3 Wavelet analysis

To detect the period of long-term cycles (periodicities equal and above the annual seasonality, i.e. $\geq$12 months) in the time series of reported serotype-specific enterovirus isolations, we did a wavelet analysis of the square-root–transformed time-series (Fig. S7 – Fig. S9). We used the Morlet wavelet, as it has been classically done for the analysis of epidemiological data *(25)*. This analysis was performed using the "WaveletComp" R package *(26)*.

S1.4 Transmission and observation models

We implemented a classic susceptible-infected-recovered (SIR) stochastic transmission model and fit it to the monthly number of reported isolations of individual enterovirus serotypes in Japan from January 2000 to December 2014. We fitted the model independently to the data for the following serotypes: CV-A2, 4, 5, 6, 9, 10, 16, EV-A71, CV-B1 – 5, E3, 6, 9, 11, 18, 25 and 30, which are the 20 most prevalent serotypes with >1 peak of activity during the study period. In the SIR model individuals become permanently immune after infection and thus reinfection with the same serotype cannot occur (acquisition of the virus is no longer possible). The model also accounts for: a) seasonality of enterovirus transmission, modeled with a sinusoidal transmission rate; b) time-varying birth and death rates ($\mu(t)$ and $m(t)$, respectively); and c) a proportion of asymptomatic infections, and under-reporting of cases, to account for the fact that only the cases picked up at pathogen-sentinel sites are reported. We also assume a constant background level of exposure to infection outside Japan, ω, to allow for reintroduction of infection following possible local stochastic extinction. For simplicity, we present the deterministic version of the transmission model, described by the following set of differential equations:

$$\begin{aligned}
\frac{dS}{dt} &= \mu(t)N - \lambda(t)S - m(t)S \\
\frac{dI}{dt} &= \lambda(t)S - \gamma I - m(t)I \\
\frac{dR}{dt} &= \gamma I - m(t)R \\
\lambda(t) &= \beta_m \left(1 + \beta_s \cos\left(2\pi\left(t + \phi\right)\right)\right) \frac{I + \omega}{N}
\end{aligned}$$

where $1/\gamma$ is the average duration of the infectious period, β_m is the average transmission rate, β_s is the amplitude of the transmission rate, and ϕ is the phase of the transmission rate, which determines the timing of the annual seasonal peak of transmission. $\lambda(t)$ is the so-called force of infection, and the variables S, I, R and N describe the number of susceptible, infected, recovered and total population size, respectively over time (although time has been omitted for notational clarity), and $N = S + I + R$.

We used a version of the above model that accounts for demographic stochasticity and that was implemented as a Markov process using a modification of the tau-leap algorithm *(27)* based on a multinomial distribution, as described in *(28)*, and using a simulation time step of one day.

Given that a large proportion of enterovirus infections are known to be asymptomatic, and among the cases, only those captured by the pathogen-sentinel sites have the serotype reported, we needed an observation model to link the output of the transmission model (number of newly infected individuals) to the data (reported isolations of enterovirus serotype). The reporting period of the data, Δt, is one month. Because the number of reported enterovirus isolations over the total number of infections is supposed to be small, we modeled the number of monthly isolations of enterovirus with a Poisson distribution:

$$\text{EV-serotype isolations in } \Delta t \sim \text{Poisson}\left(\rho \times C_{\Delta t}\right)$$

where ρ is the reporting probability per infection, which is the product of the case-to-infection ratio (i.e. the probability of an infected individual to become symptomatic) times the probability that a case is captured by the pathogen-sentinel surveillance system (which implicitly accounts for sensitivity and specificity of lab tests). The variable $C_{\Delta t}$ is the total number of new infections during Δt (one month).

The initial conditions were parameterized as follows: $S(t_0) = s_0 N(t_0)$, $I(t_0) = i_0 N(t_0)$, and $R(t_0) = (1 - s_0 - i_0)N(t_0)$, where s_0 and i_0 are the respective proportions of individuals susceptible and infected in the whole population at t_0, and were estimated. We fixed the population size at t_0 ($N(t_0) = 126,931,430$) and used the estimates of birth and death rates to simulate the changes in the population during the study period. The model-based and reported population size were closely aligned over time (Fig. S10).

The model was implemented using the R-package "pomp" *(29)*.

S1.5 Inference framework

For each enterovirus serotype, we fitted the transmission model described above to the time-series of monthly number of reported isolations. Because the duration of infectiousness is known to be highly corre-

lated with the transmission rate, we set it at $1/\gamma = 7$ days for all the serotypes based on studies on wild-type poliovirus and in agreement with trends in the quantity of virus shed over time since infection *(30)*. For each serotype, we estimated six parameters: β_m, β_s, ω, ρ, s_0 and i_0.

To estimate the parameters, we first constrained the parameter space using trajectory matching with 40,000 starting parameter combinations that were drawn using Latin Hypercube Sampling over large ranges for the parameter values. The best parameter combinations from trajectory matching were used to define the range of plausible values to draw 1,000 new parameter combinations to start the maximum iterating filtering (MIF) procedure based on sequential Monte Carlo *(11)* (specifically, we used the IF2 algorithm *(11)*). This procedure was performed 2 more times with 1,000 new starting parameter combinations each on a more constrained parameter space, and by fixing the value of ϕ to the best value obtained in the first round of maximum iterated filtering. The value of ϕ always fell between 0.65 and 0.75, in agreement with a peak of transmission occurring during August or September. The log-likelihood was computed as the log of the mean likelihoods of 10 replicate filters, each with 10,000 particles.

For the particle filtering, we used 10,000 particles and 300 MIF iterations. One round of the particle filtering with these parameters lasted on average between 5 and 9 hours of CPU time depending on the serotype. All the computations were run on the Imperial College High Performance Computing (https://www.imperial.ac.uk/admin-services/ict/self-service/research-support/hpc/).

To obtain approximate 99% confidence intervals of the parameters, we used the profile log-likelihood and followed the method in *(31)* to account for Monte Carlo uncertainty (Table S3 and Fig. S35 – Fig. S54). As for the parameter estimates, to construct the profiles we used the value of the log of the mean likelihoods of 10 replicate filters, each with 10,000–40,000 particles (depending on the parameter and the serotype).

S1.6 Model extensions: change in viral properties

We implemented three extensions of the SIR model above to account for three different changes in viral properties at a certain point in time t_c: i) a change in transmissibility, ii) a change in pathogenicity, and iii) a change in antigenicity. The change in transmissibility was modelled as follows:

$$\beta_m := \begin{cases} \beta_m, & \text{if } t < t_c \\ c_\beta \beta_m, & \text{if } t \geq t_c \end{cases}$$

where $c_\beta > 0$. Similarly, the change in pathogenicity was modelled as:

$$\rho := \begin{cases} \rho, & \text{if } t < t_c \\ c_\rho \rho, & \text{if } t \geq t_c \end{cases}$$

with $c_\rho > 0$. The change in antigenicity was modelled as an increase in the number of susceptible individuals at time t_c taken as a proportion $c_a \in [0, 1]$ of recovered individuals at that time:

$$\begin{cases} R(t_c) & := (1 - c_a) R(t_c) \\ S(t_c) & := S(t_c) + c_a R(t_c) \end{cases}$$

Note that the changes in transmissibility and antigenicity affect the transmission dynamics, whereas the change in pathogenicity only affects the observation model, but not the transmission dynamics. In addition, the three model extensions have 2 more parameters than the SIR model described above (the point in time when the change happens, t_c, and the parameter describing that change, either c_β, c_ρ or c_a), and so the three model extensions have the same complexity.

We used these model extensions to explore whether a change in transmissibility, pathogenicity or antigenicity alone could explain the dynamics of CV-A6 and E18, which were not well explained with the SIR model over the entire 15-year period.

S1.7 Waning immunity

We assumed that acquired homotypic immunity was life-long, but it is likely to wane over time, based on observations on mucosal immunity to poliovirus *(17)*. To test whether waning immunity was compatible with births-driven dynamics, we extended our model in Section S1.4 to account for the possibility of waning immunity, and therefore, allow for re-infection with the same serotype. The model with waning immunity (SIRS) has one more component than the SIR model, which describes the transition of immune individuals to susceptible, and it is given by the following set of differential equations:

$$\begin{aligned}\frac{dS}{dt} &= \mu(t)N - \lambda(t)S - m(t)S + \delta R \\ \frac{dI}{dt} &= \lambda(t)S - \gamma I - m(t)I \\ \frac{dR}{dt} &= \gamma I - m(t)R - \delta R\end{aligned}$$

where δ is the rate of waning immunity, and therefore, $1/\delta$ is the average duration of protective immunity against infection.

We fitted this model to the data for the 18 serotypes for which the SIR model without changes in viral properties explained the data well (all, except CV-A6 and E18). The model fits to the data and the MLEs of the parameters are given in Fig. S62 and Fig. S63, and Table S5, respectively.

S1.8 Out-of-sample predictions

To further test whether our models accounted for the epidemiological mechanisms necessary to explain the observed incidence patterns, we did out-of-sample predictions over the two years after the fitting period (i.e. January 2015 – December 2016), simulating forward from the initial conditions over 17 years (Figs. 2 to 4), and also using the particle filter to reconstruct the state space variables up to December 2014 and simulating the model forward after that (Fig. S57).

Birth and death rates in the "predictive period" (2015–2016) were extrapolated using the default function implemented in "pomp" *(29)*, which is linear extrapolation.

S2 Supplementary Text

S2.1 Description of demographic data

The variation of the demographic variables (population size, live births, deaths, and birth and death rates) over the study period is shown in Fig. S3. Overall, live births declined from 1,194,000 in 2000 to 1,023,000 in 2014, with a small increase between 2005 and 2008, whereas the number of deaths increased regularly from 968,000 in 2000 to 1,274,000 in 2014. These opposite changes in births and deaths resulted in an inflection in the population size that increased from 126,926,000 in 2000 to 128,084,000 in 2008, remained fairly constant until 2010, and then decreased, reaching 127,083,000 in 2014. Changes in birth and death rates followed a pattern similar to the number of births and deaths respectively.

S2.2 Description of epidemic patterns

The time-series of the monthly number of reported non-polio enterovirus isolations (all non-polio enterovirus serotypes combined) from January 2000 to December 2014 displays a regular pattern (Figure 1A), with a peak of cases each year in summer, and with an annual number of enterovirus isolations ranging between 1,787 in 2009 and 4,433 in 2002, with a mean of 2,844 (IQR 2,195 – 3,336).

For all the serotypes with >500 isolations reported during the study period (January 2000 and December 2014), their time-series of the monthly number of reported isolations are shown in Fig. S4 – Fig. S6. Those serotypes include CV-A2, 4, 5, 6, 10, 16 and EV-A71 that belong to species A, and CV-A9, CV-B1 – 5, E3, 6, 7, 9, 11, 13, 18, 25, and 30 that belong to species B. Note that the few serotypes in species C and D were isolated a small number of times (<300 each) during the study period (Table S1).

In order to identify periodicities equal and above the annual seasonality in the time-series of serotype-specific enterovirus isolations and their possible changes over time (regime shifts), we performed a wavelet analysis of each time series (Fig. S7 – Fig. S9).

Generally, the Coxsackievirus A serotypes, and EV-A71 showed, in addition to the 1-year band, regular patterns with periods above 1 year, including 2 and 3-year cycles (Fig. S4 and Fig. S7). CV-A2 exhibited a 2-year cycle; CV-A4 transitioned from a 1-year cycle during 2000 – 2004 to a 2-year cycle with higher peaks during 2004 – 2014; CV-A5 and CV-A6 showed a 2-year cycle by the end of the period; CV-A10 had a 3-year cycle at the beginning that switched to a 2-year cycle after 2003; CV-A16 transitioned from a 1-year cycle during 2000 – 2008 to a 3-year cycle after that; CV-A9 (which belongs to species B) also transitioned from a 1-year cycle during 2000 – 2006 to a 3-year cycle from 2006 onwards; and EV-A71 showed a constant 3-year cycle over the study period.

The number of isolations of Coxsackievirus B serotypes were generally smaller than Coxsackievirus A serotypes, with <2000 isolations reported over the study period per serotype (Table S1), and always <100 per month. The wavelets for Coxsackievirus B serotypes (Fig. S8) had a clear band at 1 year, interrupted at some points because of the small number or absence of reports for CV-B1, CV-B2 and CV-B5 (Fig. S5), and a less clear band around 3 – 4 years that was not apparent for CV-B4, which maintained a regular and clear 1-year period.

Echoviruses showed more irregular patterns than Coxsackievirus A and B serotypes, most of them including periods with consecutive months or years with no or a small number of isolations reported (Fig. S6), which was rarely the case for Coxsackieviruses A and B. For some echovirus serotypes (including E3, 6, 9, 18, 25, and 30), the one-year seasonal cycle was clear over some periods of time (Fig. S9), whereas multi-annual cycles were not apparent, except perhaps for Echovirus 3 (with a 4-year cycle at the beginning that increased later) and Echovirus 9 (with a 2 – 3 year cycle). Echovirus 13 had a single and big peak of activity in 2002 (reporting >800 reports in a single month); Echovirus 7 displayed two short periods of activity, one around 2004 – 2005 and another around 2012 – 2013; and Echovirus 11 also had two periods of activity, one with three consecutive and increasing peaks between 2000 and 2002, which were followed by twelve years with rare detections, and then another peak in 2014.

S2.3 Variability among stochastic realizations of the model

Accounting for stochastic demography may be important if the system is sensitive to fluctuations in the number of susceptible and/or infected individuals, and it can push the system into different dynamics that in particular can differ from the deterministic behaviour, but may be more realistic. In the time-series analysed here, stochastic demography can play an important role when the number of infected individuals becomes small, which happens during the troughs (which roughly correspond to winter months) and during years with no or a small number of cases (i.e. in time-series with multi-annual cycles or irregular patterns). In those time points, stochasticity may determine whether a next epidemic will take off or not, or whether the virus will go extinct. We have allowed for a constant exposure to infection outside of Japan ($w > 0$, estimated) to account for the fact that the system is not closed and that infection may be reintroduced from elsewhere.

Models accounting for demographic stochasticity result in some variability between simulated realizations with the same parameter values. To analyse this variability, for each serotype we simulated the model 100 times with the maximum likelihood estimates (MLE) of the parameters and computed the sum of squared residuals (SSR) for each of the stochastic realizations. This approach is similar to the likelihood of the simulations given the data (Fig. S32). The histogram of the SSR (Fig. S31), the increasing curve of it (Fig. S33) and the distribution of the likelihood of the simulations (Fig. S32) all give an idea of the variability between simulations for a given serotype, and whether all the simulations stay in a similar regime behaviour, or they enter more than one different dynamics. A full exploration of a subset of trajectories (taken as multiples of ten in the rank of their increasing SSR, Fig. S11 – Fig. S30), allows to visually identify whether there are critical points in the dynamics where the simulations diverge into different behaviour regimes.

For example, for CV-A4, about 80% of the simulations had a small and similar SSR, whereas the remaining 20% had a much bigger SSR (Fig. S33). When looking at the full trajectories of the simulations ordered by increasing SSR, we can see that the first 8 plots (i.e. those corresponding to the first 80% of the simulations) fit the data well, whereas the last two (i.e. those corresponding to the last 20%) have a pattern that is in anti-phase with the data from around 2005 onwards (Fig. S12). That is, the estimated parameter values correctly predict a regime shift from a one year-cycle to a two-year cycle, but for about 20% of the simulations, this shift does not occur at the observed time (Fig. S12). The underlying reason is the differences in the number of susceptible individuals among the stochastic trajectories around 2005 (Fig. S34): those with a large number of susceptibles result in a peak in 2005 that is not observed in the data. Therefore, CV-A4 seems to have a *critical point* around 2005 where the dynamics can swing between a behaviour very similar to the data (and therefore provide a good fit) or a behaviour in anti-phase with the data (providing a bad fit). Because this critical point occurs early in the time-series, this explains the bimodal distribution of the SSR for this serotype (Fig. S31).

Some serotypes seem to be more sensitive to stochastic demography than others. For example, for some serotypes, all the simulated trajectories have a similar behaviour (e.g. E25, Fig. S29). For some others, the critical point where the dynamics result in different behaviours occurs late in time, therefore leading to small increases in SSR. For example, most of the simulations for CV-B2 reproduced the data well and only a tiny proportion failed to explain the last two peaks (Fig. S20). The consequences of stochastic demography resulting in different dynamics behaviour may be more important for serotypes with a period greater than 1 year (because of the possibility to be in anti-phase with the data), but not all the serotypes with multi-annual cycles show this phenomenon or show it for a very small fraction of simulations (e.g. CV-B3, Fig. S21).

The proportion of simulations with a small SSR may be a *measure* of how likely the observed epidemic trajectory for a given serotype is under the model.

The iterated filtering 2 (IF2) algorithm was developed to make inference with non-linear, stochastic, partially-observed models, as the one used here, where stochasticity may play an important role *(11)*. As a particle-filtering based algorithm, the way IF2 deals with stochasticity is by at each observation step, replacing the particles with a low likelihood by new particles in the proximity of those with higher likelihood (similar to a mutation-selection approach). As such, the epidemic trajectories obtained during the fitting process with IF2 are always in better agreement with the data than they can be the stochastic realizations of the model. Stochastic realizations of the model from the initial conditions with the MLE of the parameters may result in highly different behaviours, as discussed above and shown in Fig. S11 – Fig. S30. As a consequence of this variability and because we are interested in how well the model can explain the data, in our plots of model realizations (Figures 2–4 of the main text) we show a range of those that more closely match the data, selected as the 10 stochastic realizations with lower SSR of 100 simulated using the MLE of the parameters.

Fig. S1.

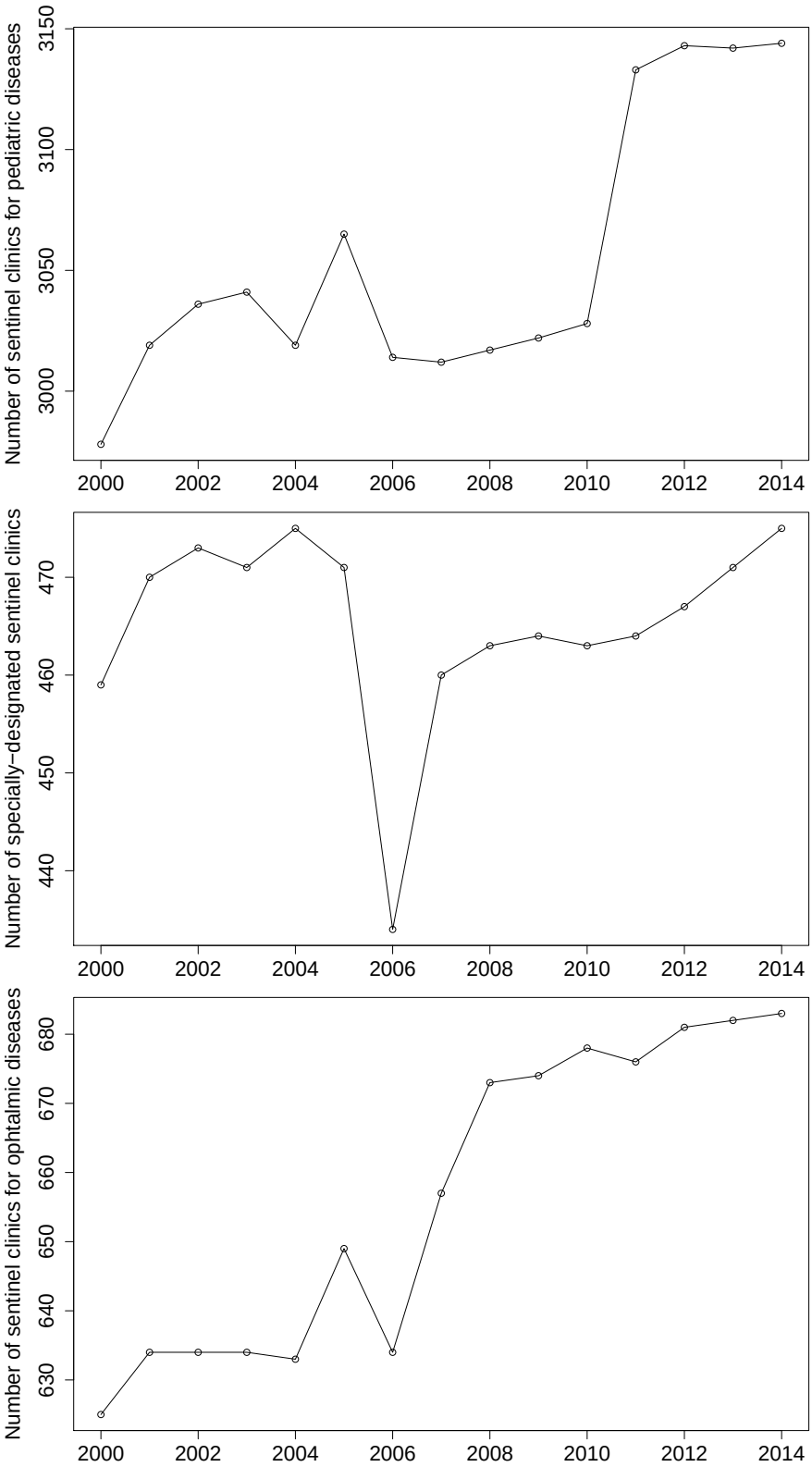

Fig. S1: Number of sentinel clinics for pediatric diseases (including surveillance of HFMD and herpangina) (top), specially-designated sentinel clinics for surveillance of aseptic meningitis (center) and sentinel clinics for ophtalmic diseases (including surveillance of acute haemorrhagic conjunctivitis) (bottom) between 2000 and 2014. Data available from https://www.niid.go.jp/niid/en/survei/2085-idwr/ydata/6053-report-eb2014-1.html

Fig. S2.

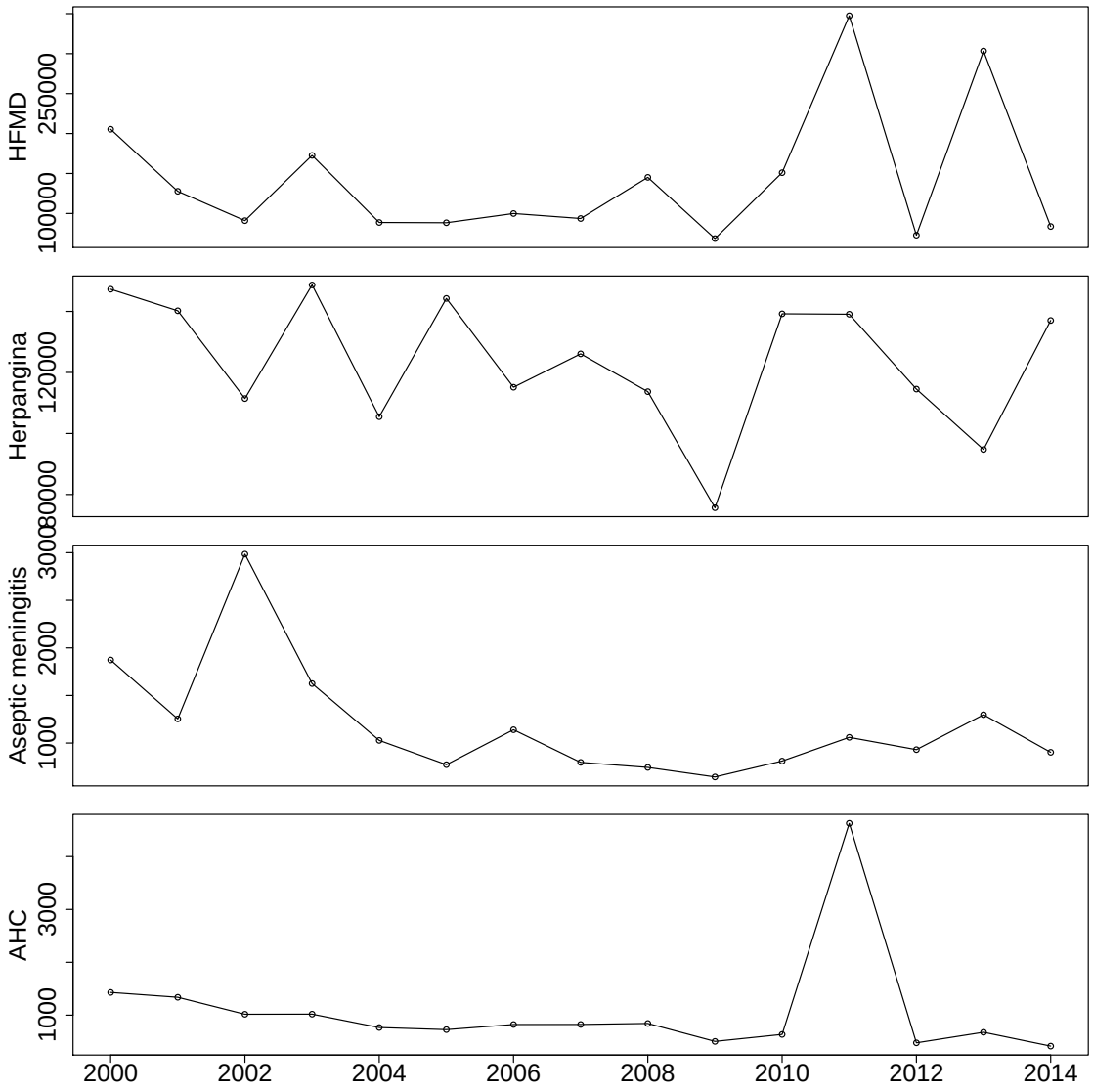

Fig. S2: Number of cases of HFMD, herpangina, aseptic meningitis and acute haemorrhagic conjunctivitis (AHC) diagnosed at the sentinel sites between 2000 and 2014. Data available from https://www.niid.go.jp/niid/en/survei/2085-idwr/ydata/6054-report-eb2014-2.html and https://www.niid.go.jp/niid/en/survei/2085-idwr/ydata/6056-report-eb2014-4.html

Fig. S3.

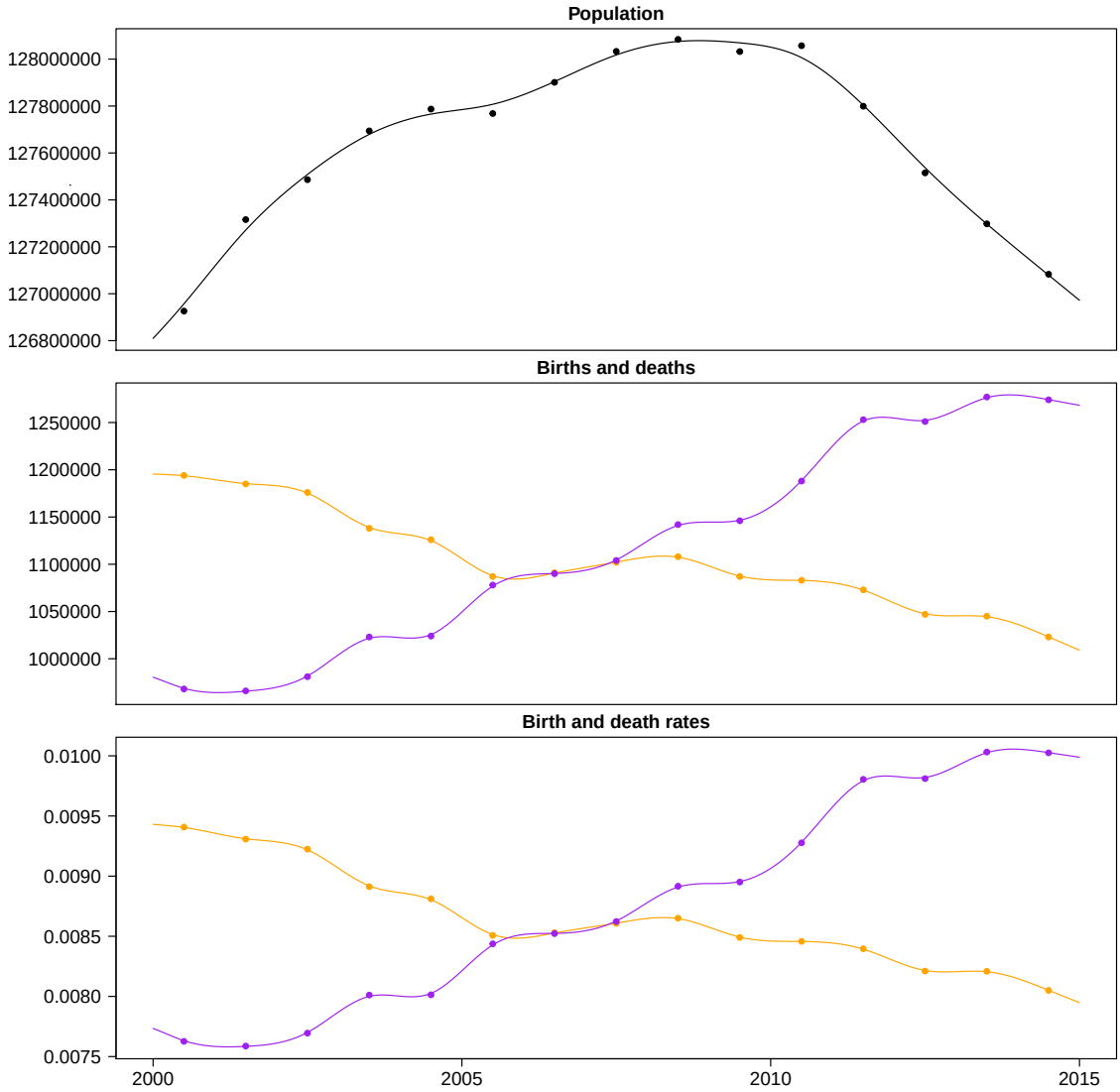

Fig. S3: Demographic data for Japan from 2000 to 2014. (Top) Total population size. (Center) Annual number of live births (orange) and deaths (purple). (Bottom) Annual birth (orange) and death (purple) rates. The dots are the annual values and the lines are smoothed splines (with 3 degrees of freedom for the population, and 10 for the remaining variables).

Fig. S4.

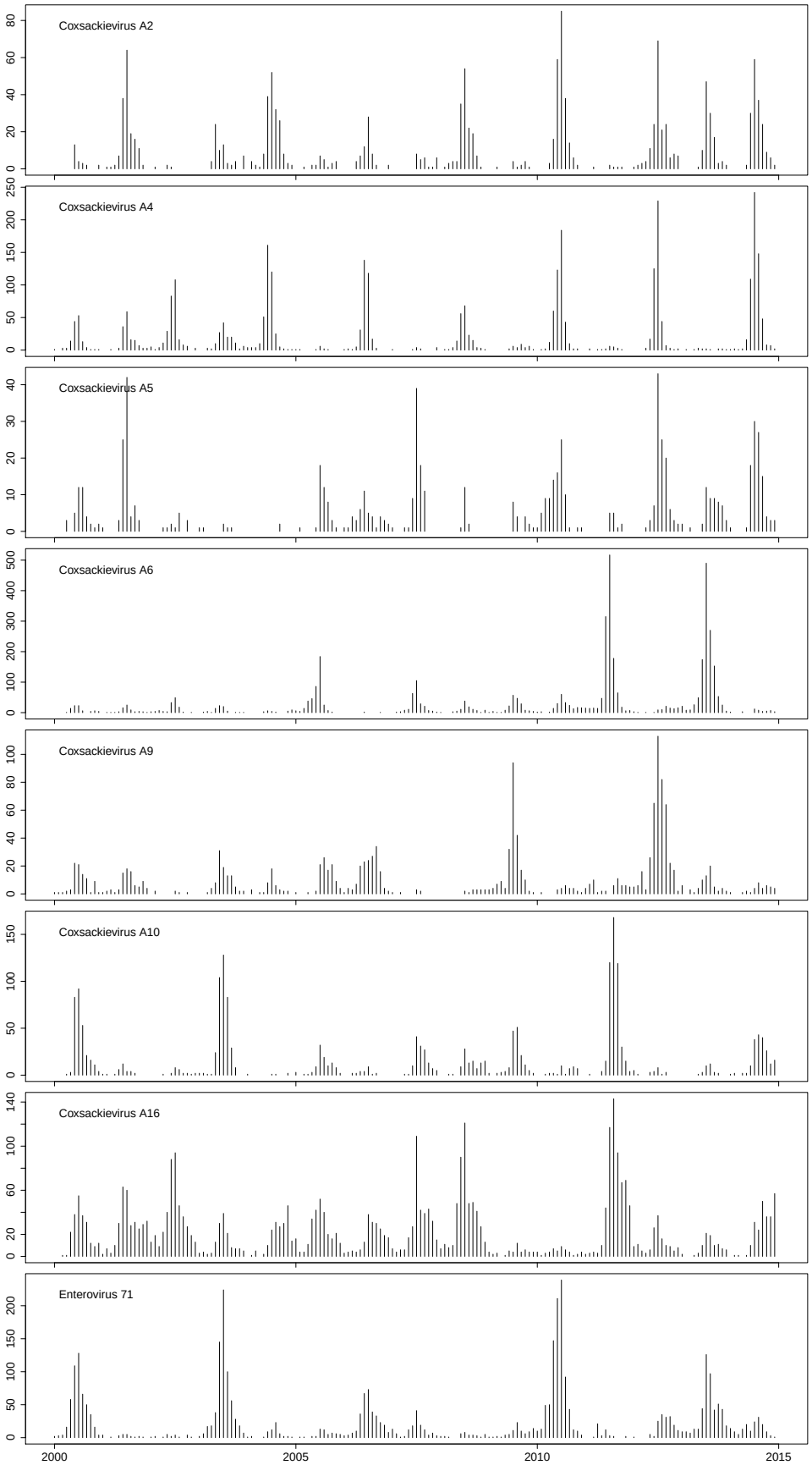

Fig. S4: Time-series of the monthly number of enterovirus reports between January 2000 and December 2014 in Japan for seven Coxsackievirus A serotypes and Enterovirus 71.

Fig. S5.

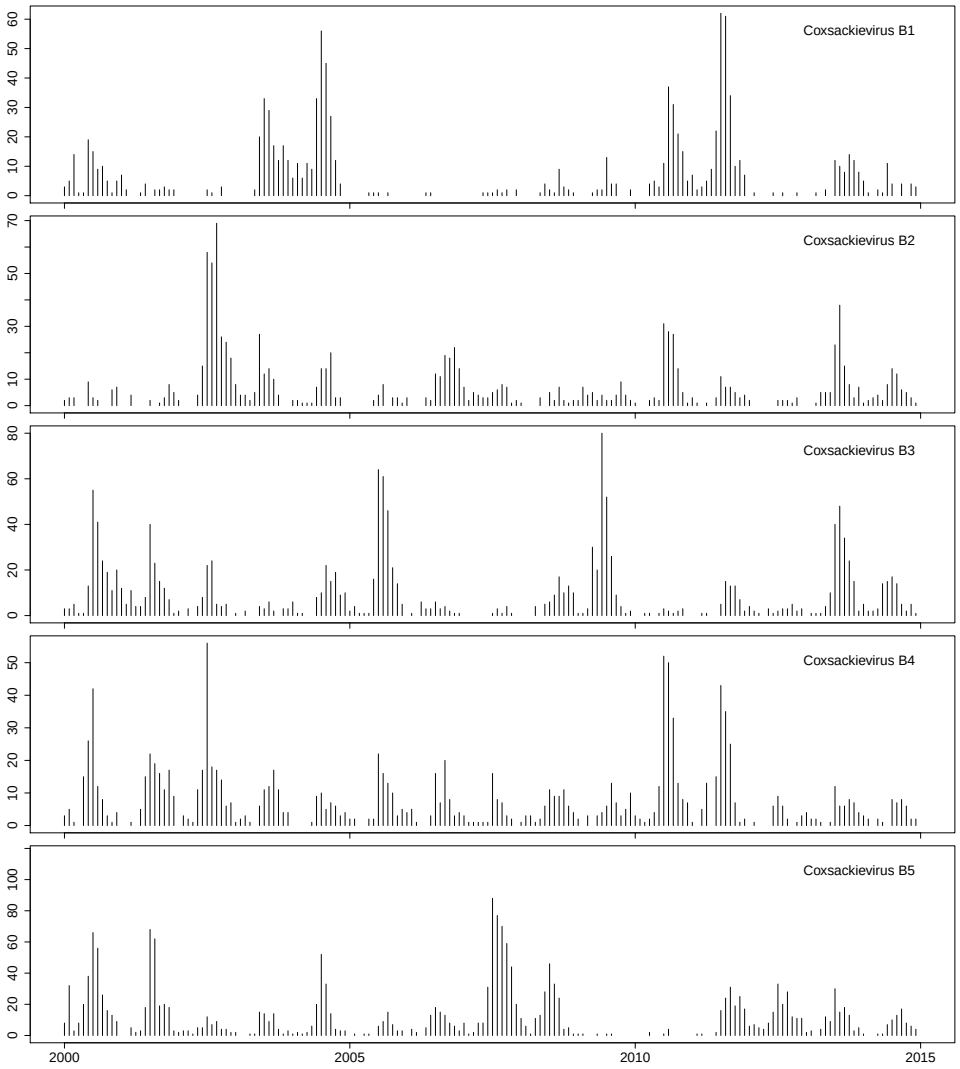

Fig. S5: Time-series of the monthly number of enterovirus reports between January 2000 and December 2014 in Japan for five Coxsackievirus B serotypes.

Fig. S6.

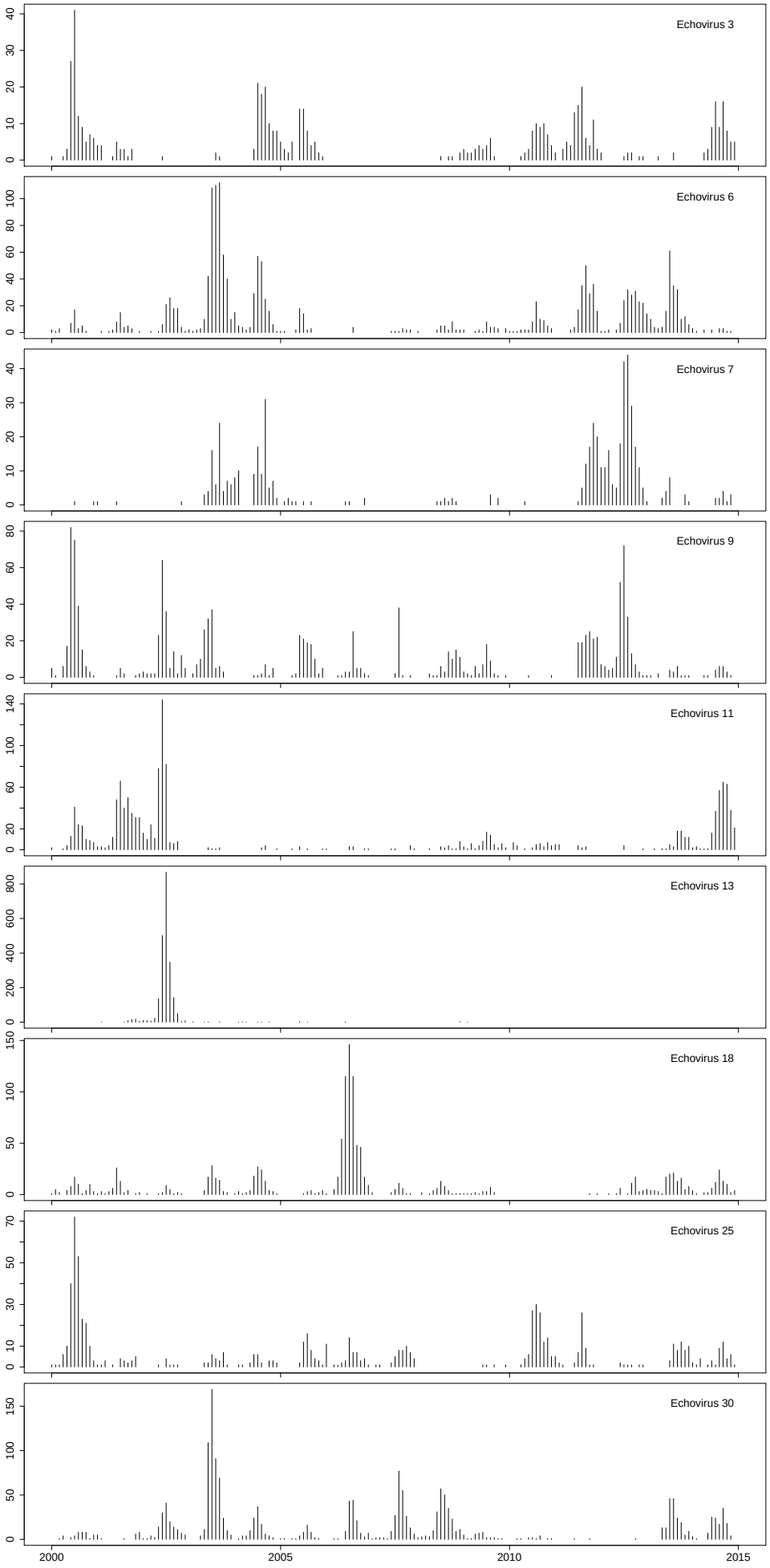

Fig. S6: Time-series of the monthly number of enterovirus reports between January 2000 and December 2014 in Japan for nine Echovirus serotypes.

Fig. S7.

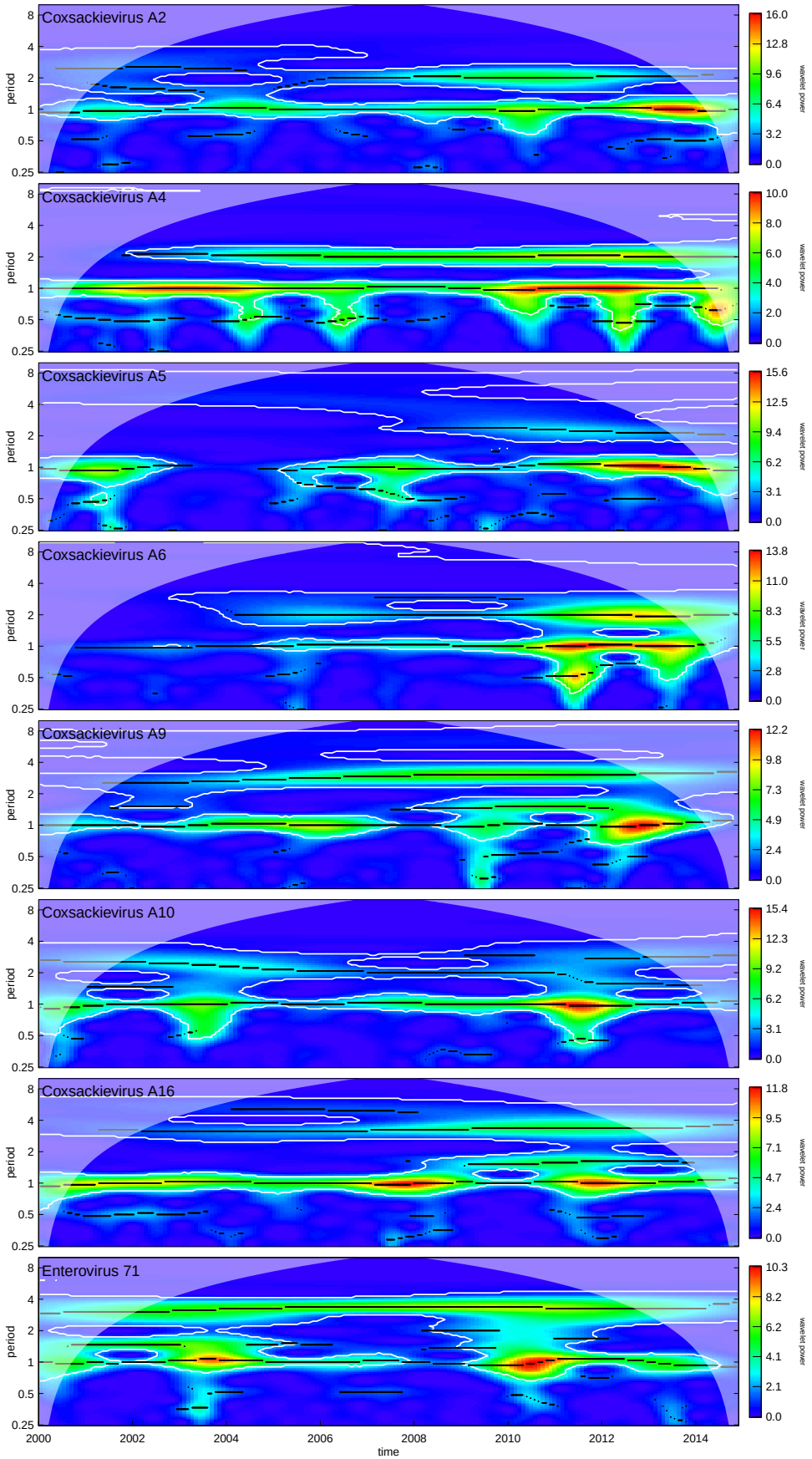

Fig. S7: Average wavelet power of the square-root–transformed time-series of the monthly number of enterovirus reports between January 2000 and December 2014 in Japan for seven Coxsackievirus A serotypes and Enterovirus 71.

Fig. S8.

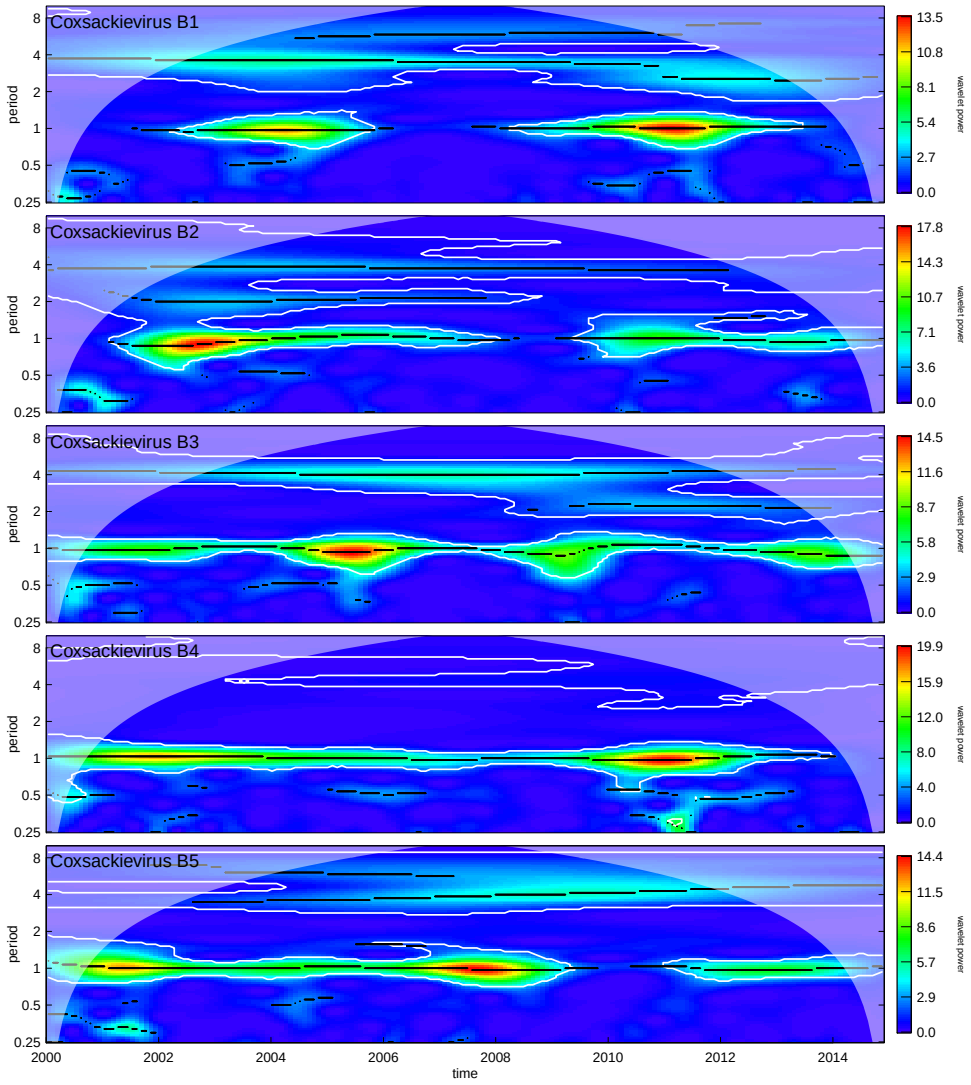

Fig. S8: Average wavelet power of the square-root–transformed time-series of the monthly number of enterovirus reports between January 2000 and December 2014 in Japan for five Coxsackievirus B serotypes.

Fig. S9.

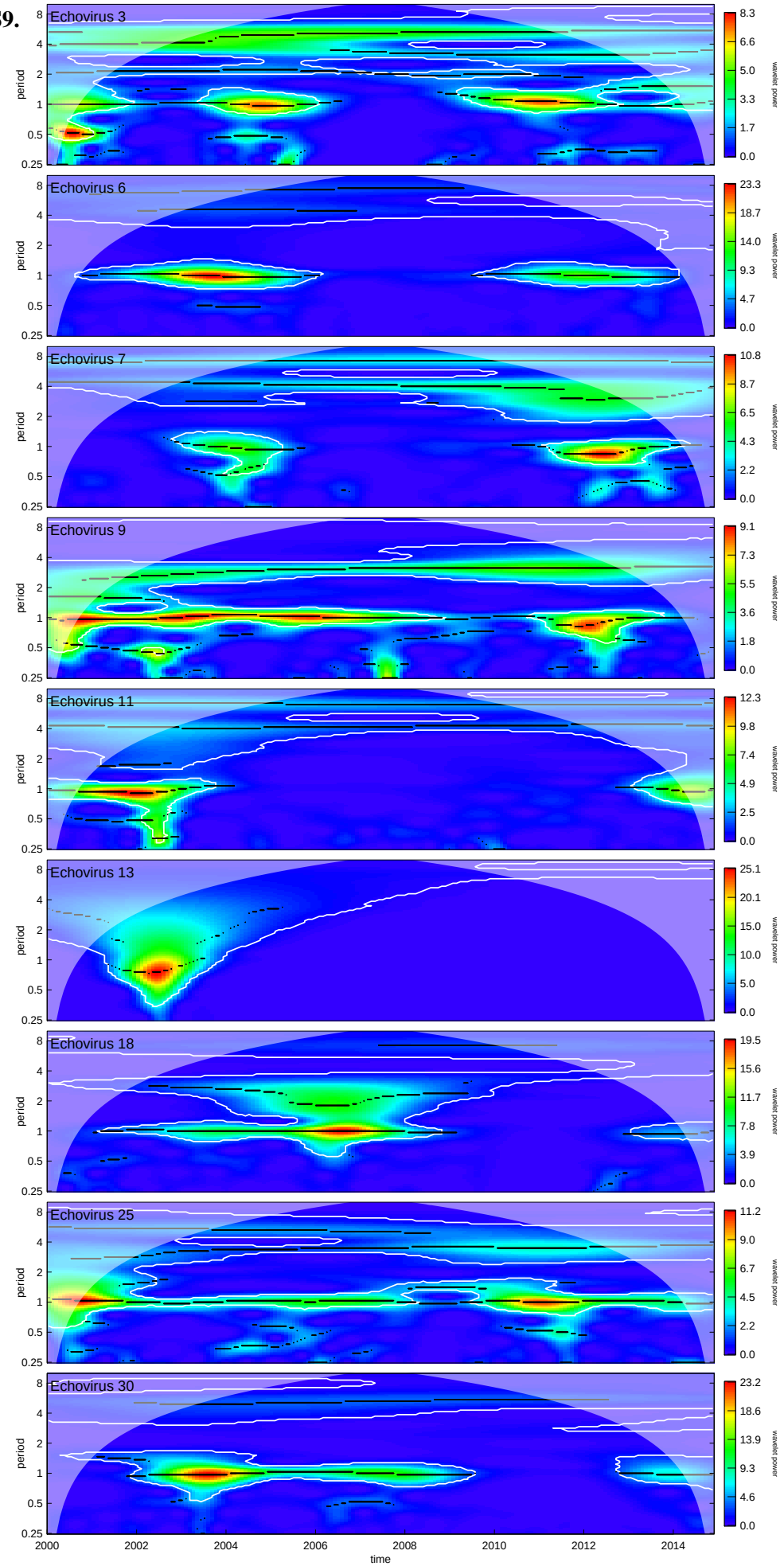

Fig. S9: Average wavelet power of the square-root–transformed time-series of the monthly number of enterovirus reports between January 2000 and December 2014 in Japan for nine Echovirus serotypes.

Fig. S10.

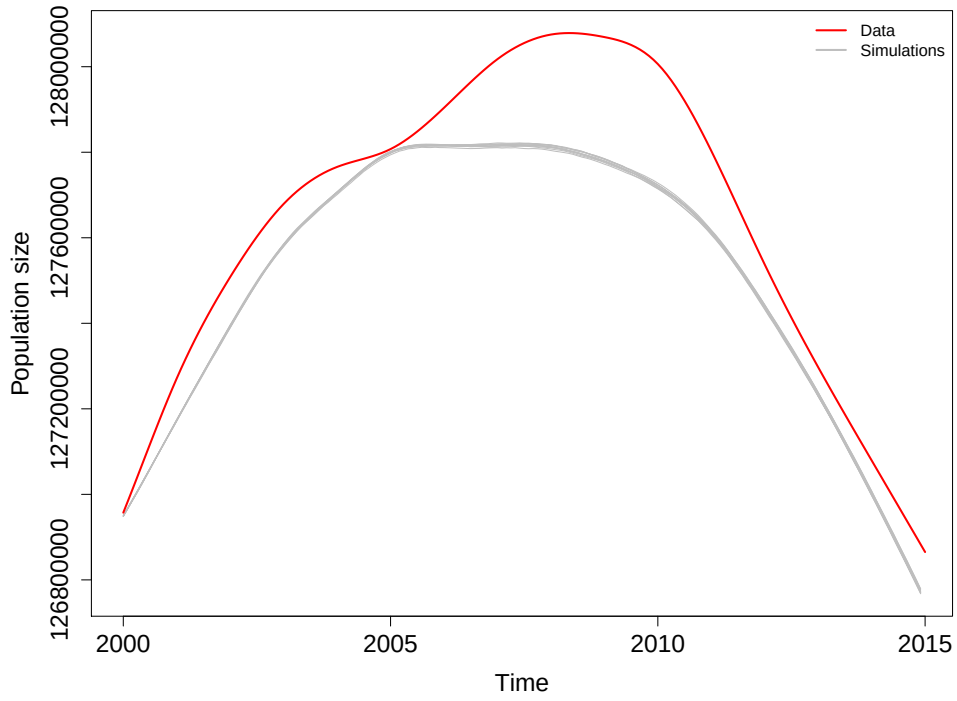

Fig. S10: Changes in annual population size between 2000 and 2014 predicted by the model (gray) and observed (red). Ten realizations of the model for the same parameter values are shown.

Fig. S11.

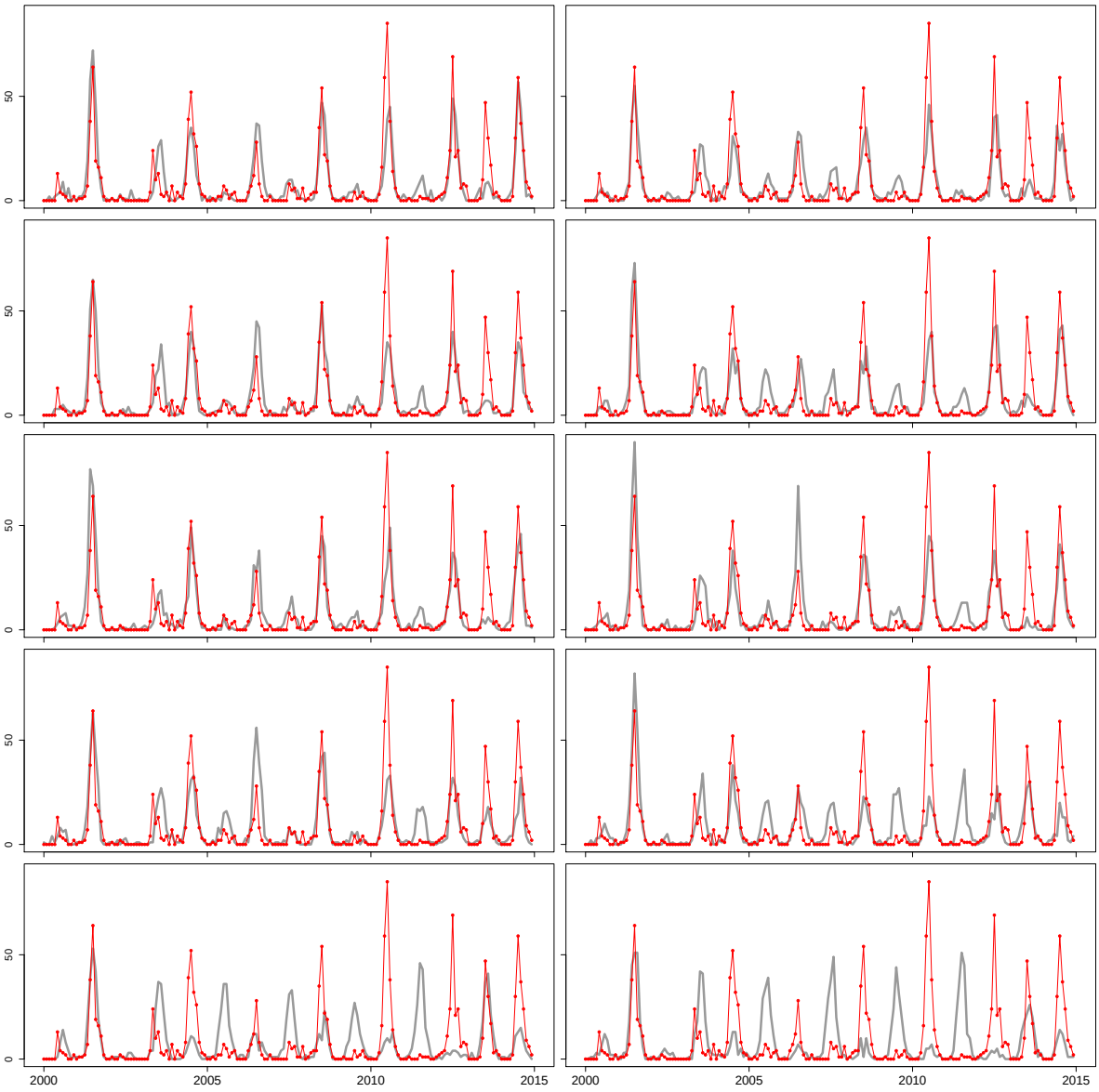

Fig. S11: Variability in the simulated realizations of the fitted model for CV-A2 obtained with the MLE. The observed number of monthly reported isolations (red line) and 10 stochastic realizations of the fitted model out of 100 for the MLE of the parameters (gray lines) are shown. From left to right, top to bottom, the 10 realizations shown correspond to the multiples of ten in the rank of their respective increasing sum of squared residuals (SSR): 10th, 20th,...,100th.

Fig. S12.

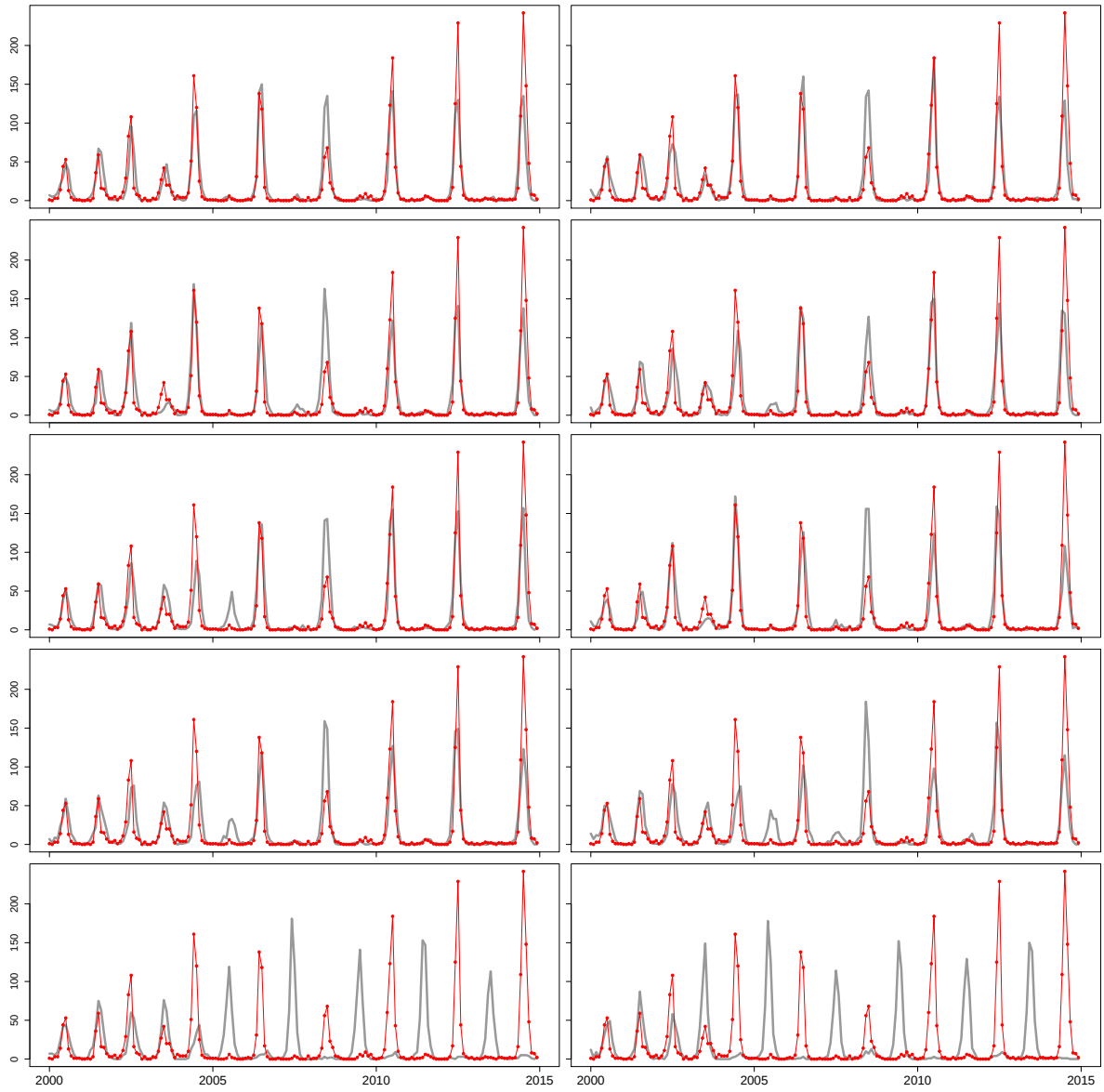

Fig. S12: Variability in the simulated realizations of the fitted model for CV-A4 obtained with the MLE. The observed number of monthly reported isolations (red line) and 10 stochastic realizations of the fitted model out of 100 for the MLE of the parameters (gray lines) are shown. From left to right, top to bottom, the 10 realizations shown correspond to the multiples of ten in the rank of their respective increasing sum of squared residuals (SSR): 10th, 20th,...,100th.

Fig. S13.

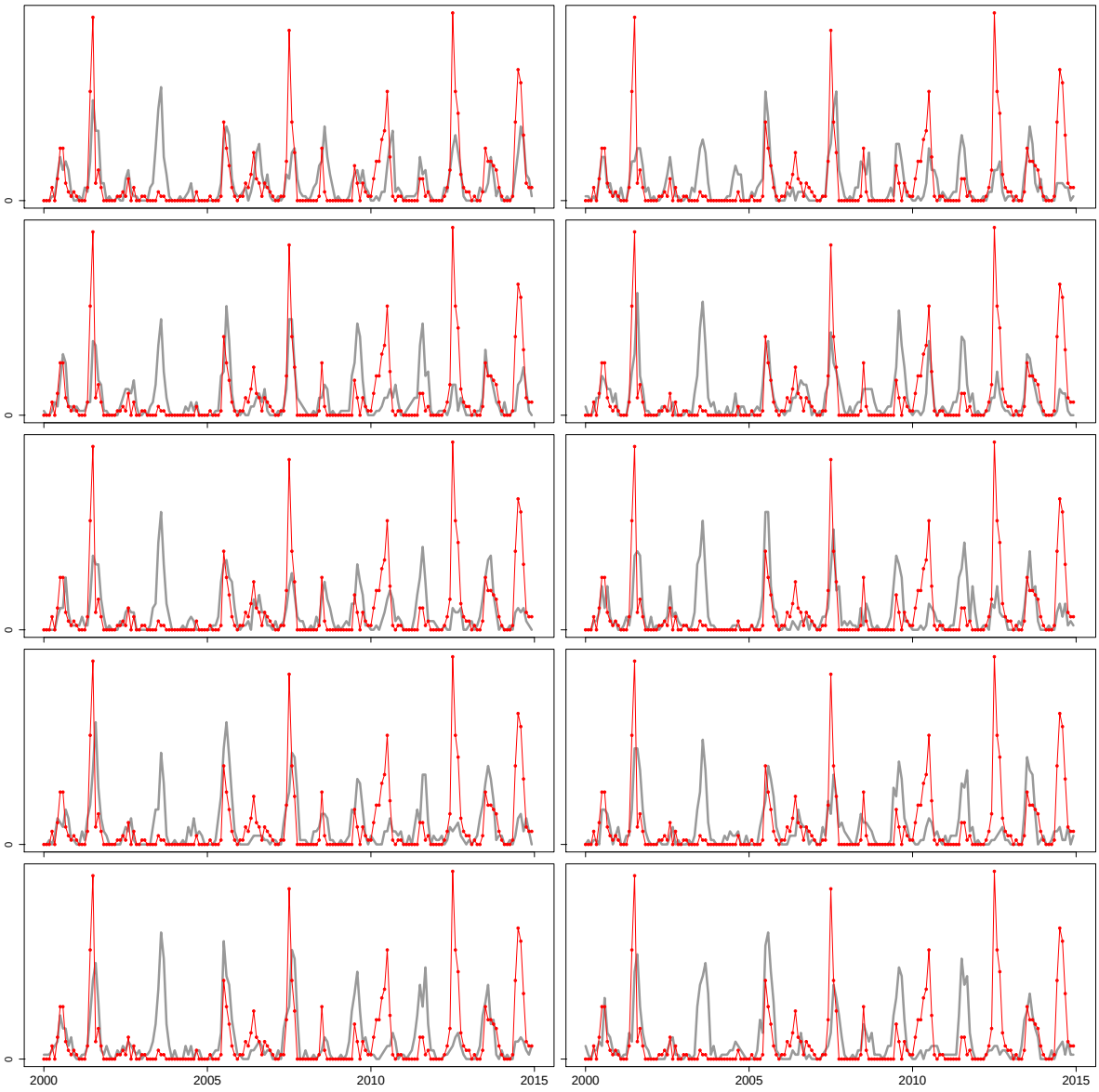

Fig. S13: Variability in the simulated realizations of the fitted model for CV-A5 obtained with the MLE. The observed number of monthly reported isolations (red line) and 10 stochastic realizations of the fitted model out of 100 for the MLE of the parameters (gray lines) are shown. From left to right, top to bottom, the 10 realizations shown correspond to the multiples of ten in the rank of their respective increasing sum of squared residuals (SSR): 10th, 20th,...,100th.

Fig. S14.

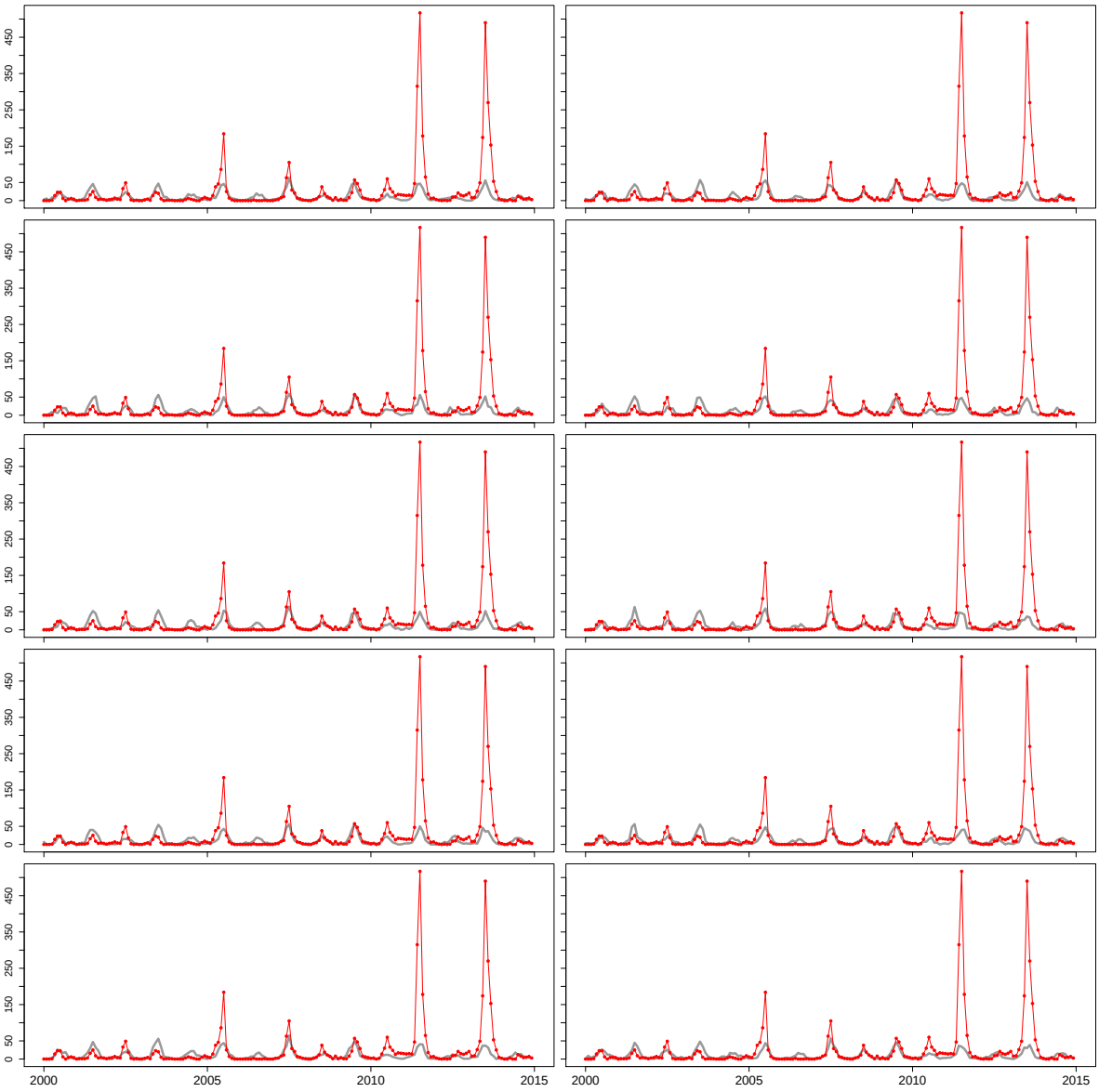

Fig. S14: Variability in the simulated realizations of the fitted model for CV-A6 obtained with the MLE. The observed number of monthly reported isolations (red line) and 10 stochastic realizations of the fitted model out of 100 for the MLE of the parameters (gray lines) are shown. From left to right, top to bottom, the 10 realizations shown correspond to the multiples of ten in the rank of their respective increasing sum of squared residuals (SSR): 10th, 20th,...,100th.

Fig. S15.

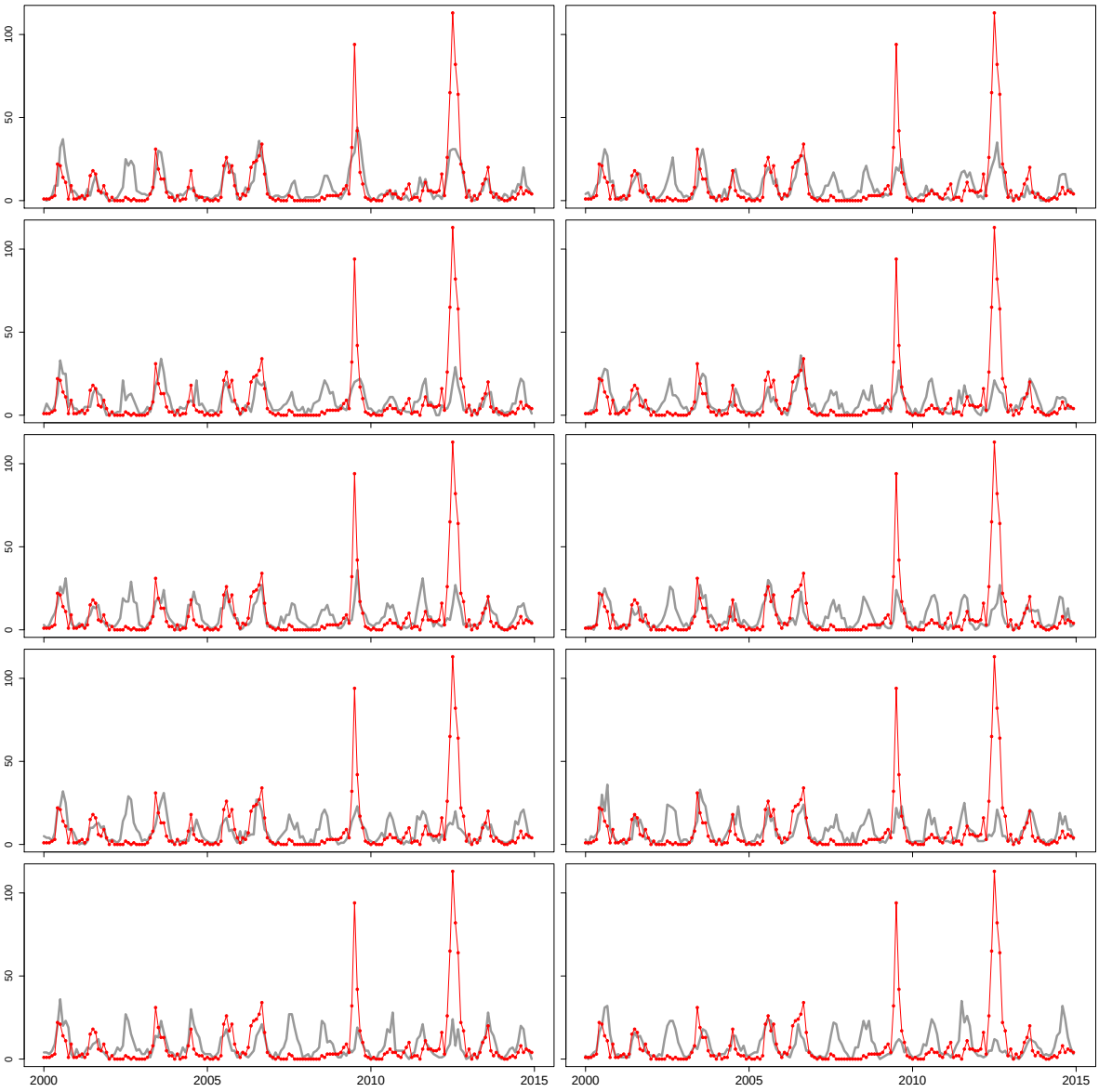

Fig. S15: Variability in the simulated realizations of the fitted model for CV-A9 obtained with the MLE. The observed number of monthly reported isolations (red line) and 10 stochastic realizations of the fitted model out of 100 for the MLE of the parameters (gray lines) are shown. From left to right, top to bottom, the 10 realizations shown correspond to the multiples of ten in the rank of their respective increasing sum of squared residuals (SSR): 10th, 20th,...,100th.

Fig. S16.

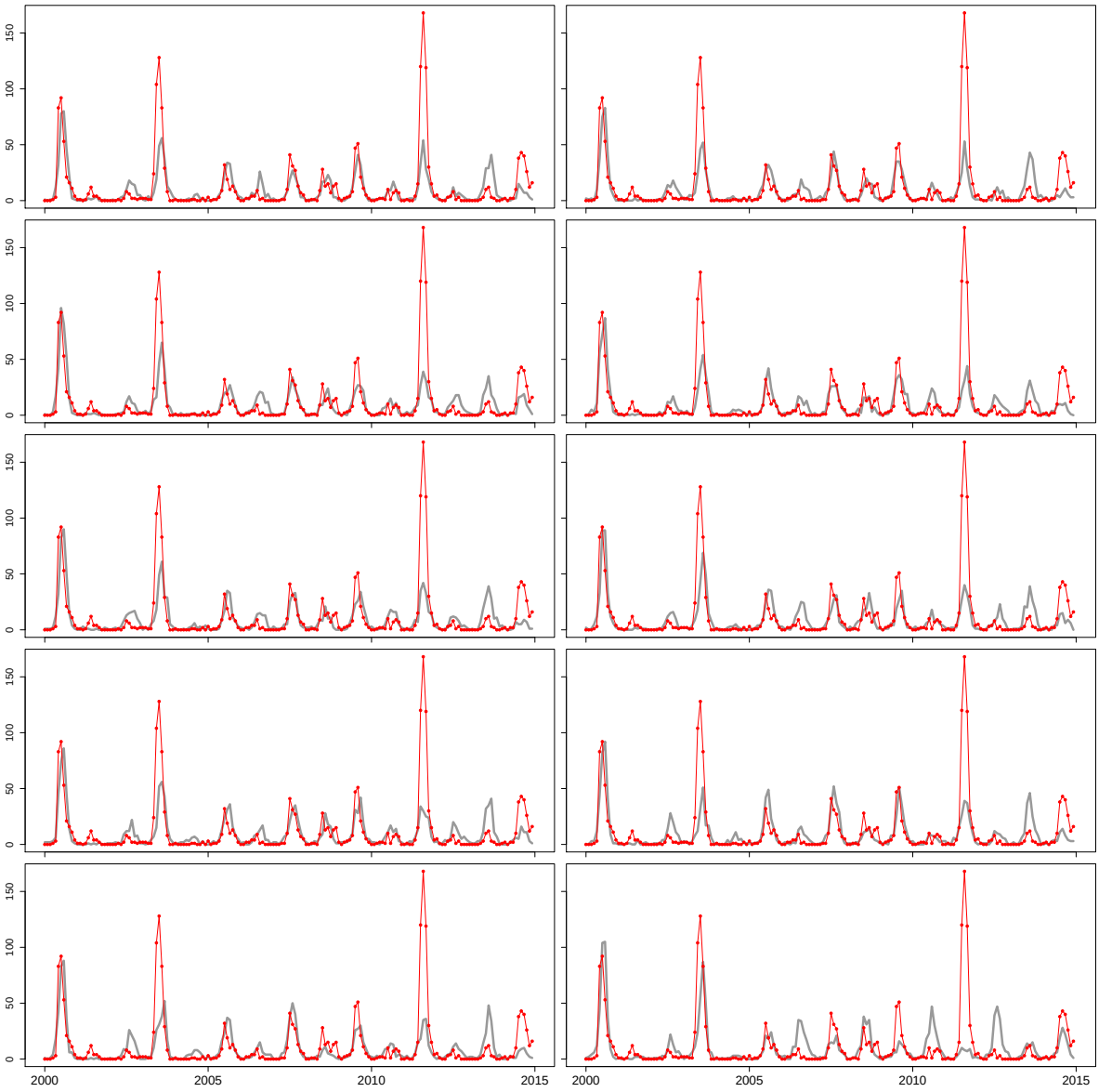

Fig. S16: Variability in the simulated realizations of the fitted model for CV-A10 obtained with the MLE. The observed number of monthly reported isolations (red line) and 10 stochastic realizations of the fitted model out of 100 for the MLE of the parameters (gray lines) are shown. From left to right, top to bottom, the 10 realizations shown correspond to the multiples of ten in the rank of their respective increasing sum of squared residuals (SSR): 10th, 20th,...,100th.

Fig. S17.

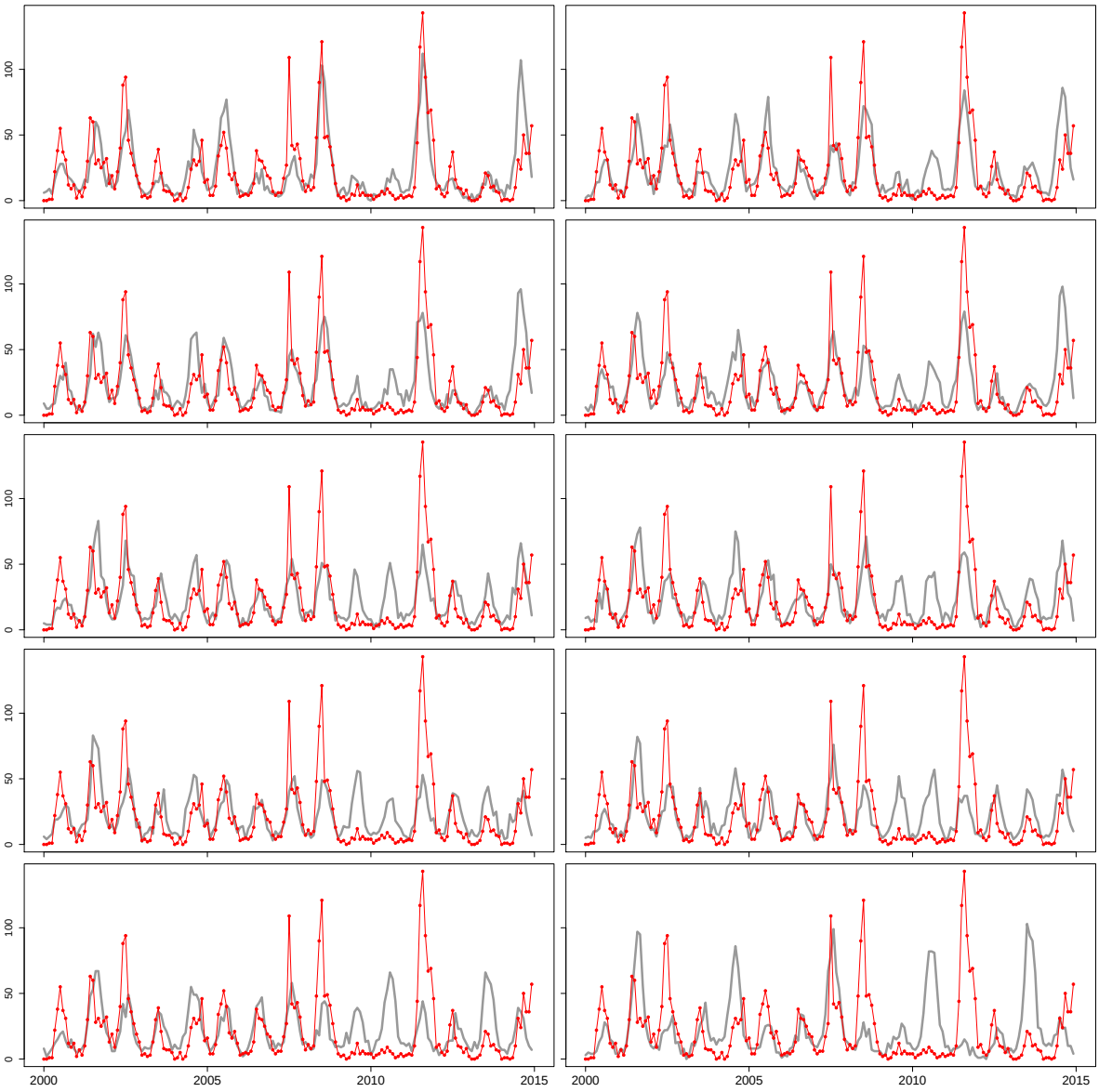

Fig. S17: Variability in the simulated realizations of the fitted model for CV-A16 obtained with the MLE. The observed number of monthly reported isolations (red line) and 10 stochastic realizations of the fitted model out of 100 for the MLE of the parameters (gray lines) are shown. From left to right, top to bottom, the 10 realizations shown correspond to the multiples of ten in the rank of their respective increasing sum of squared residuals (SSR): 10th, 20th,...,100th.

Fig. S18.

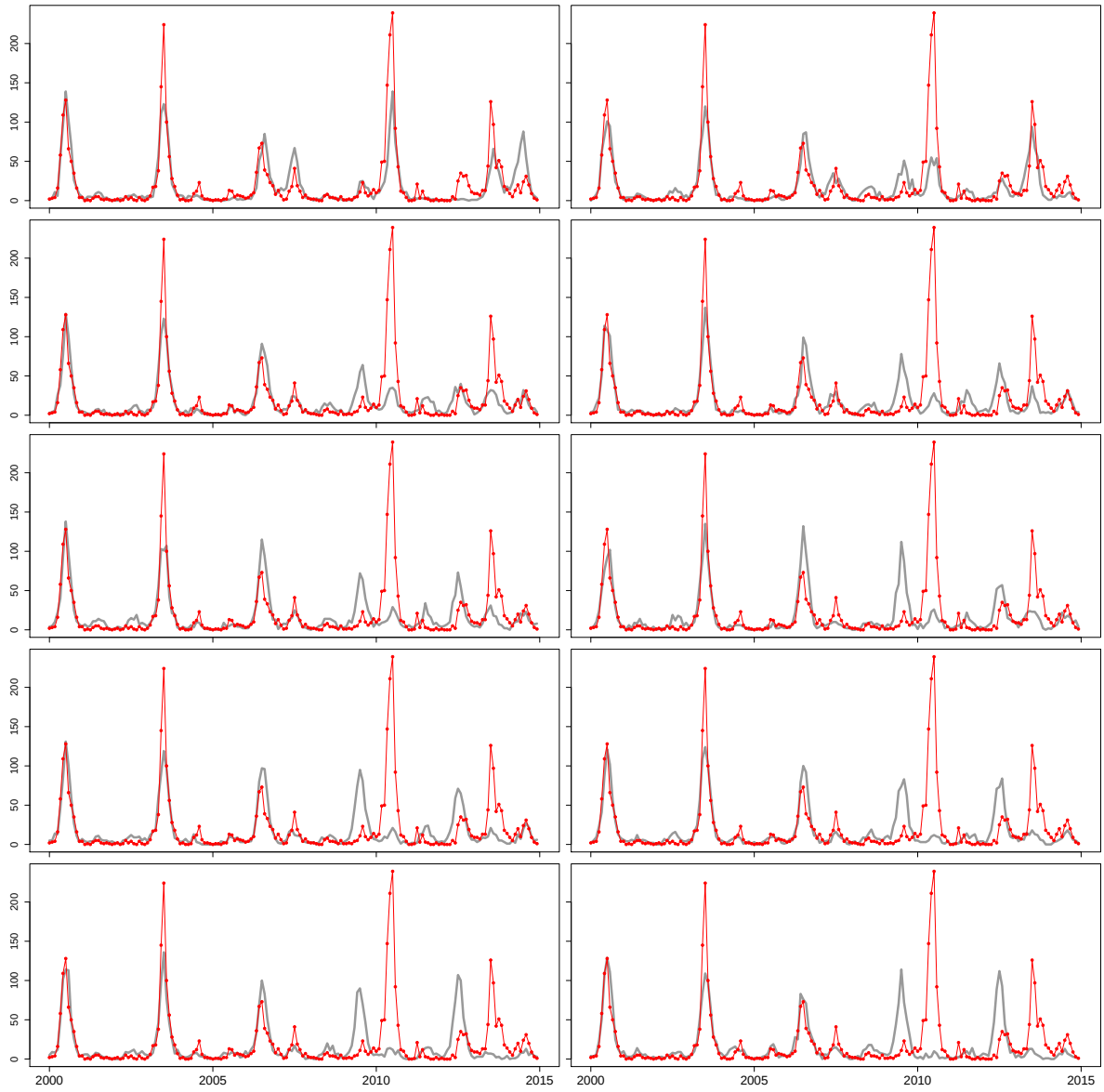

Fig. S18: Variability in the simulated realizations of the fitted model for EV-A71 obtained with the MLE. The observed number of monthly reported isolations (red line) and 10 stochastic realizations of the fitted model out of 100 for the MLE of the parameters (gray lines) are shown. From left to right, top to bottom, the 10 realizations shown correspond to the multiples of ten in the rank of their respective increasing sum of squared residuals (SSR): 10th, 20th,...,100th.

Fig. S19.

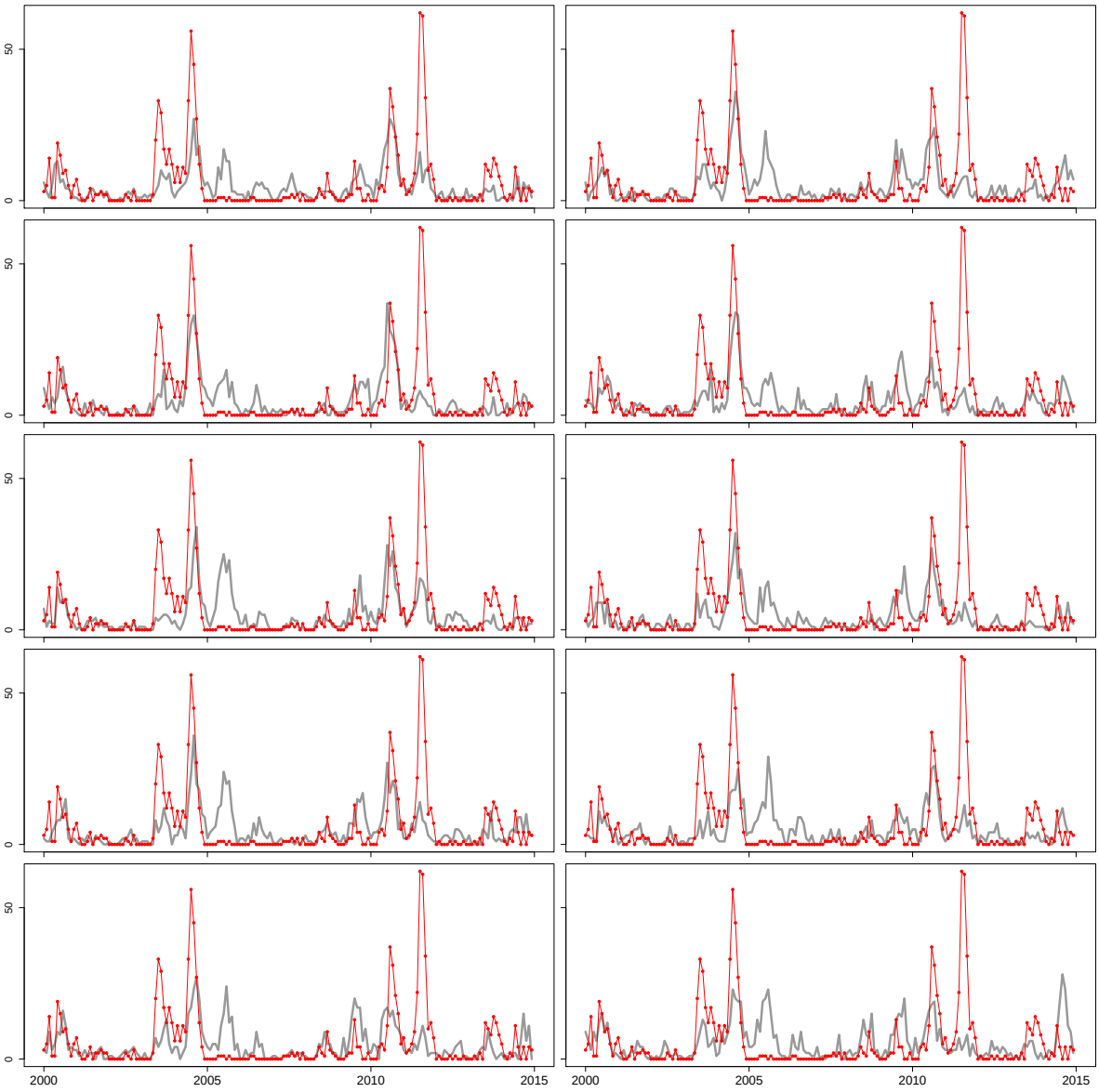

Fig. S19: Variability in the simulated realizations of the fitted model for CV-B1 obtained with the MLE. The observed number of monthly reported isolations (red line) and 10 stochastic realizations of the fitted model out of 100 for the MLE of the parameters (gray lines) are shown. From left to right, top to bottom, the 10 realizations shown correspond to the multiples of ten in the rank of their respective increasing sum of squared residuals (SSR): 10th, 20th,...,100th.

Fig. S20.

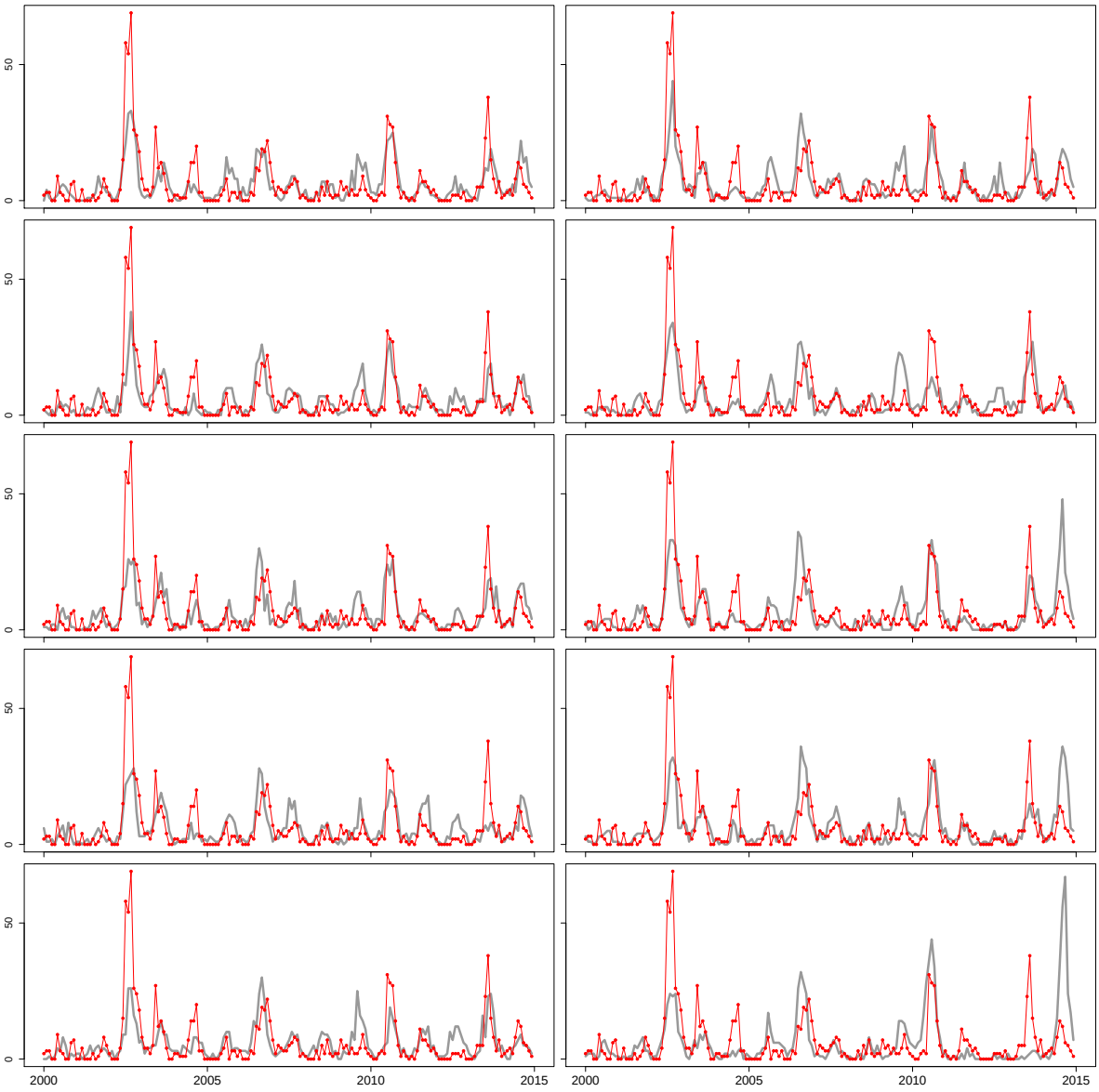

Fig. S20: Variability in the simulated realizations of the fitted model for CV-B2 obtained with the MLE. The observed number of monthly reported isolations (red line) and 10 stochastic realizations of the fitted model out of 100 for the MLE of the parameters (gray lines) are shown. From left to right, top to bottom, the 10 realizations shown correspond to the multiples of ten in the rank of their respective increasing sum of squared residuals (SSR): 10th, 20th,...,100th.

Fig. S21.

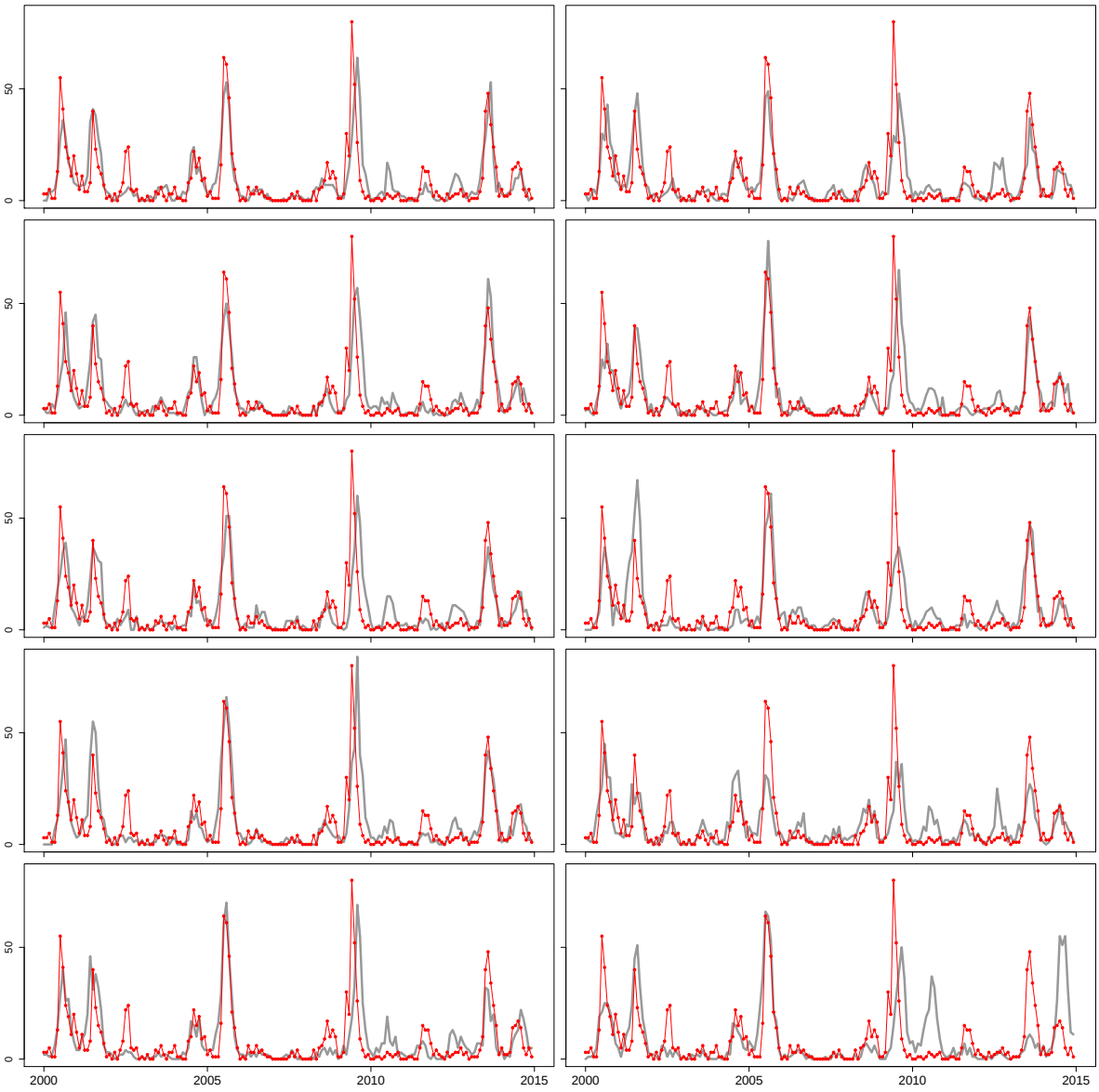

Fig. S21: Variability in the simulated realizations of the fitted model for CV-B3 obtained with the MLE. The observed number of monthly reported isolations (red line) and 10 stochastic realizations of the fitted model out of 100 for the MLE of the parameters (gray lines) are shown. From left to right, top to bottom, the 10 realizations shown correspond to the multiples of ten in the rank of their respective increasing sum of squared residuals (SSR): 10th, 20th,...,100th.

Fig. S22.

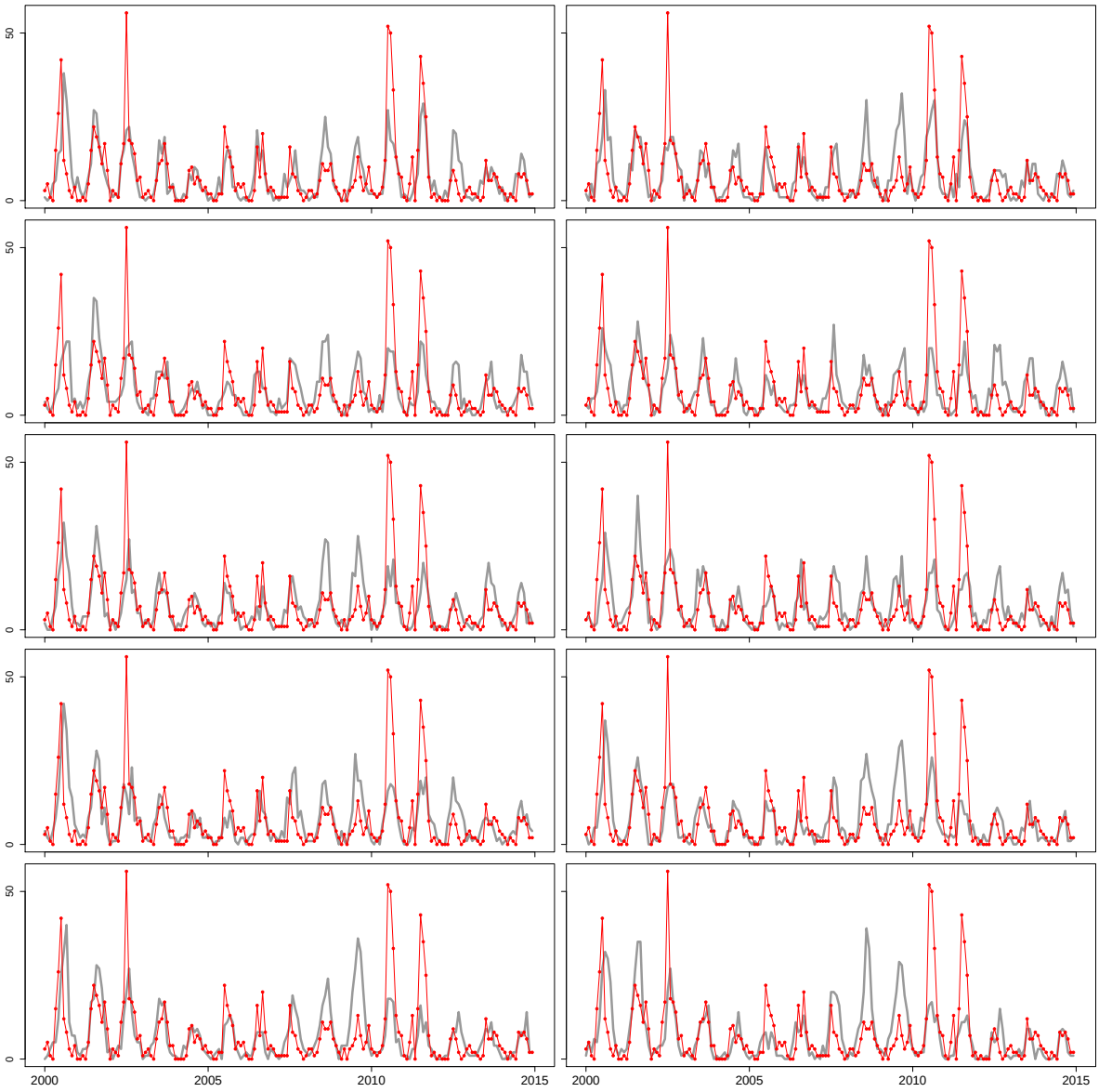

Fig. S22: Variability in the simulated realizations of the fitted model for CV-B4 obtained with the MLE. The observed number of monthly reported isolations (red line) and 10 stochastic realizations of the fitted model out of 100 for the MLE of the parameters (gray lines) are shown. From left to right, top to bottom, the 10 realizations shown correspond to the multiples of ten in the rank of their respective increasing sum of squared residuals (SSR): 10th, 20th,...,100th.

Fig. S23.

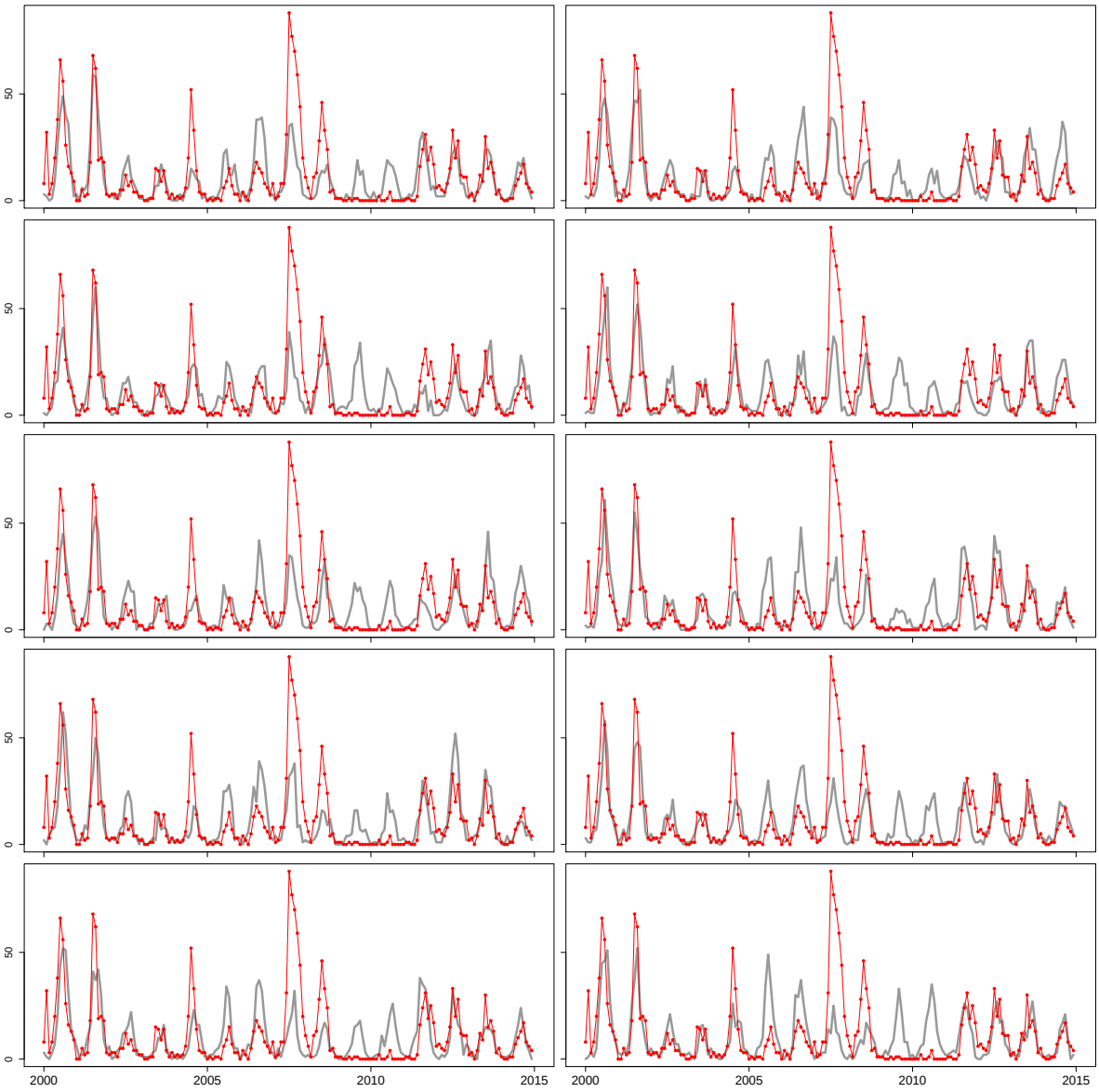

Fig. S23: Variability in the simulated realizations of the fitted model for CV-B5 obtained with the MLE. The observed number of monthly reported isolations (red line) and 10 stochastic realizations of the fitted model out of 100 for the MLE of the parameters (gray lines) are shown. From left to right, top to bottom, the 10 realizations shown correspond to the multiples of ten in the rank of their respective increasing sum of squared residuals (SSR): 10th, 20th,...,100th.

Fig. S24.

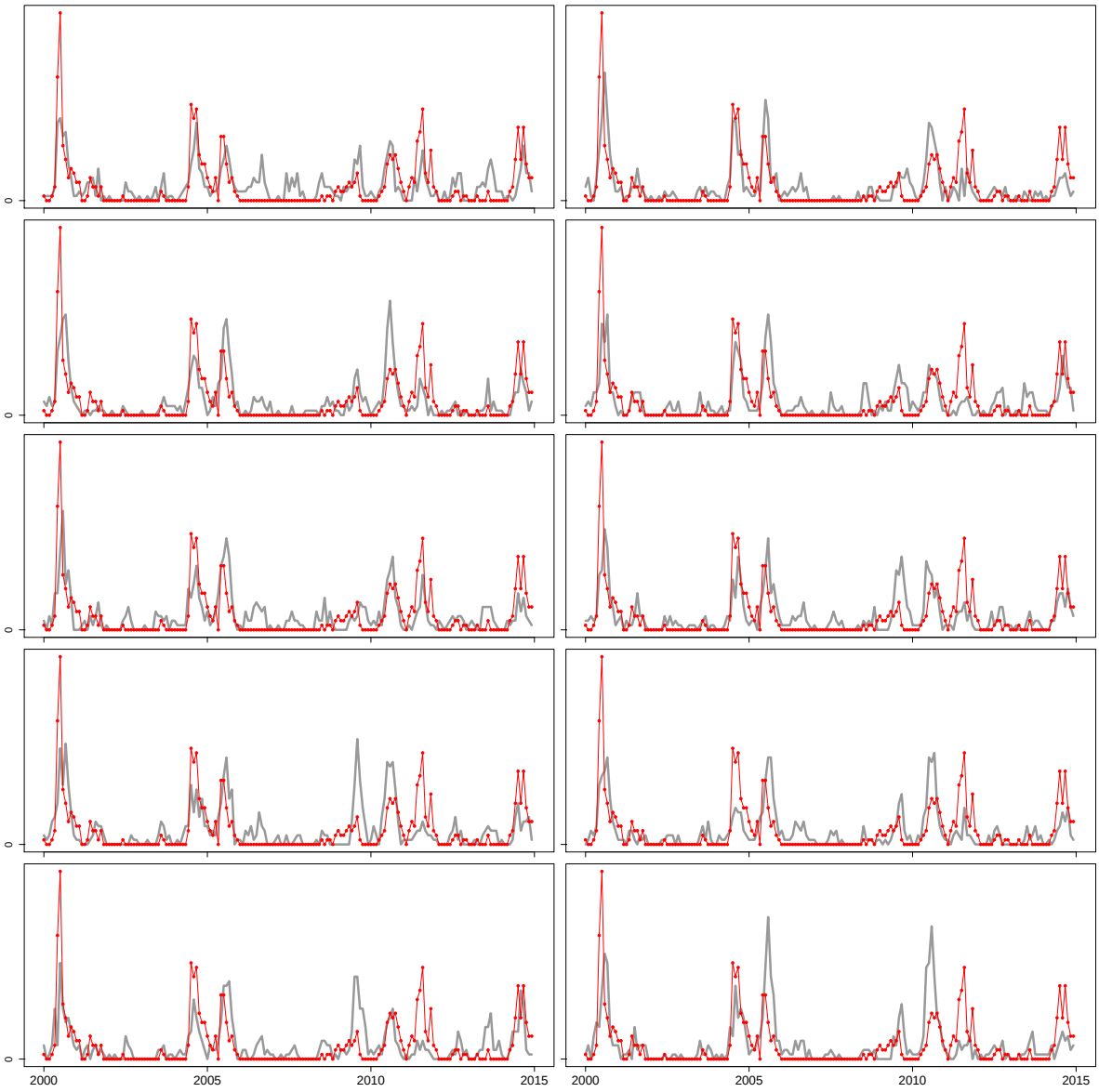

Fig. S24: Variability in the simulated realizations of the fitted model for E3 obtained with the MLE. The observed number of monthly reported isolations (red line) and 10 stochastic realizations of the fitted model out of 100 for the MLE of the parameters (gray lines) are shown. From left to right, top to bottom, the 10 realizations shown correspond to the multiples of ten in the rank of their respective increasing sum of squared residuals (SSR): 10th, 20th,...,100th.

Fig. S25.

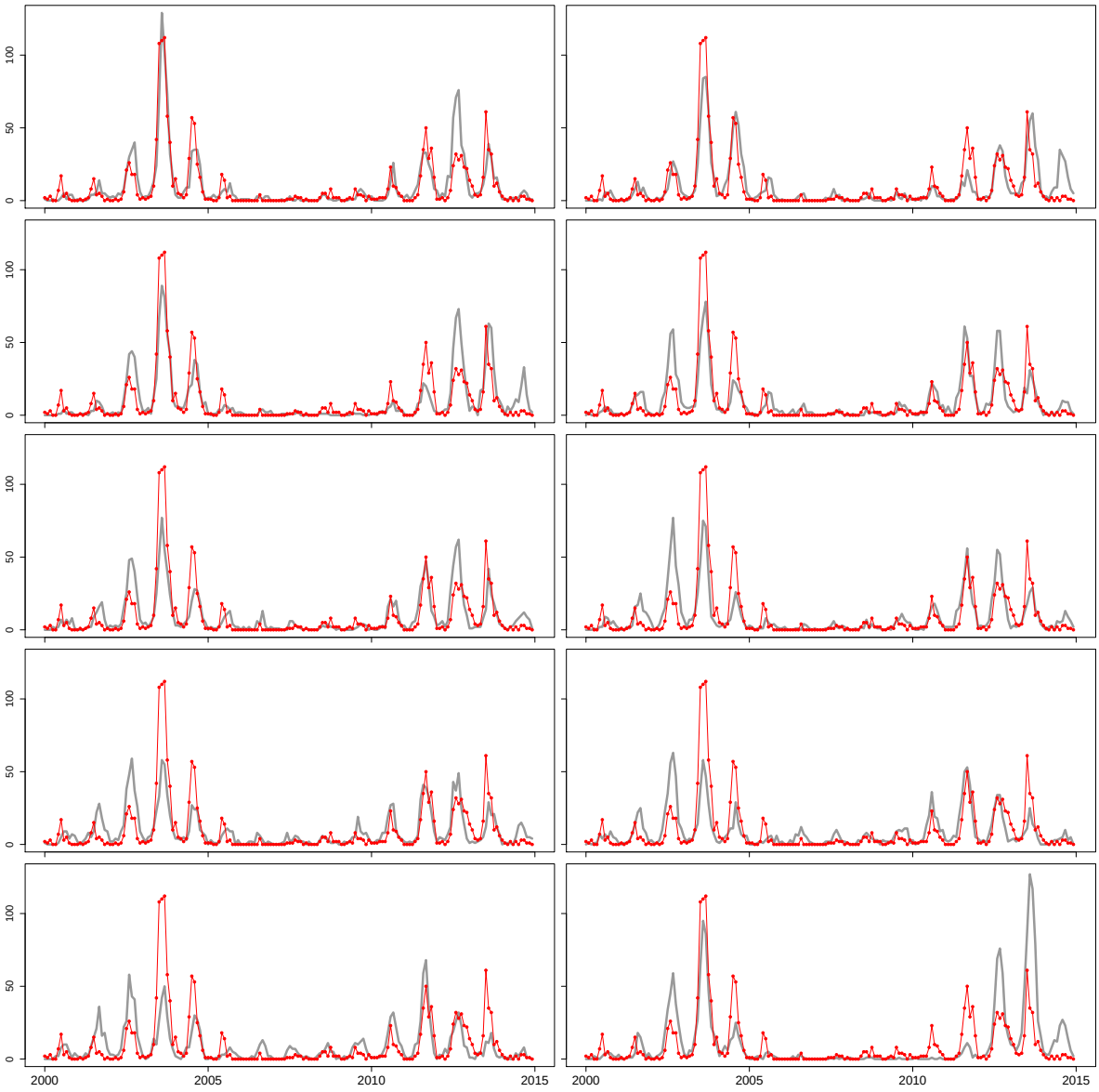

Fig. S25: Variability in the simulated realizations of the fitted model for E6 obtained with the MLE. The observed number of monthly reported isolations (red line) and 10 stochastic realizations of the fitted model out of 100 for the MLE of the parameters (gray lines) are shown. From left to right, top to bottom, the 10 realizations shown correspond to the multiples of ten in the rank of their respective increasing sum of squared residuals (SSR): 10th, 20th,...,100th.

Fig. S26.

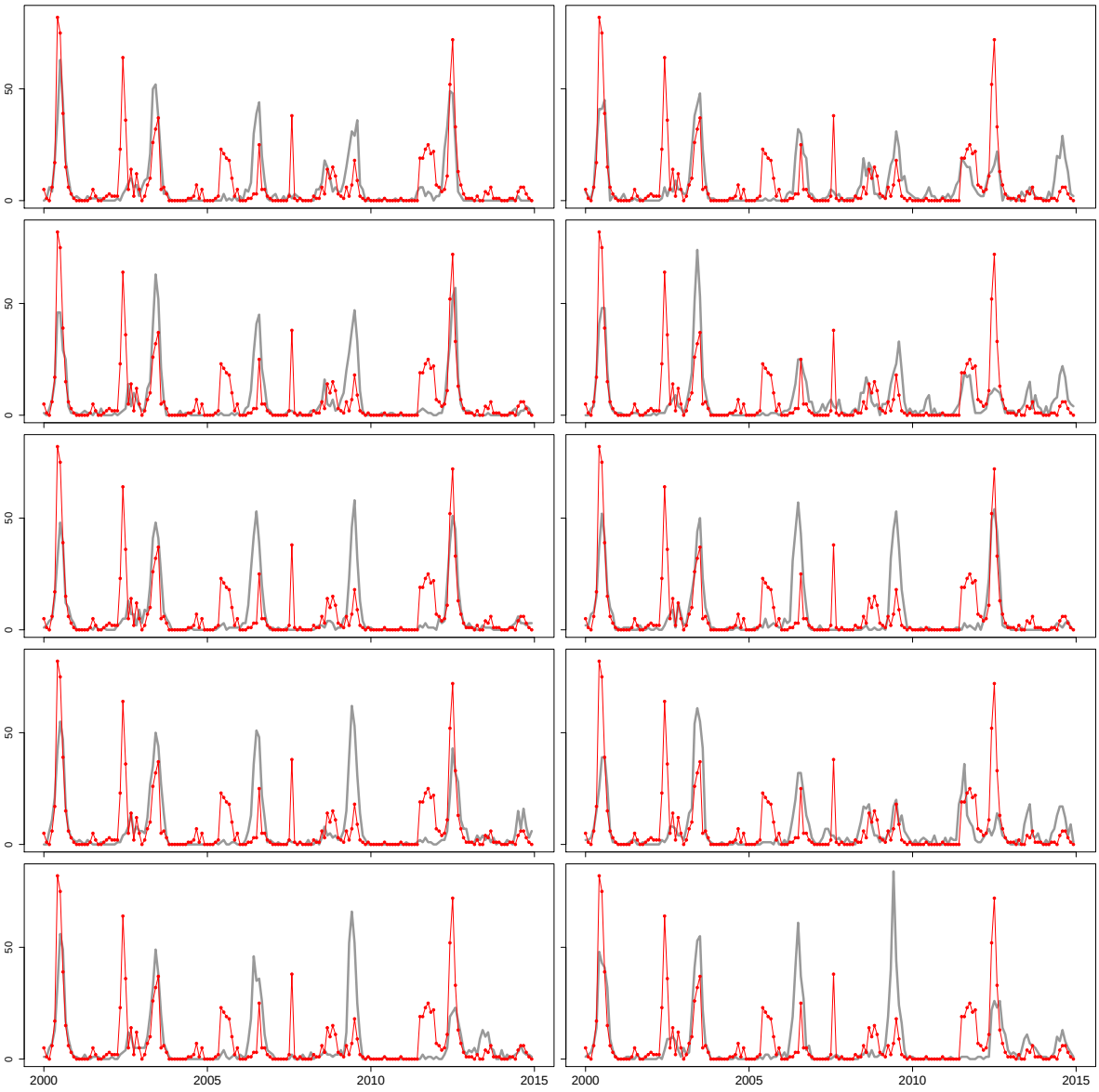

Fig. S26: Variability in the simulated realizations of the fitted model for E9 obtained with the MLE. The observed number of monthly reported isolations (red line) and 10 stochastic realizations of the fitted model out of 100 for the MLE of the parameters (gray lines) are shown. From left to right, top to bottom, the 10 realizations shown correspond to the multiples of ten in the rank of their respective increasing sum of squared residuals (SSR): 10th, 20th,...,100th.

Fig. S27.

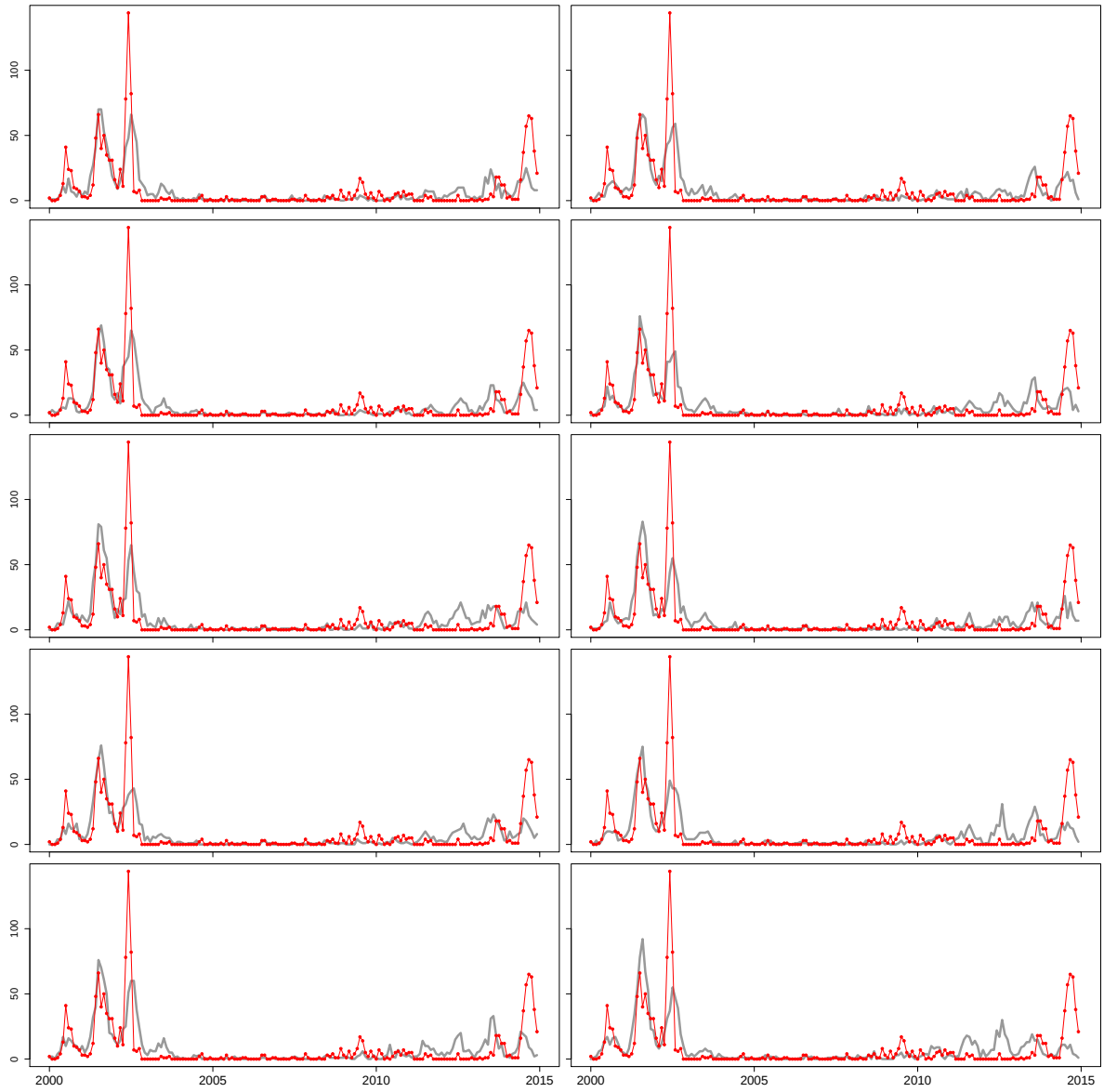

Fig. S27: Variability in the simulated realizations of the fitted model for E11 obtained with the MLE. The observed number of monthly reported isolations (red line) and 10 stochastic realizations of the fitted model out of 100 for the MLE of the parameters (gray lines) are shown. From left to right, top to bottom, the 10 realizations shown correspond to the multiples of ten in the rank of their respective increasing sum of squared residuals (SSR): 10th, 20th,...,100th.

Fig. S28.

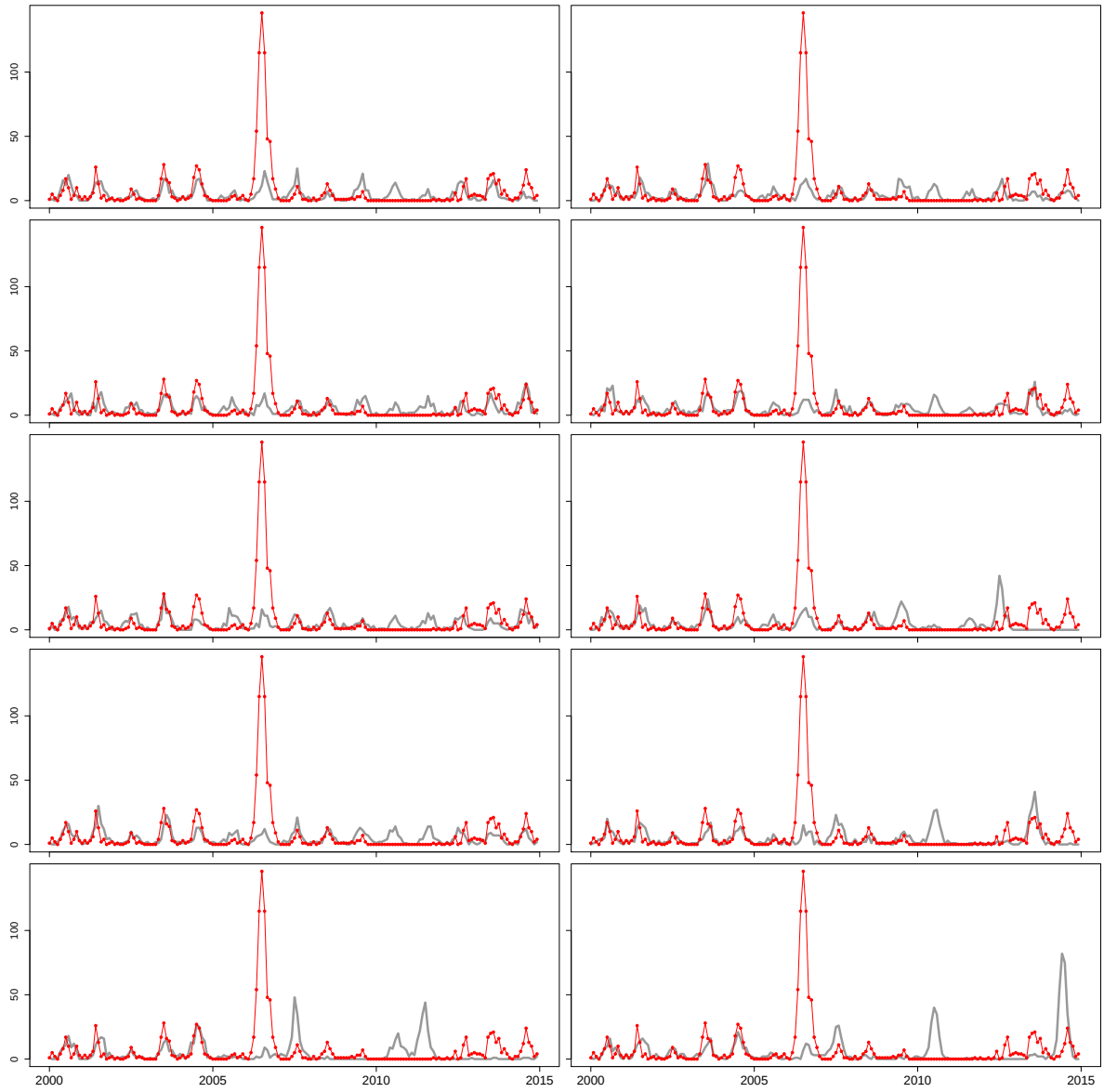

Fig. S28: Variability in the simulated realizations of the fitted model for E18 obtained with the MLE. The observed number of monthly reported isolations (red line) and 10 stochastic realizations of the fitted model out of 100 for the MLE of the parameters (gray lines) are shown. From left to right, top to bottom, the 10 realizations shown correspond to the multiples of ten in the rank of their respective increasing sum of squared residuals (SSR): 10th, 20th,...,100th.

Fig. S29.

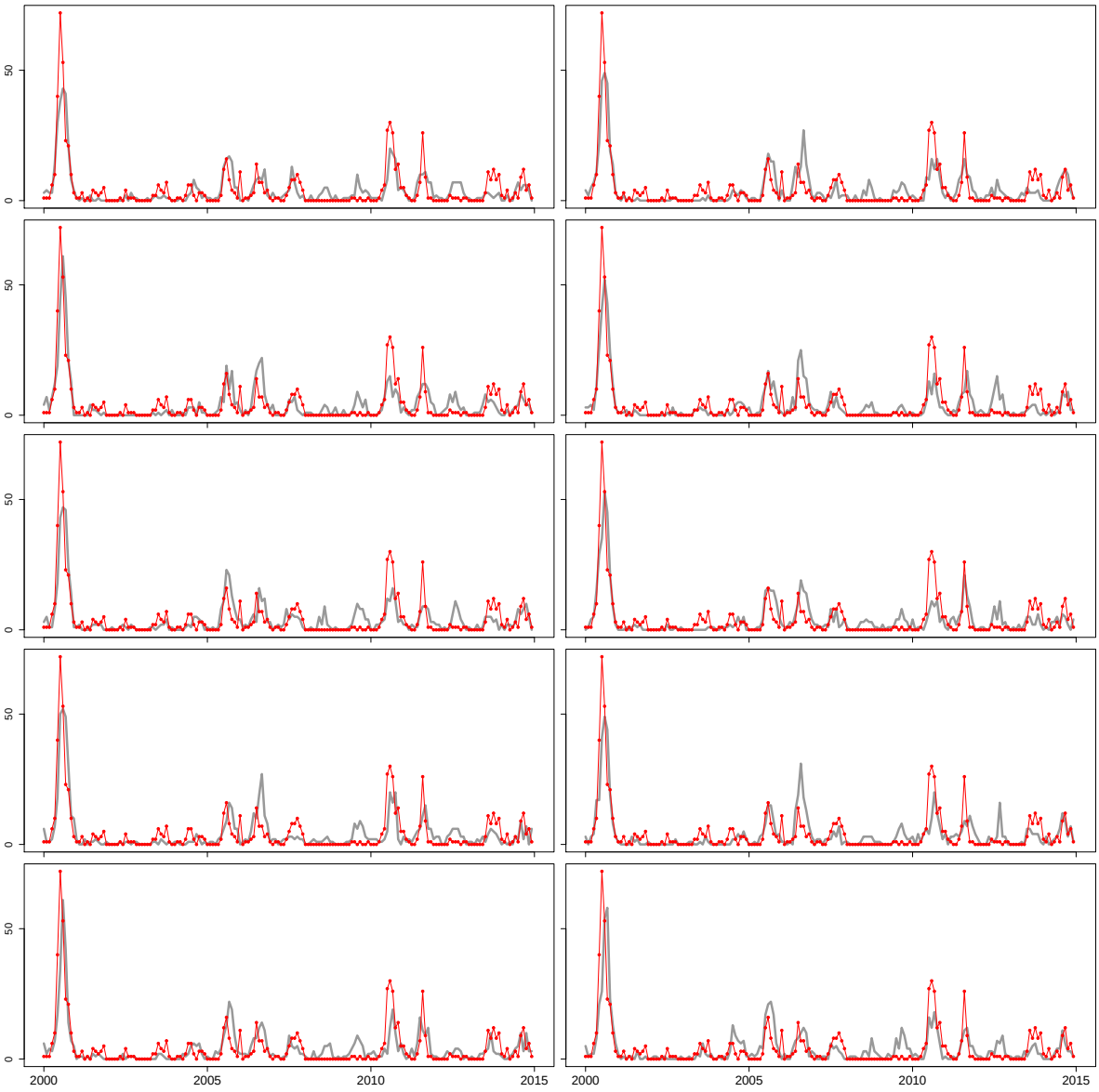

Fig. S29: Variability in the simulated realizations of the fitted model for E25 obtained with the MLE. The observed number of monthly reported isolations (red line) and 10 stochastic realizations of the fitted model out of 100 for the MLE of the parameters (gray lines) are shown. From left to right, top to bottom, the 10 realizations shown correspond to the multiples of ten in the rank of their respective increasing sum of squared residuals (SSR): 10th, 20th,...,100th.

Fig. S30.

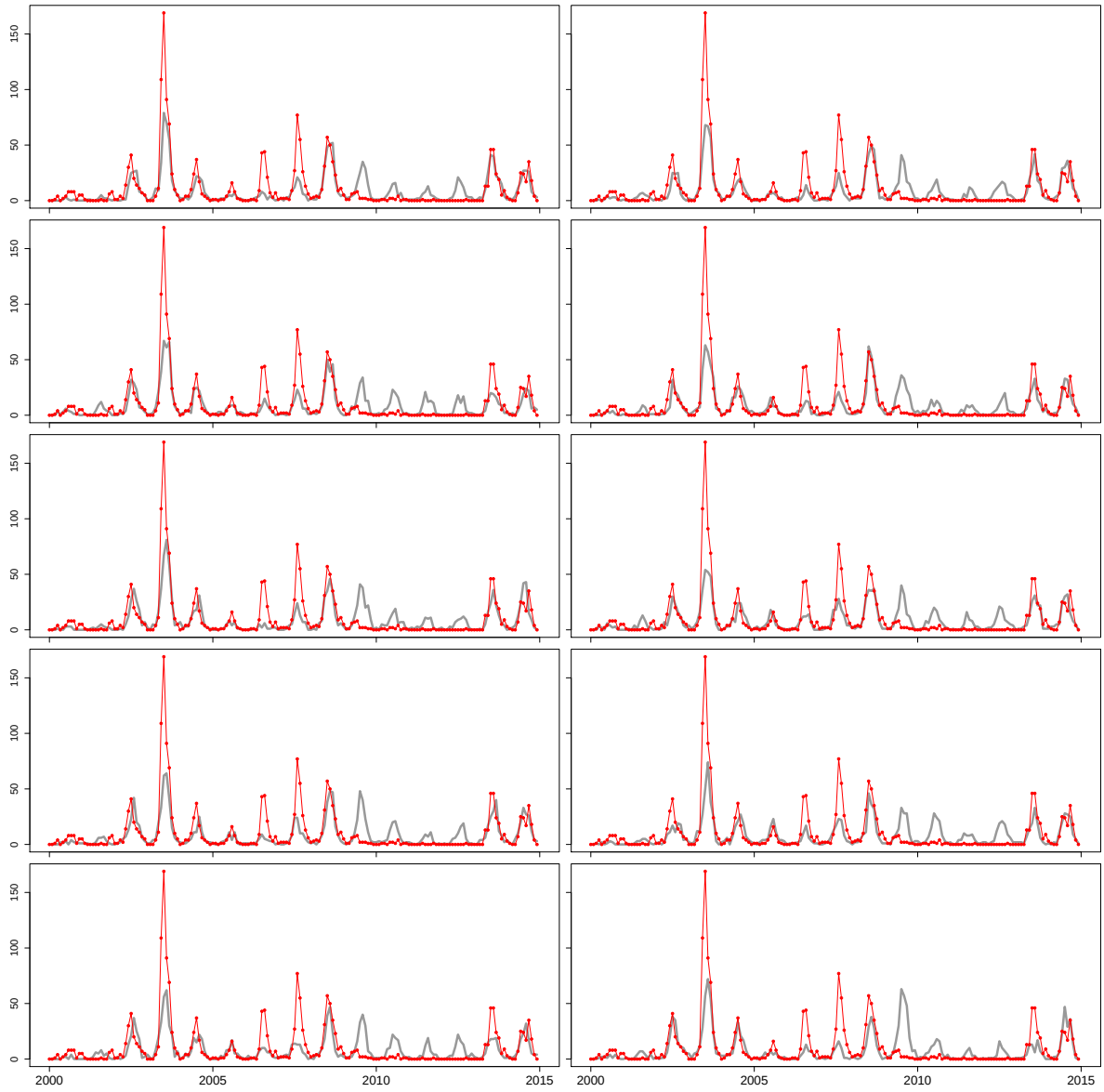

Fig. S30: Variability in the simulated realizations of the fitted model for E30 obtained with the MLE. The observed number of monthly reported isolations (red line) and 10 stochastic realizations of the fitted model out of 100 for the MLE of the parameters (gray lines) are shown. From left to right, top to bottom, the 10 realizations shown correspond to the multiples of ten in the rank of their respective increasing sum of squared residuals (SSR): 10th, 20th,...,100th.

Fig. S31.

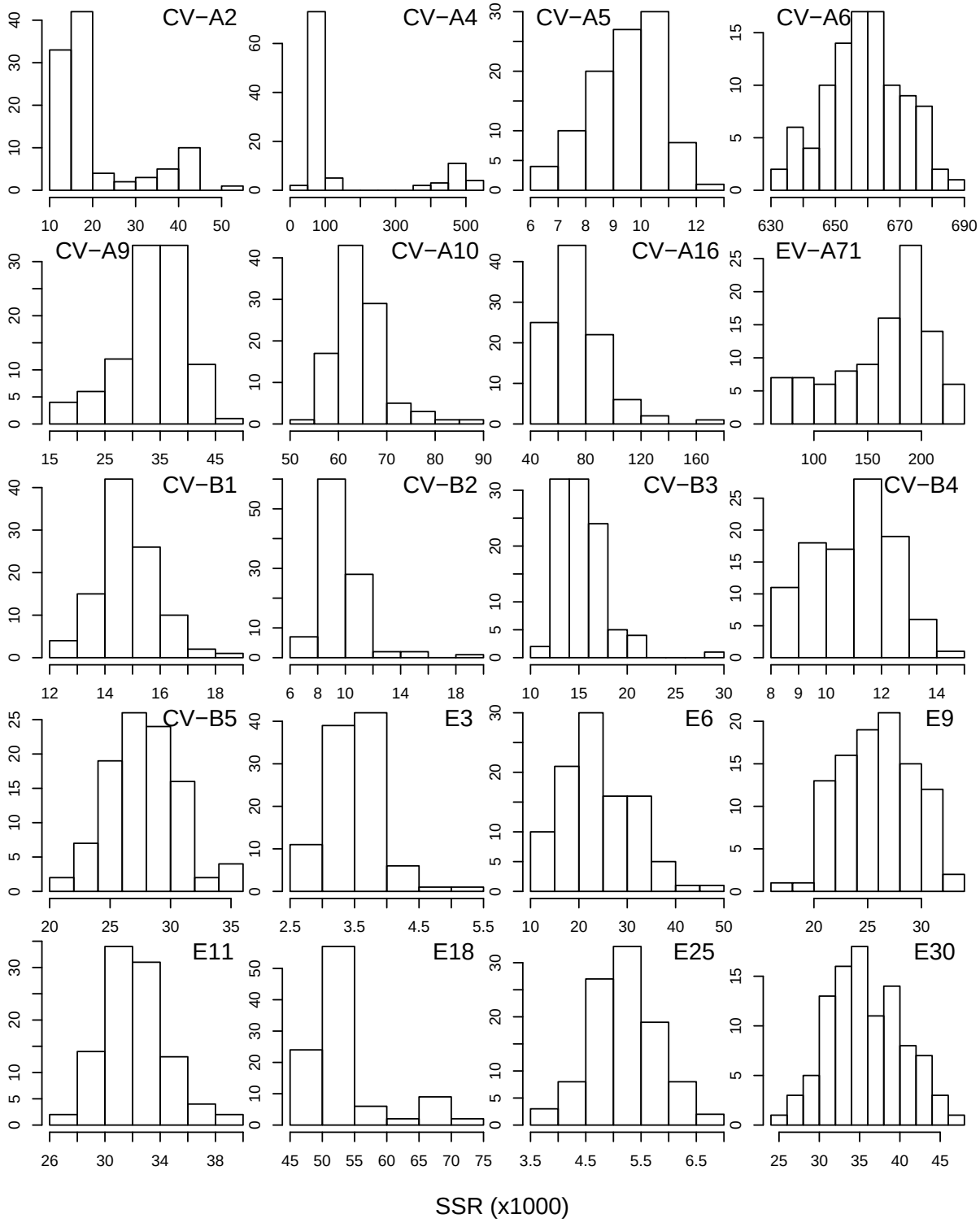

Fig. S31: Histogram of the sum of squared residuals (SSR) for 100 stochastic realizations of the model with the MLE for each serotype.

Fig. S32.

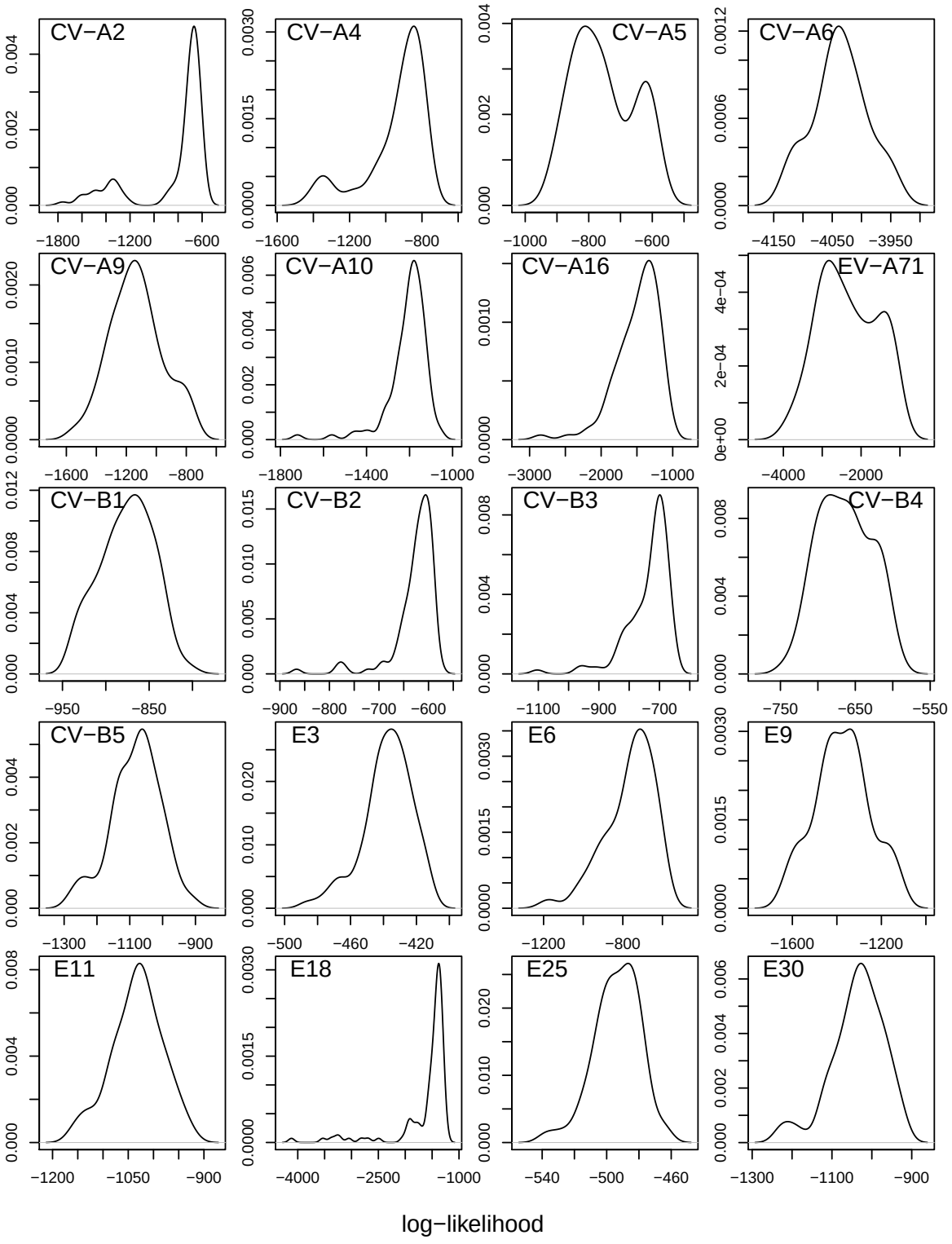

Fig. S32: Likelihood of the simulations given the data for 100 stochastic realizations of the model with the MLE for each serotype.

Fig. S33.

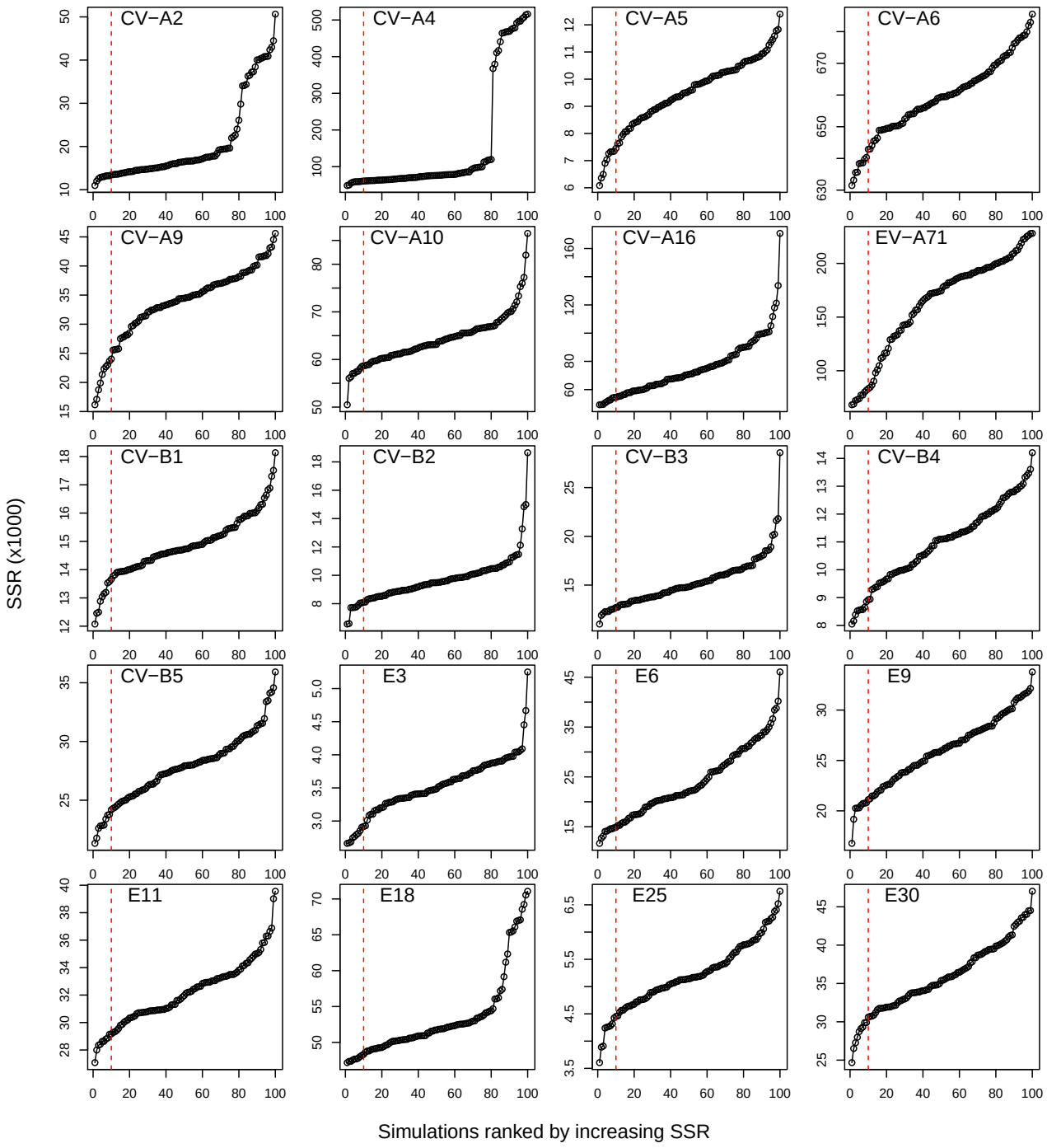

Fig. S33: Increasing curve of the sum of squared residuals (SSR) for 100 stochastic realizations of the model with the MLE for each serotype. The dashed red line indicates the 10th simulation in the rank of increasing SSR.

Fig. S34.

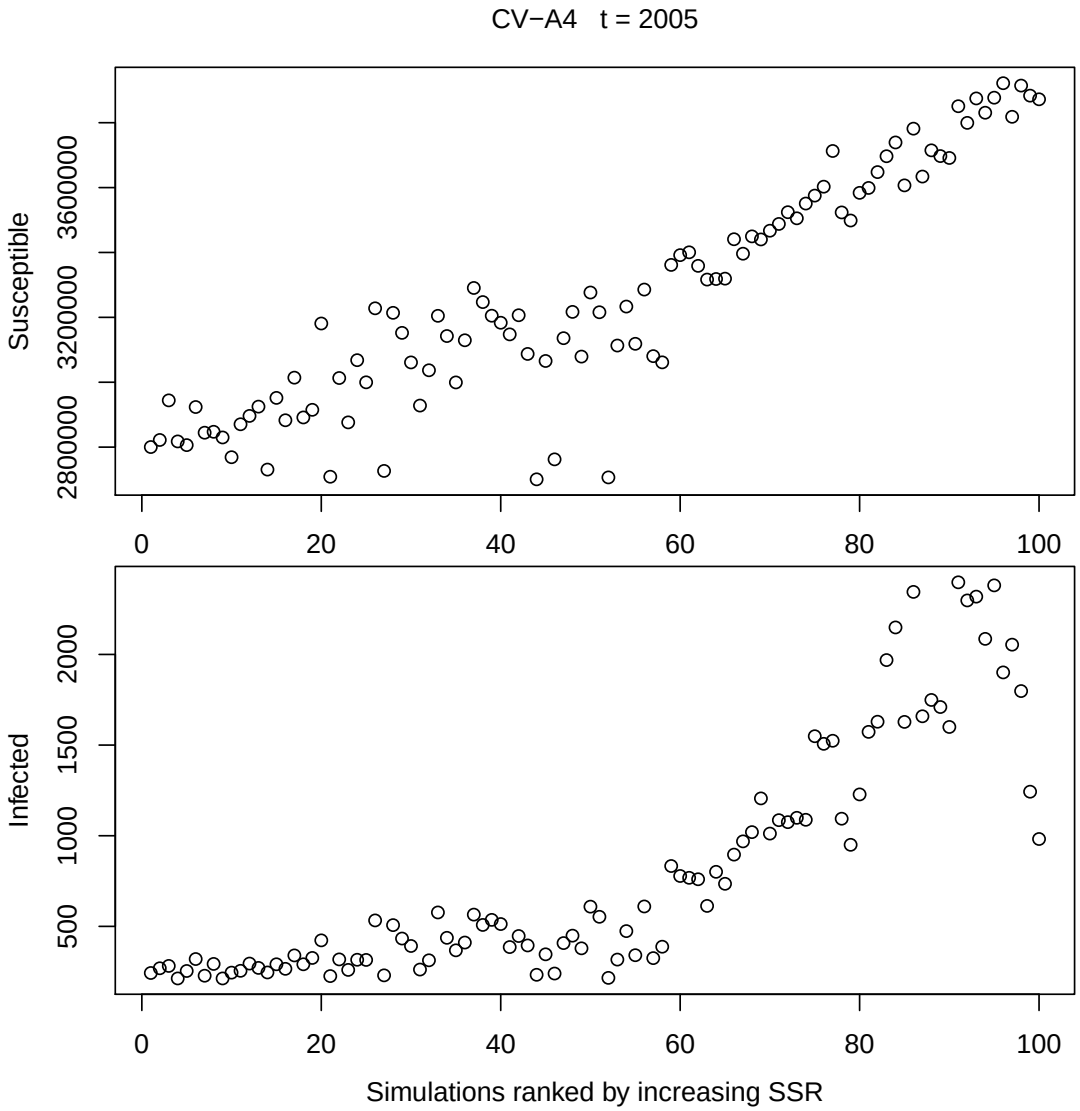

Fig. S34: Number of susceptible (top) and infected individuals (bottom) in January 2005 for each of the 100 stochastic realizations of the model with the MLE of the parameters for CV-A4. The simulations are ordered by increasing value of the sum of squared residuals (SSR).

Fig. S35.

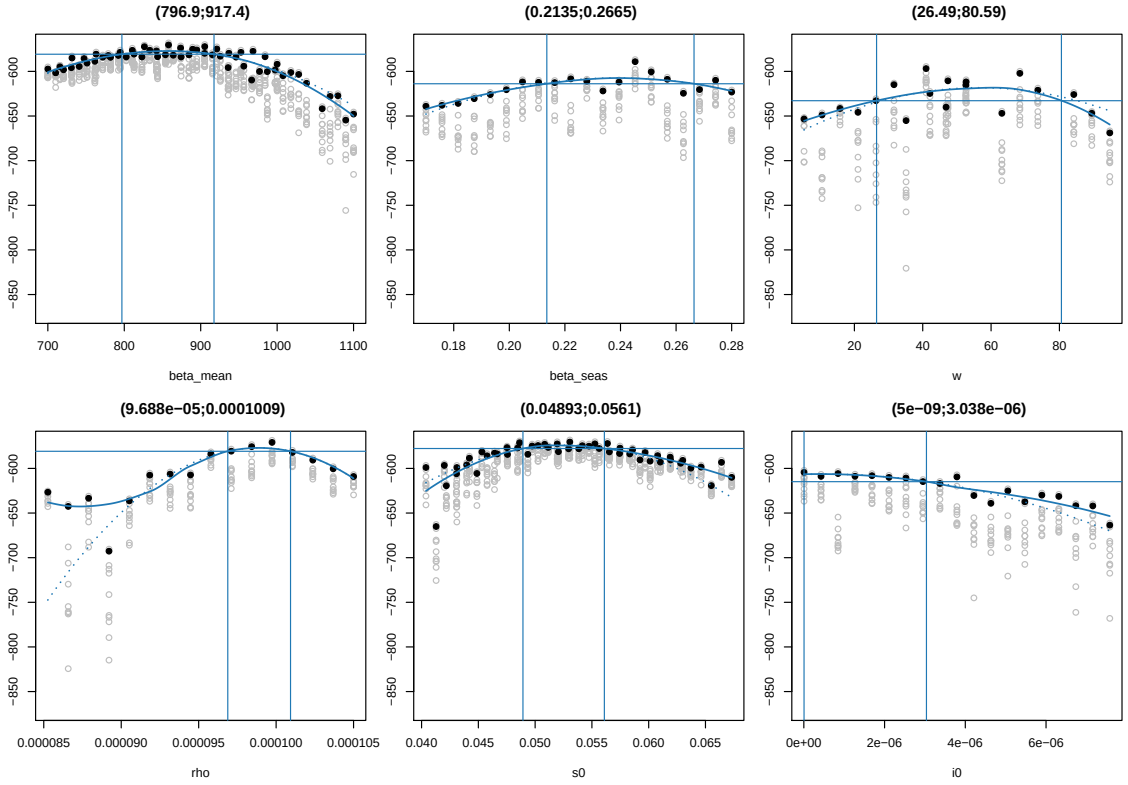

Fig. S35: Profile likelihoods for the parameters corresponding to CV-A2. Each point represents the maximized log-likelihood at each fixed value of the parameter: the black points are the log of the mean likelihoods of 10 replicate filters (gray points). The profiles are created by fitting a smooth line through the black points. The blue vertical lines determine the 99% confidence interval.

Fig. S36.

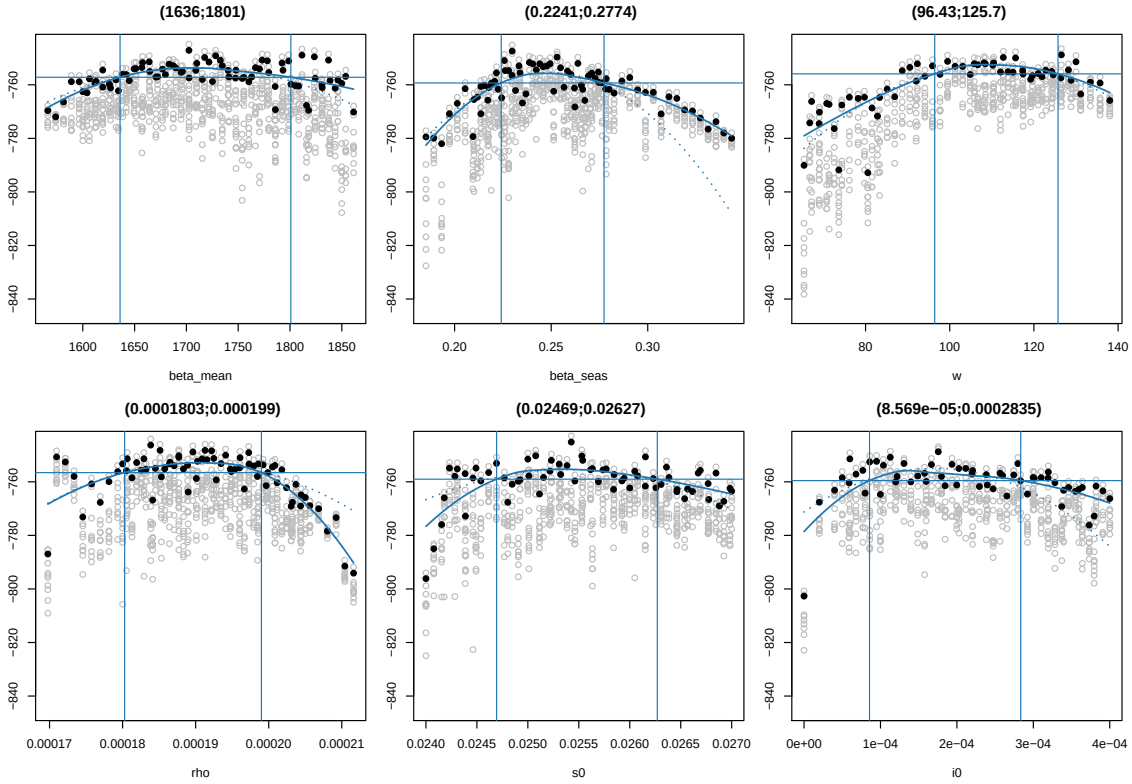

Fig. S36: Profile likelihoods for the parameters corresponding to CV-A4. See details in Fig. S35.

Fig. S37.

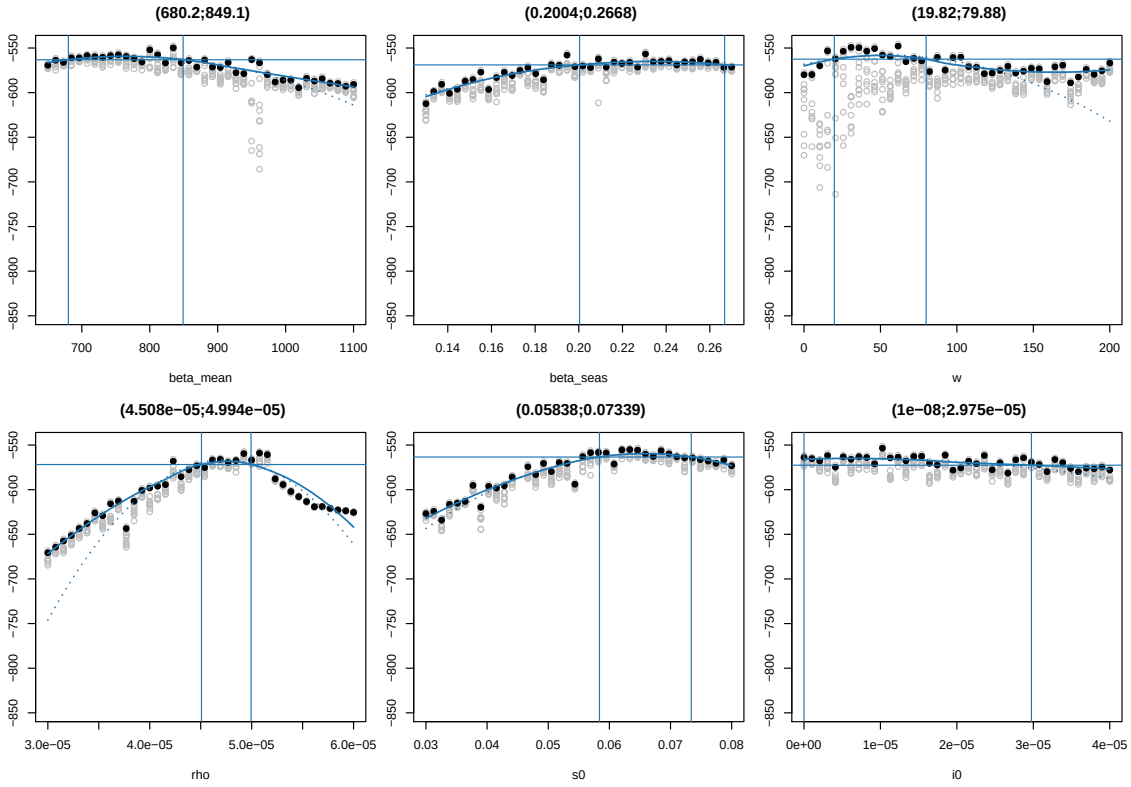

Fig. S37: Profile likelihoods for the parameters corresponding to CV-A5. See details in Fig. S35.

Fig. S38.

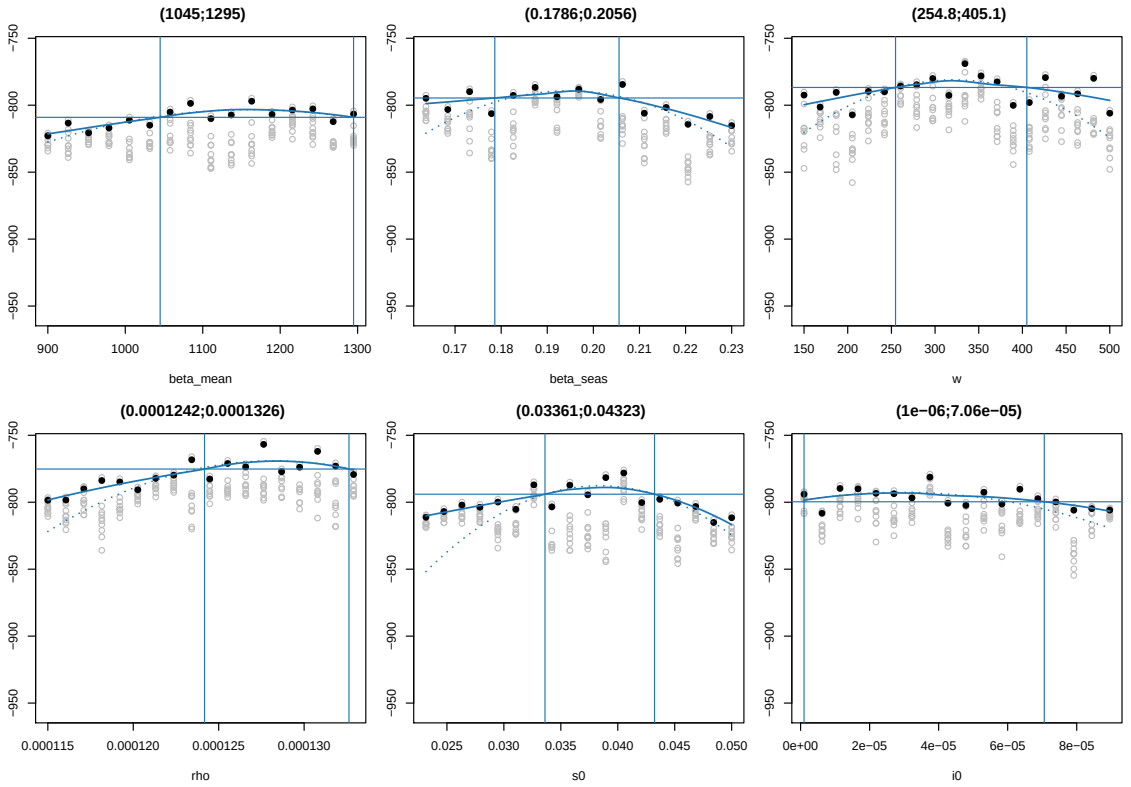

Fig. S38: Profile likelihoods for the parameters corresponding to CV-A6. See details in Fig. S35.

Fig. S39.

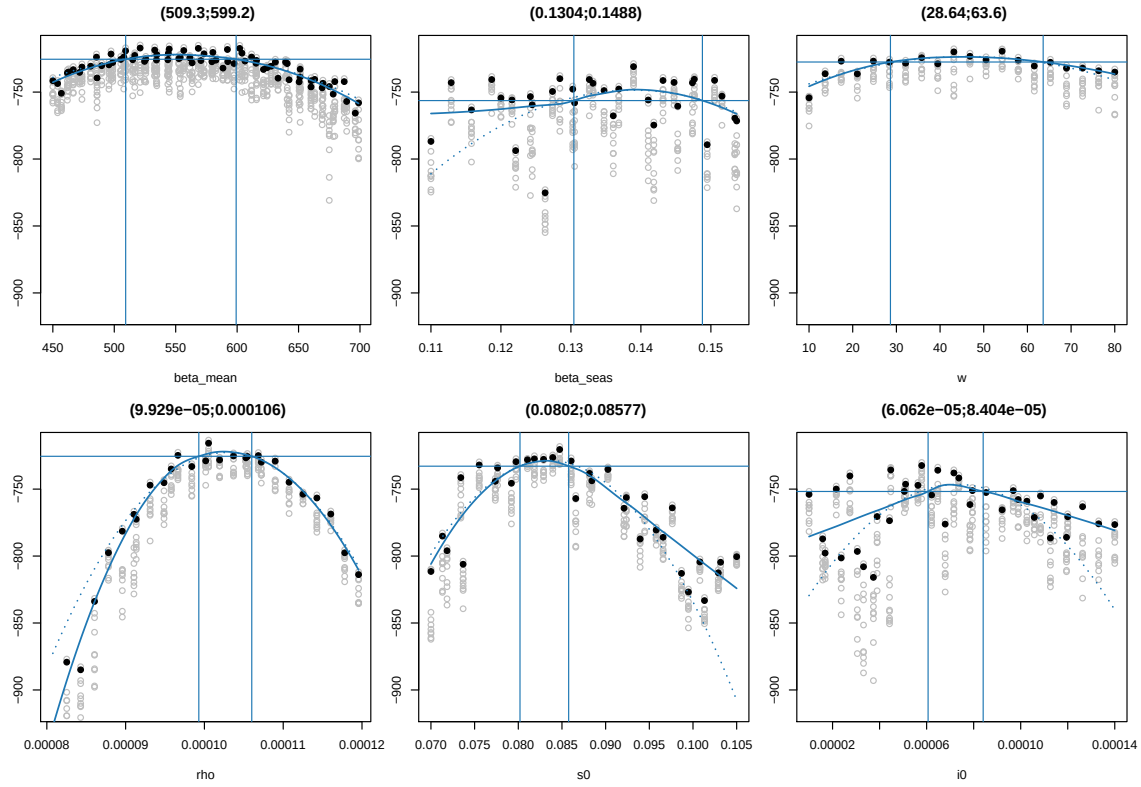

Fig. S39: Profile likelihoods for the parameters corresponding to CV-A9. See details in Fig. S35.

Fig. S40.

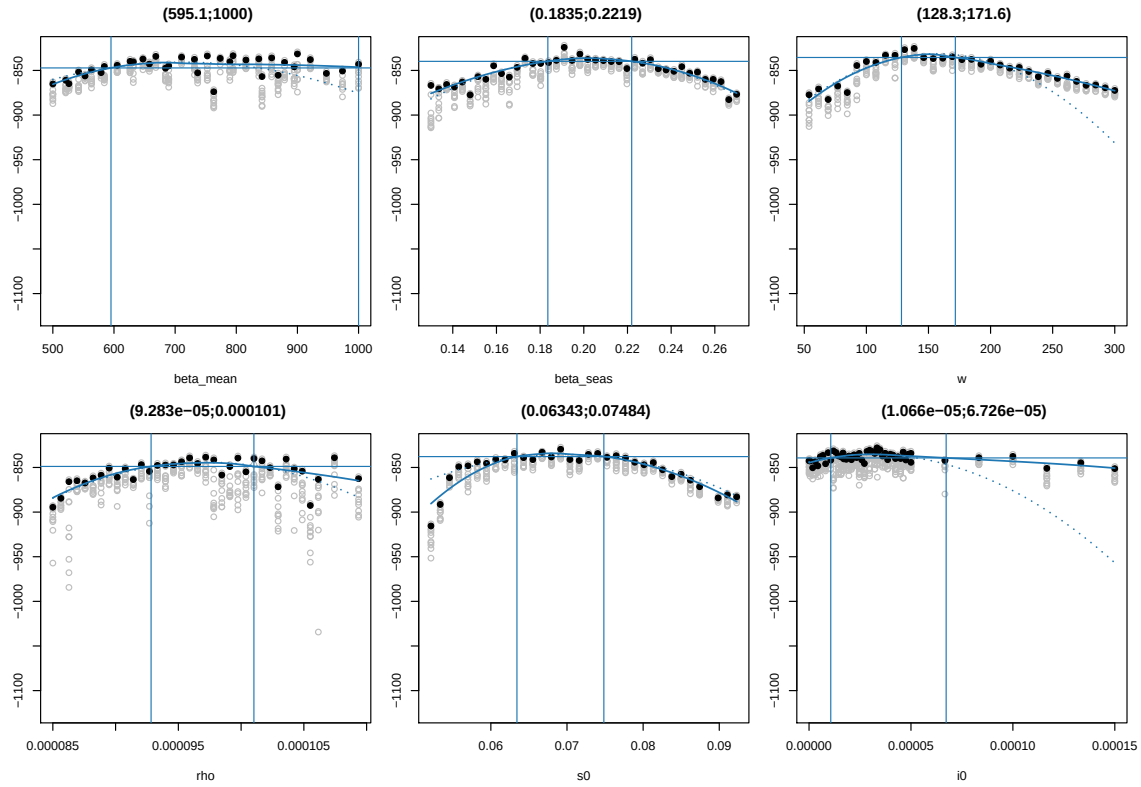

Fig. S40: Profile likelihoods for the parameters corresponding to CV-A10. See details in Fig. S35.

Fig. S41.

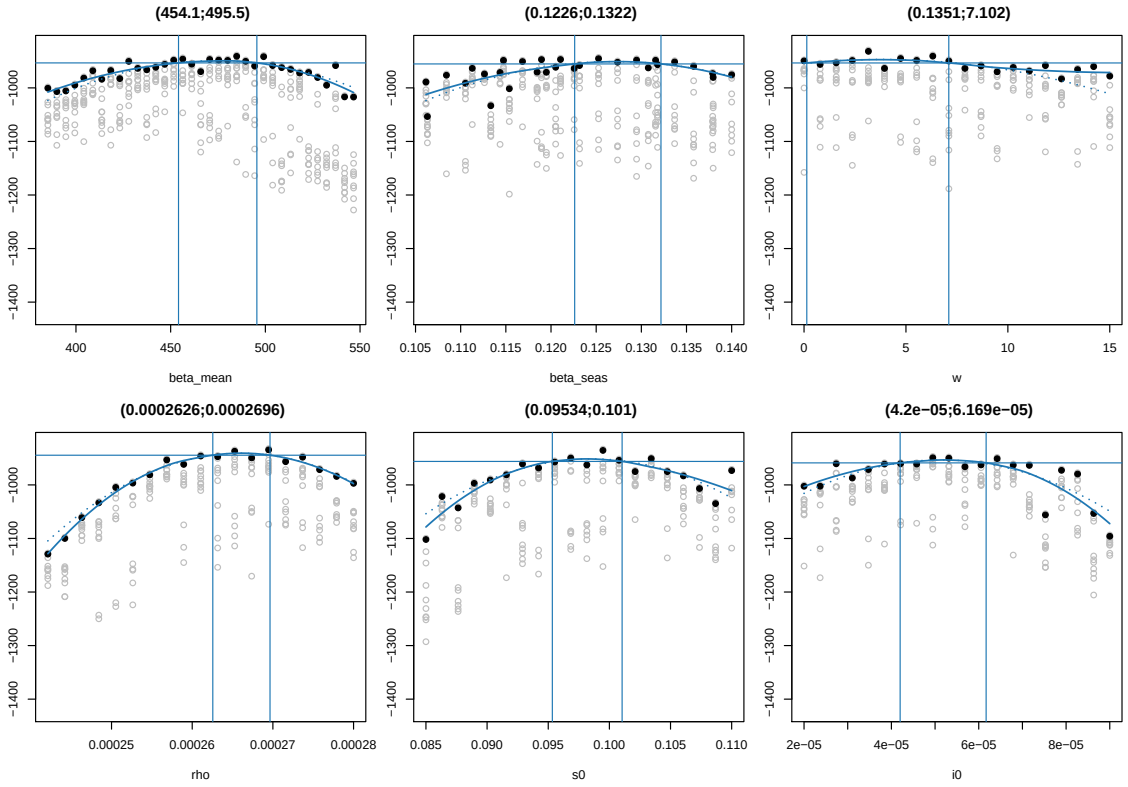

Fig. S41: Profile likelihoods for the parameters corresponding to CV-A16. See details in Fig. S35.

Fig. S42.

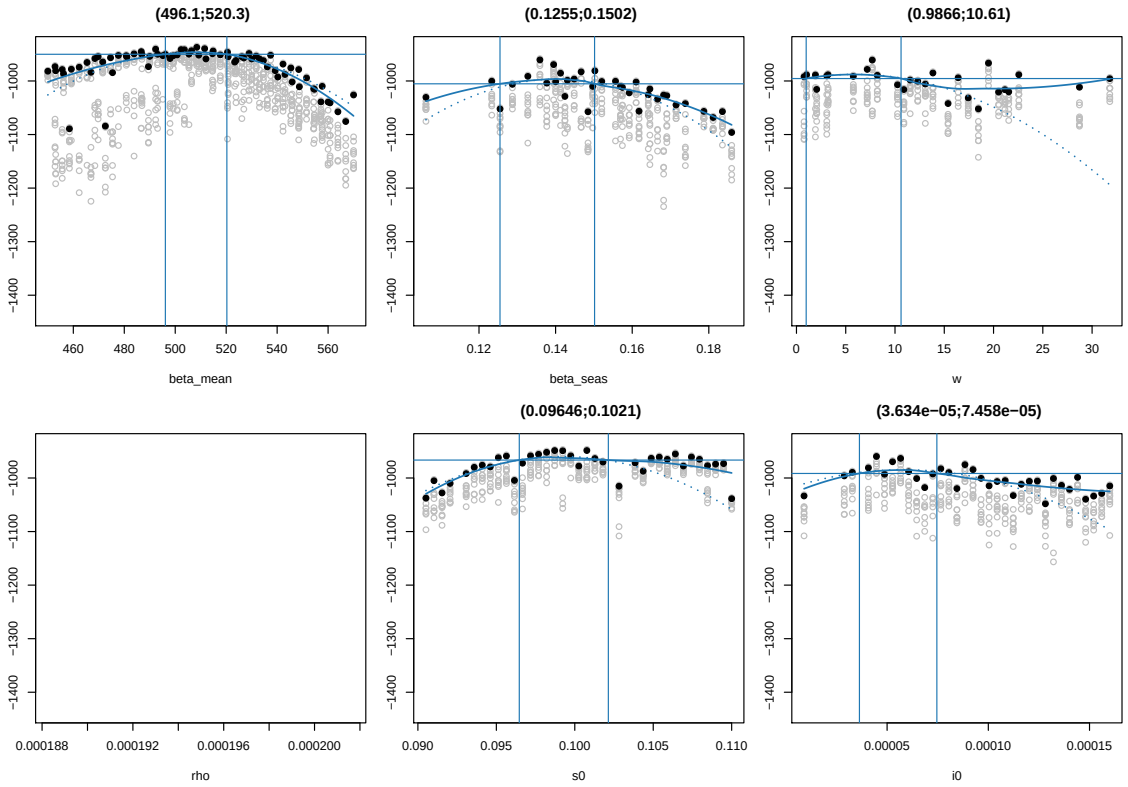

Fig. S42: Profile likelihoods for the parameters corresponding to EV-A71. See details in Fig. S35.

Fig. S43.

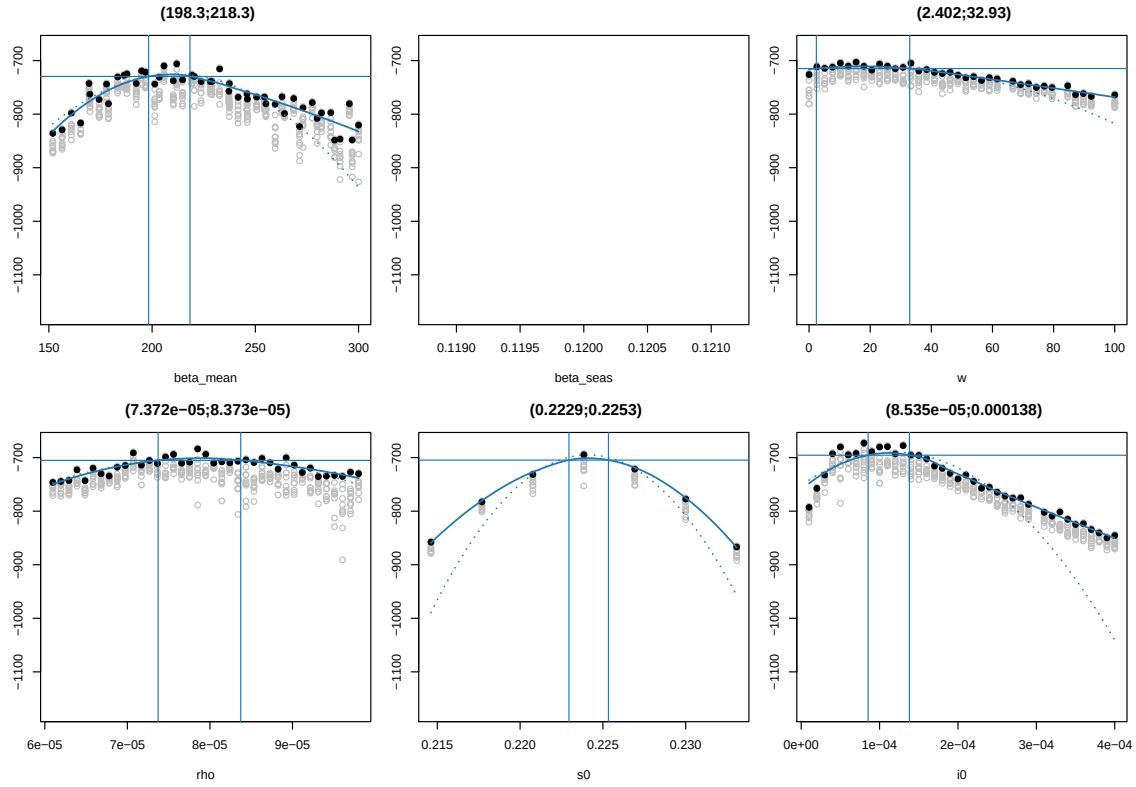

Fig. S43: Profile likelihoods for the parameters corresponding to CV-B1. Due to bimodality issues, to obtain those of w, ρ s_0 and i_0, we fixed β_m and β_s at their MLEs ($\beta_m = 178$ and $\beta_s = 0.12$). See details in Fig. S35.

Fig. S44.

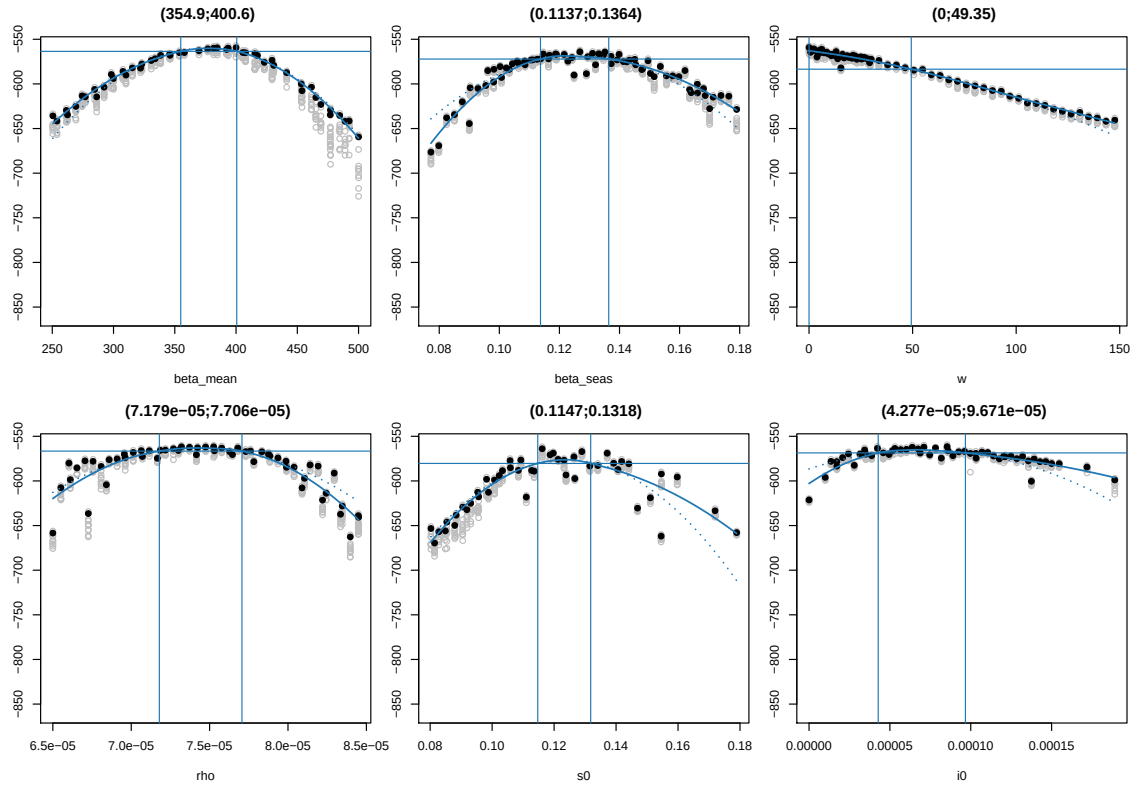

Fig. S44: Profile likelihoods for the parameters corresponding to CV-B2. See details in Fig. S35.

Fig. S45.

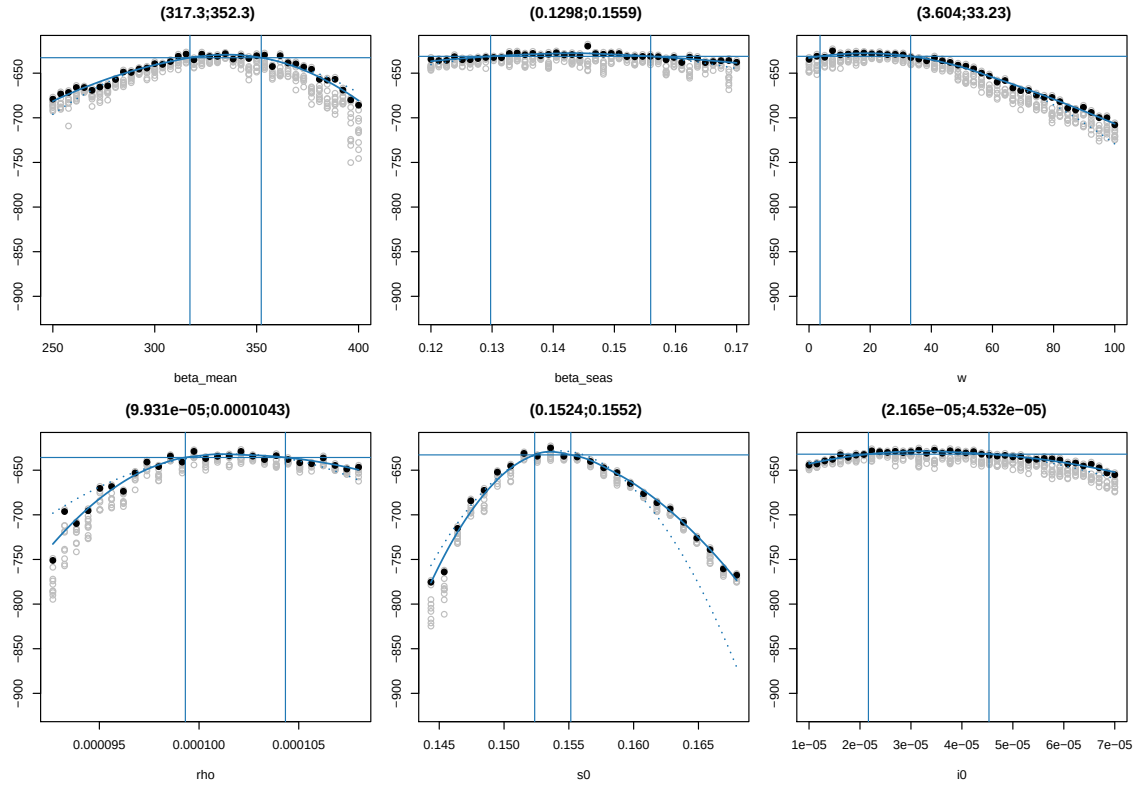

Fig. S45: Profile likelihoods for the parameters corresponding to CV-B3. To obtain those of β_s, w, s_0 and i_0, we had to fix β_m to reach maximization ($\beta_m = 330$). See details in Fig. S35.

Fig. S46.

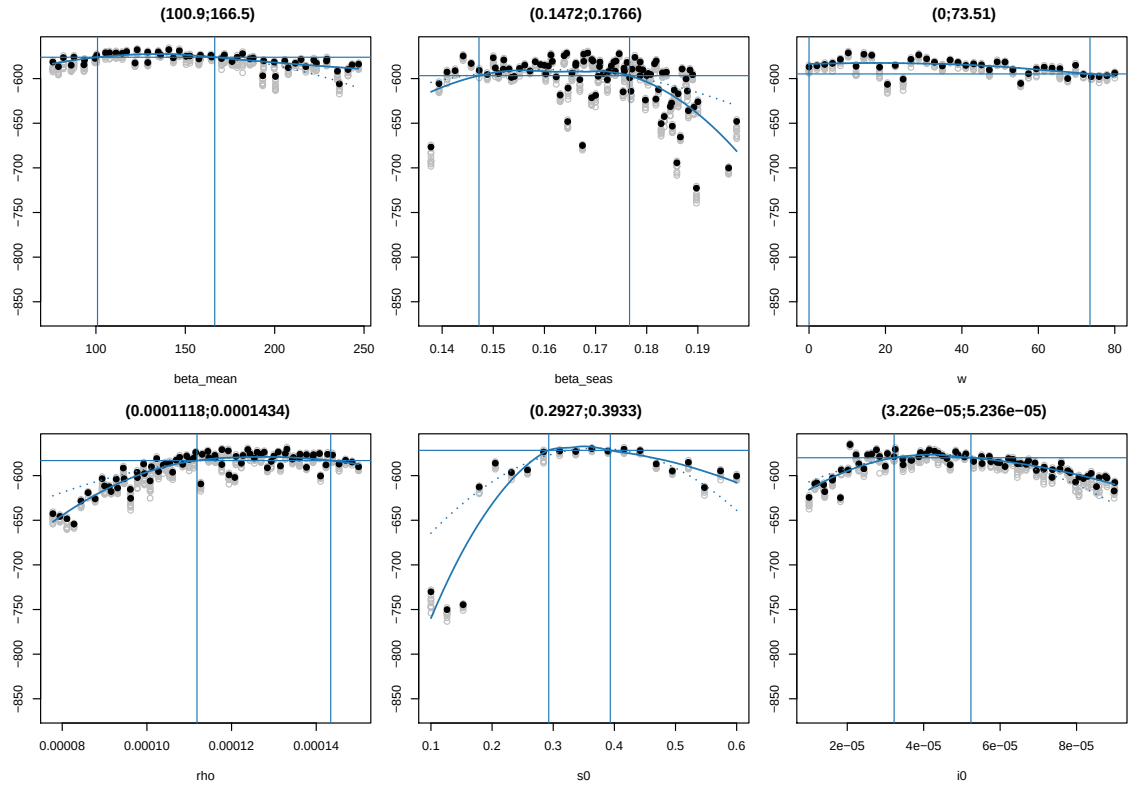

Fig. S46: Profile likelihoods for the parameters corresponding to CV-B4. See details in Fig. S35.

Fig. S47.

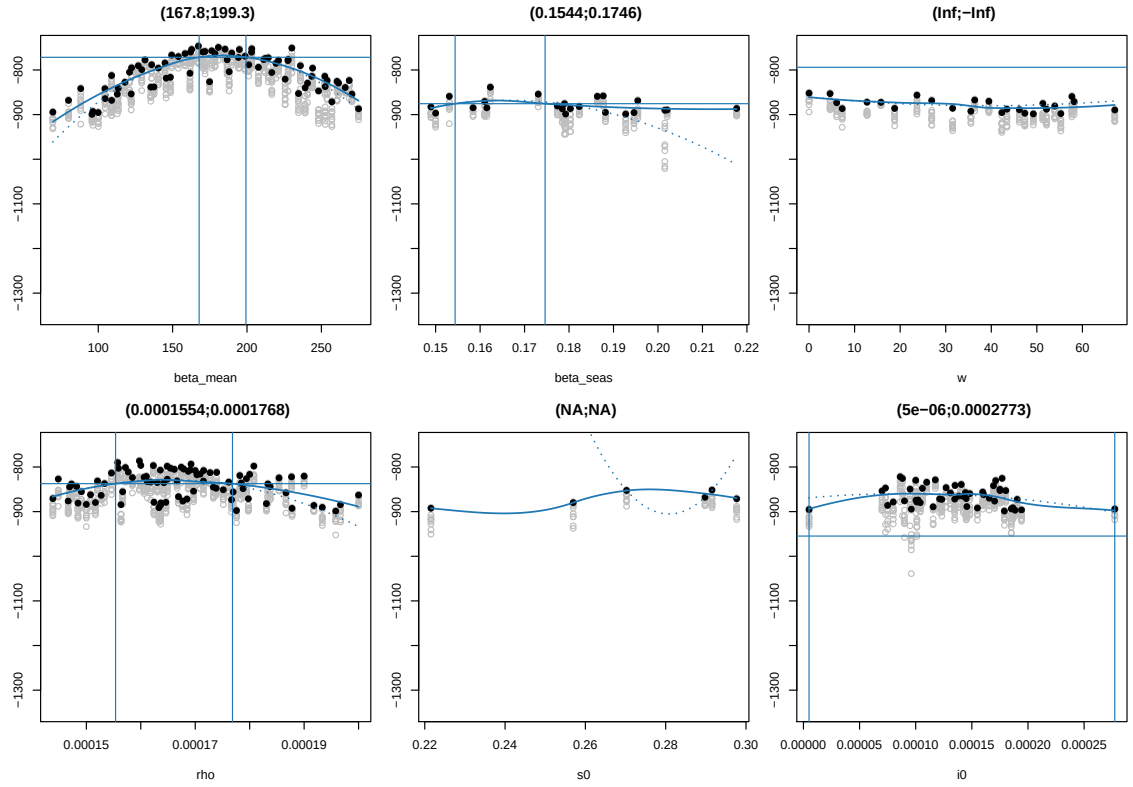

Fig. S47: Profile likelihoods for the parameters corresponding to CV-B5. See details in Fig. S35.

Fig. S48.

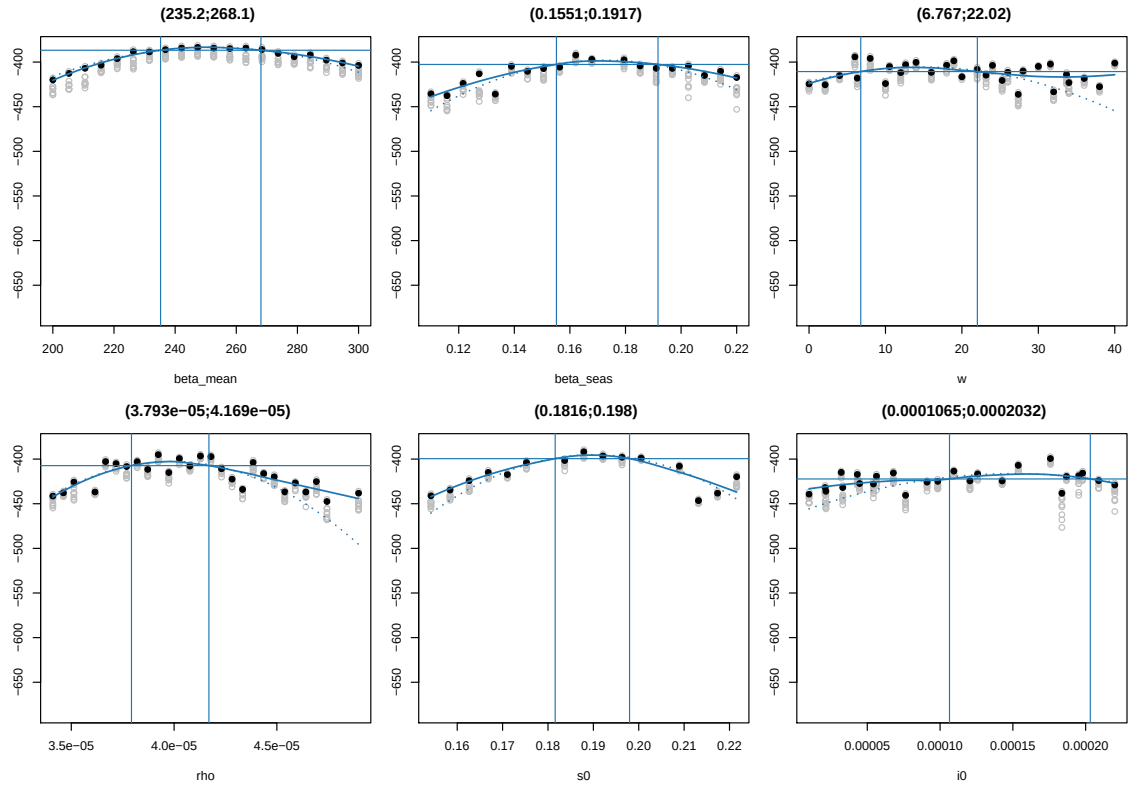

Fig. S48: Profile likelihoods for the parameters corresponding to E3. See details in Fig. S35.

Fig. S49.

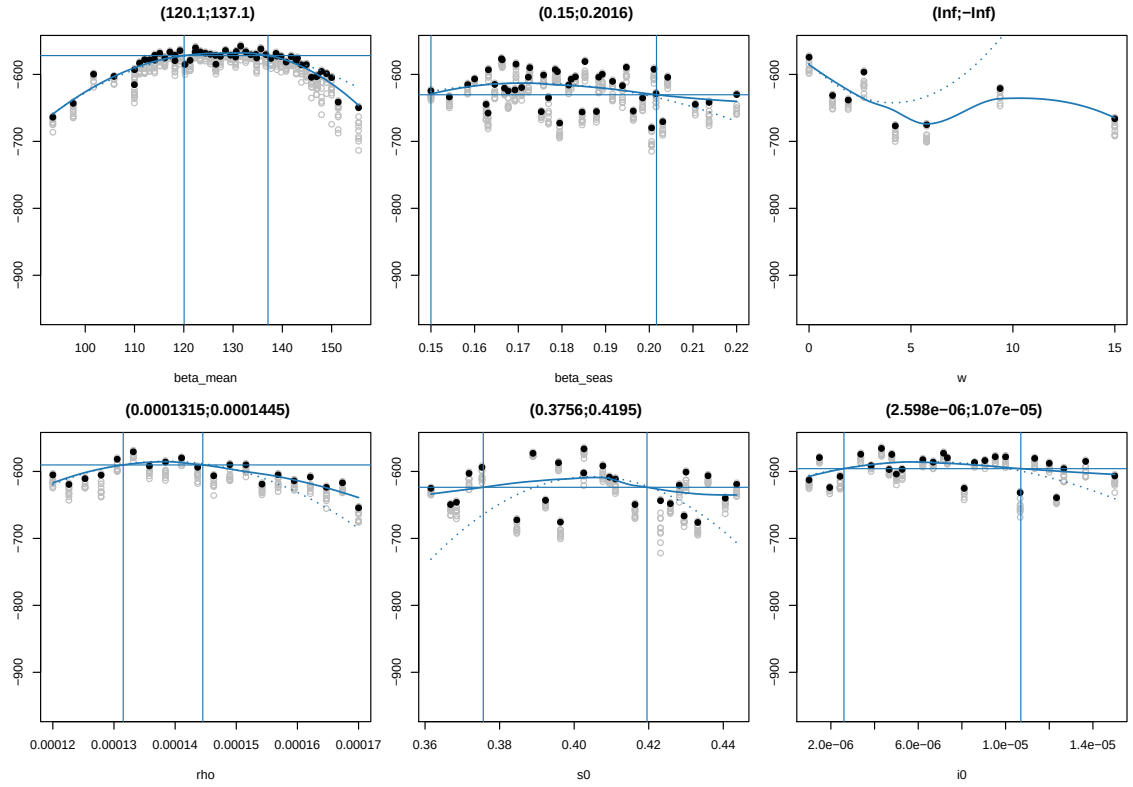

Fig. S49: Profile likelihoods for the parameters corresponding to E6. See details in Fig. S35.

Fig. S50.

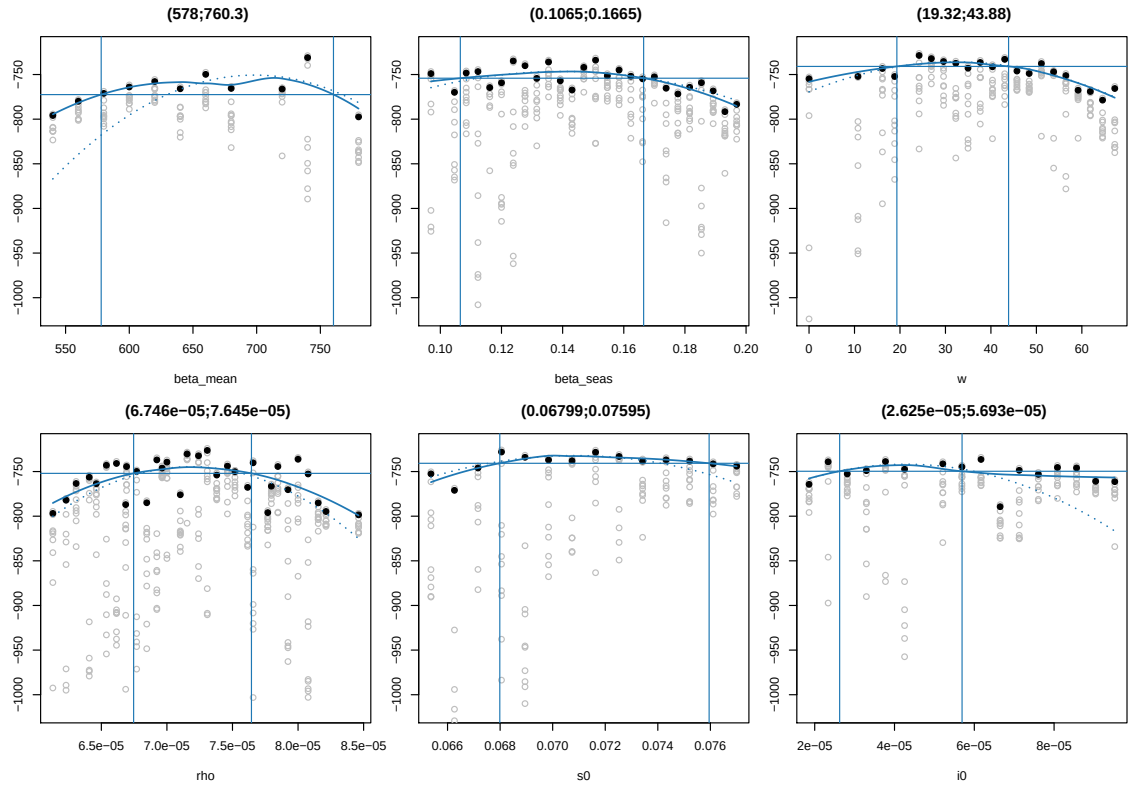

Fig. S50: Profile likelihoods for the parameters corresponding to E9. See details in Fig. S35.

Fig. S51.

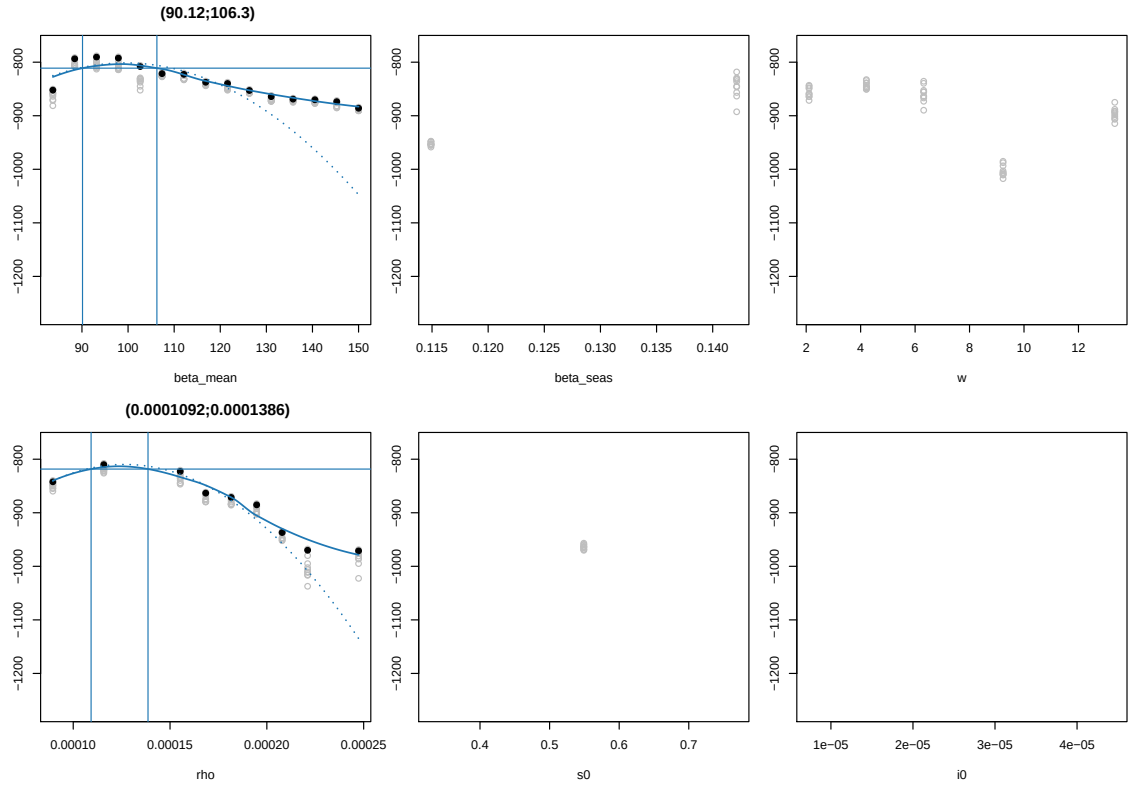

Fig. S51: Profile likelihoods for the parameters corresponding to E11. See details in Fig. S35.

Fig. S52.

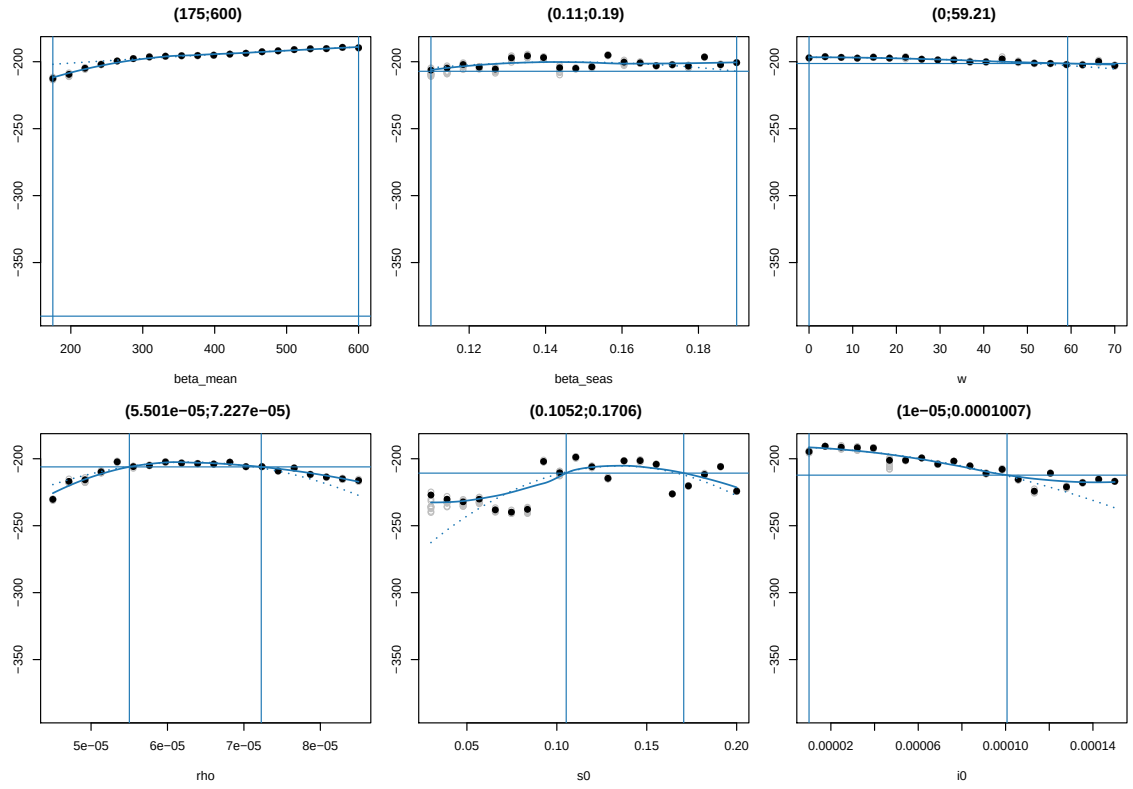

Fig. S52: Profile likelihoods for the parameters corresponding to E18. See details in Fig. S35.

Fig. S53.

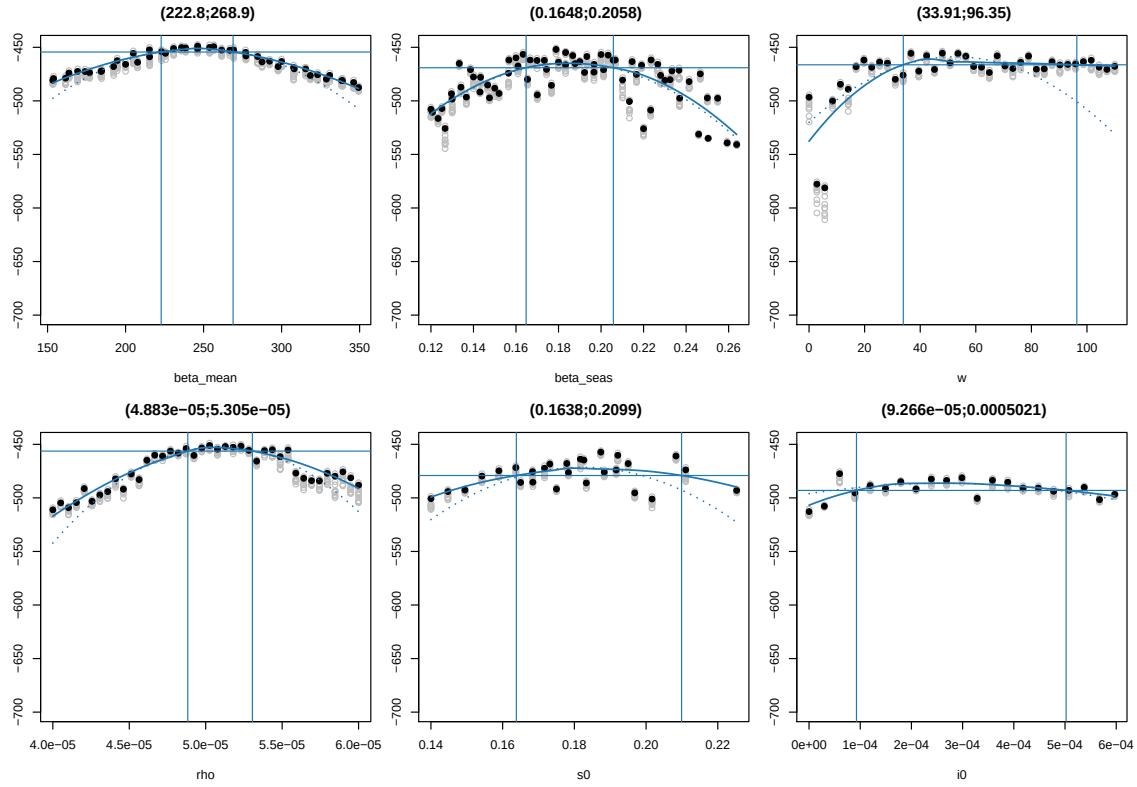

Fig. S53: Profile likelihoods for the parameters corresponding to E25. See details in Fig. S35.

Fig. S54.

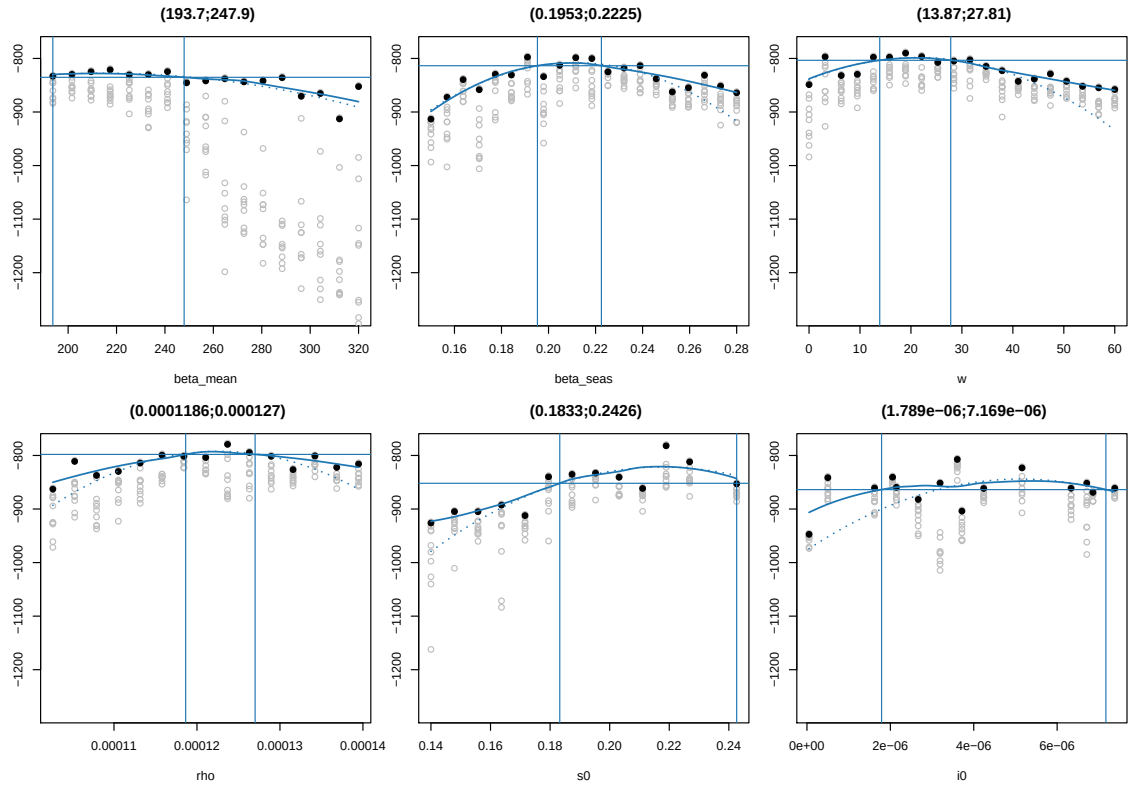

Fig. S54: Profile likelihoods for the parameters corresponding to E30. See details in Fig. S35.

Fig. S55.

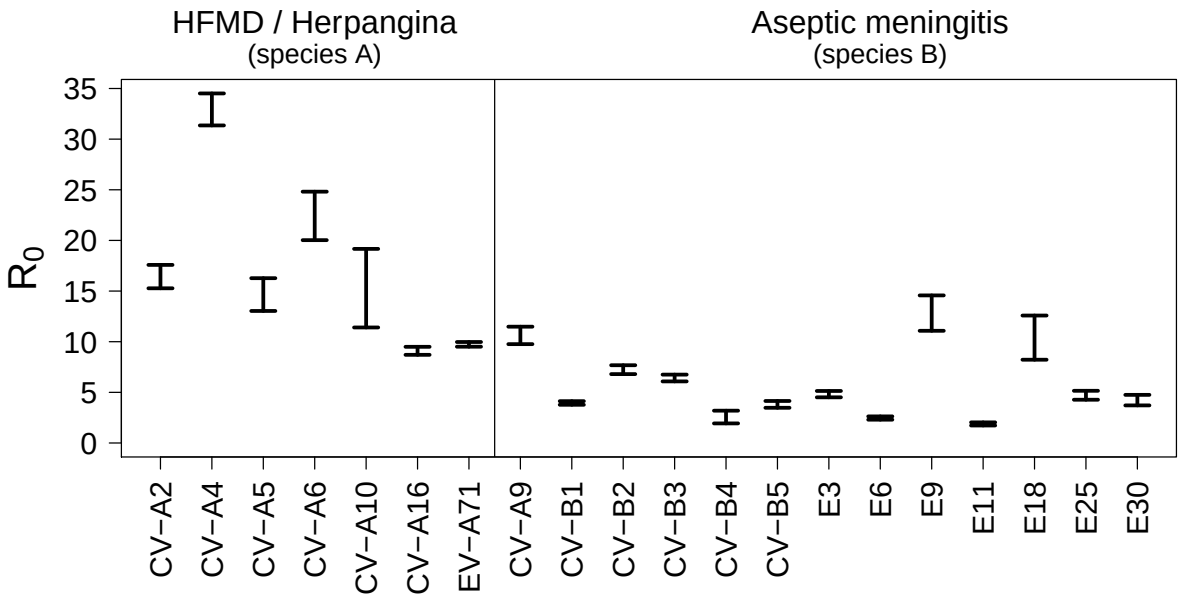

Fig. S55: Estimated basic reproduction numbers. 99% confidence intervals of the estimates of the basic reproduction number for each serotype.

Fig. S56.

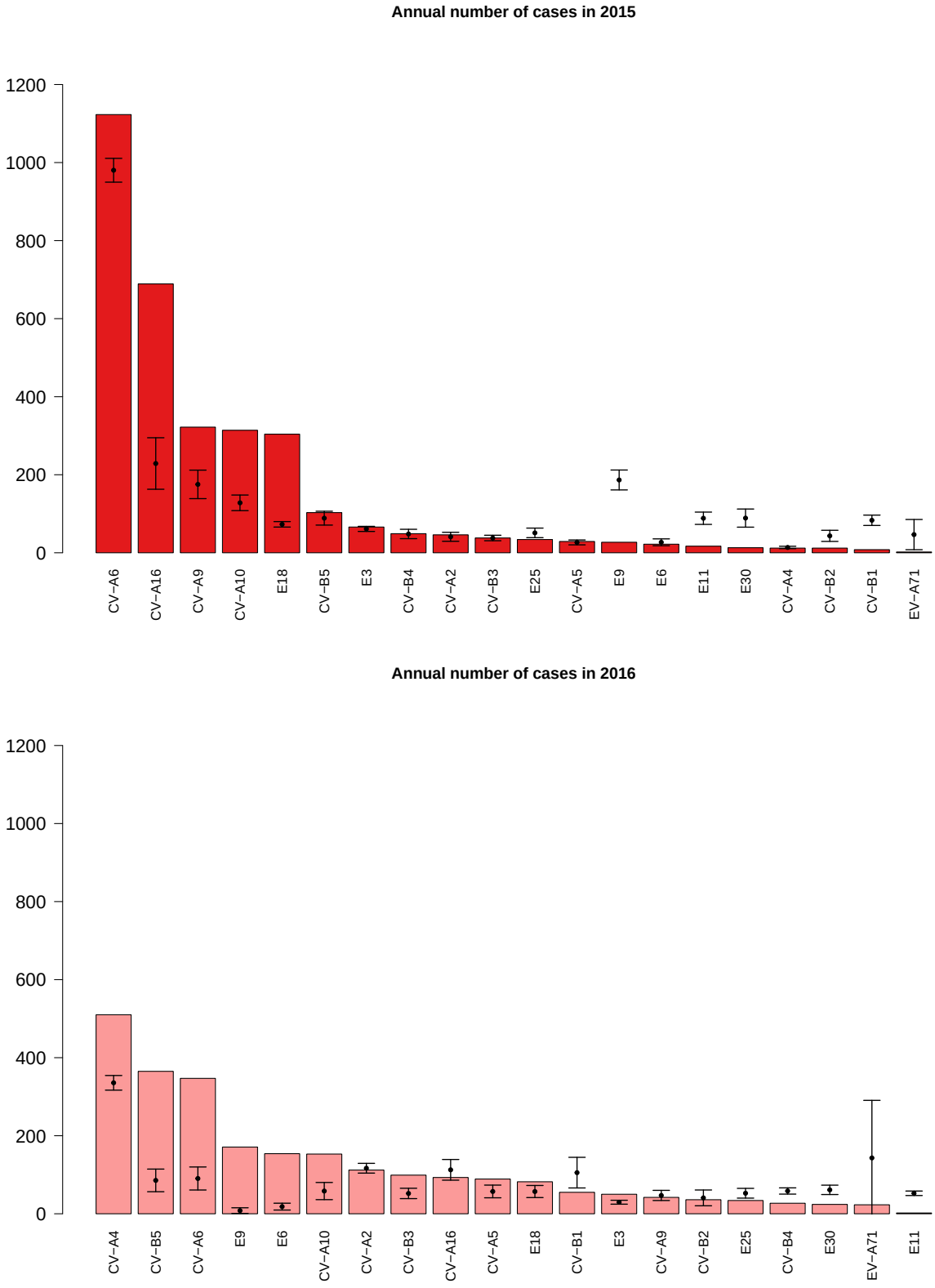

Fig. S56: Out-of-sample predictions. Annual number of cases observed (bars) and predicted (intervals) for 2015 (top) and 2016 (bottom). The intervals are the interquartile range for the 10 best stochastic realizations out of 100 simulated using the MLE. For CV-A6, we used the model with increased pathogenicity (SIR+P), and for E18, the model with an antigenic change (SIR+A).

Fig. S57.

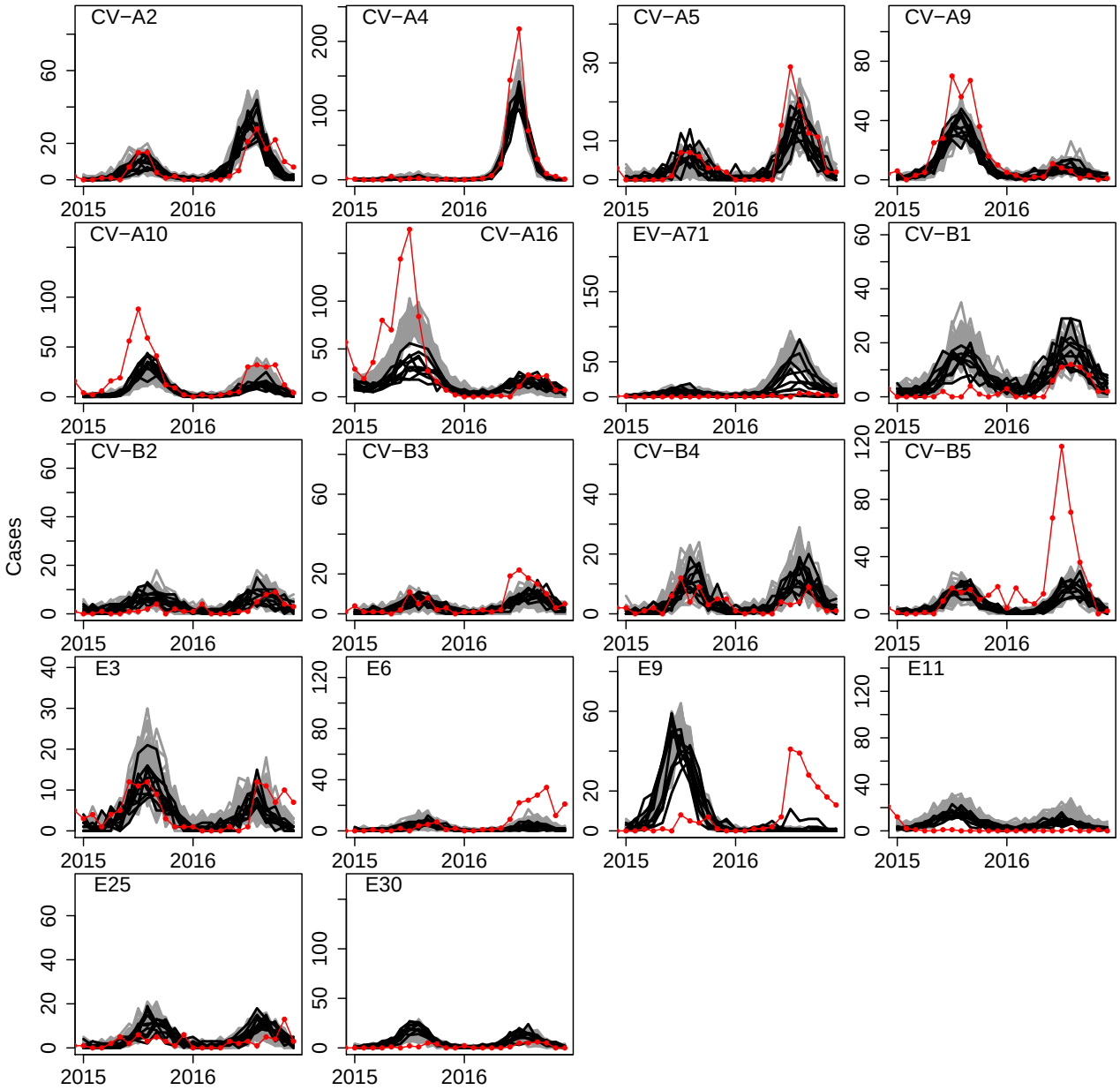

Fig. S57: Comparison of out-of-sample predictions over 2015–2016. In black, 10 out-of-sample predictions obtained by simulating forward from the initial conditions 100 times and selecting the 10 stochastic realizations that fit the data better between January 2000 – December 2014 (these correspond to those shown in Figs. 2 and 3 of the main text). In gray, 100 out-of-sample predictions obtained using the particle filter to reconstruct the state space variables up to December 2014 and simulating the model forward after that. The data is shown in red.

Fig. S58.

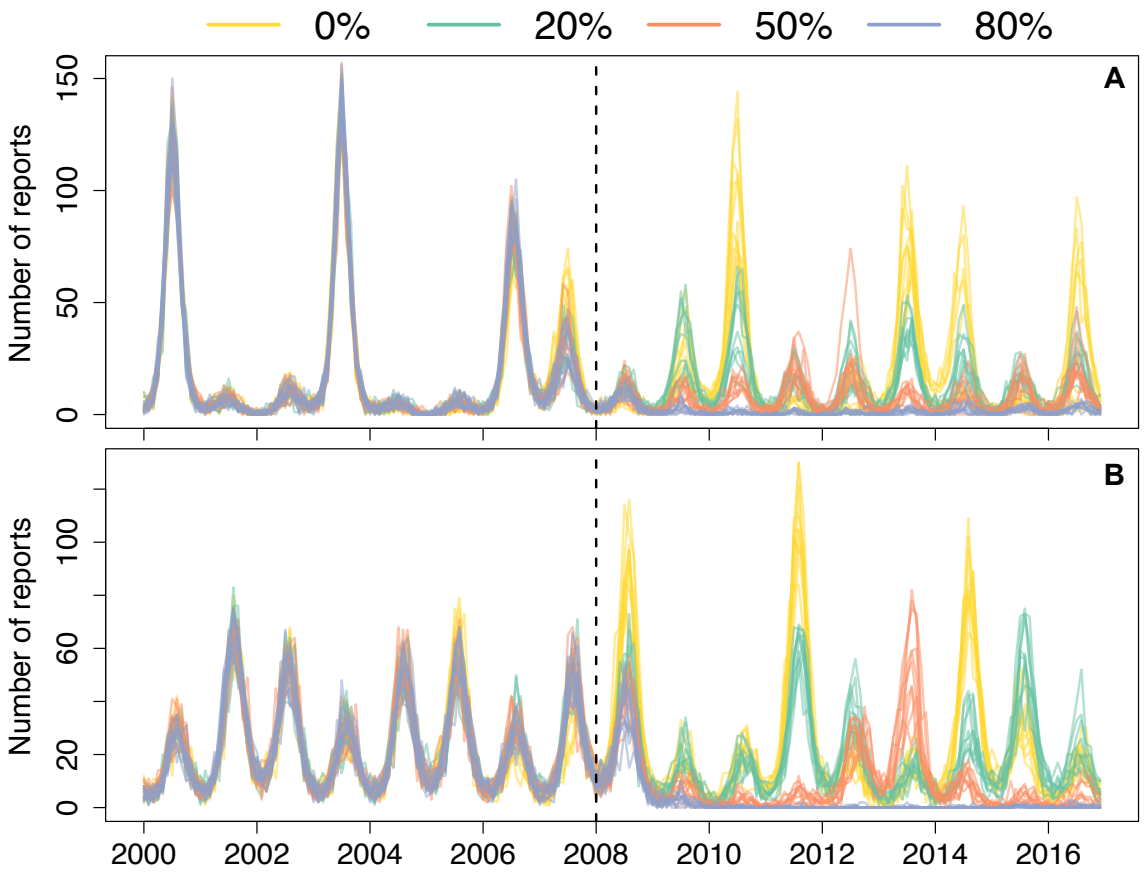

Fig. S58: Simulated vaccination against EV-A71 (A) and CV-A16 (B) for different coverage levels. Vaccination of newborns starts in 2008 (dashed vertical line), and 100% vaccine efficacy against infection and lifelong protection is assumed. Ten stochastic realizations of the model are shown for each value of vaccine coverage.

Fig. S59.

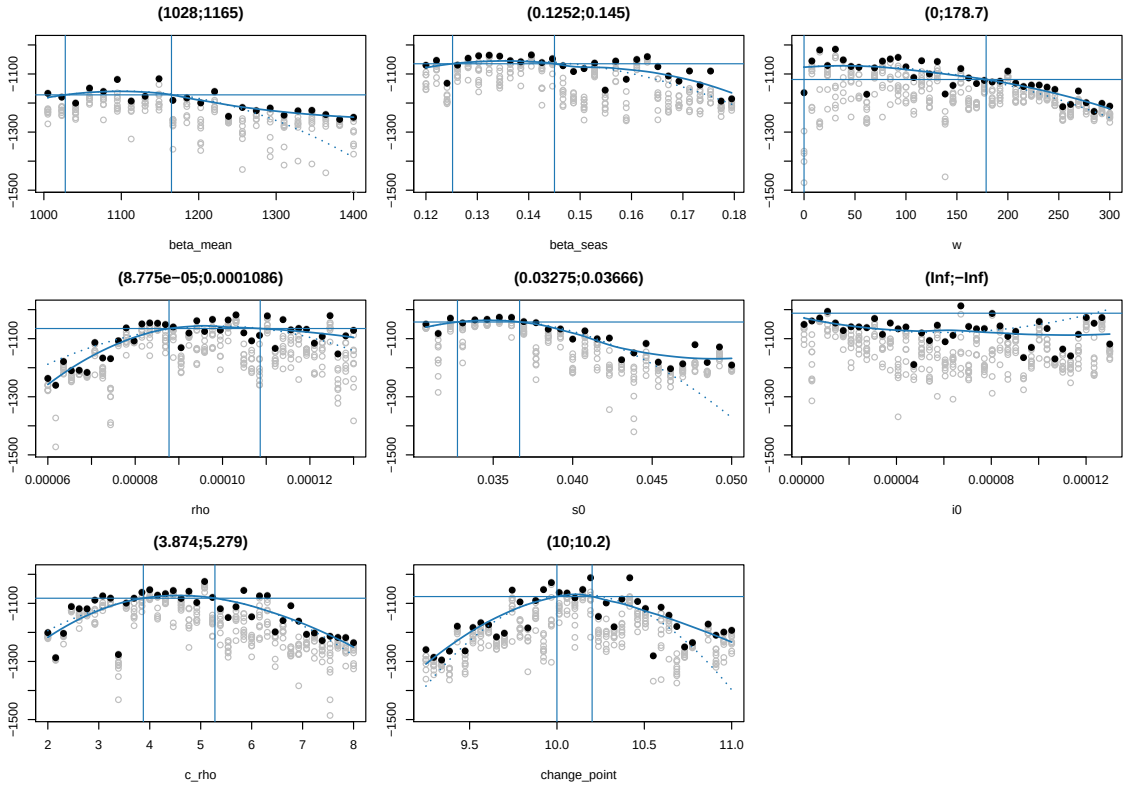

Fig. S59: Profile likelihoods for the parameters corresponding to the model extension SIR+P for serotype CV-A6. The parameter change point is given in number of years after 2000.

Fig. S60.

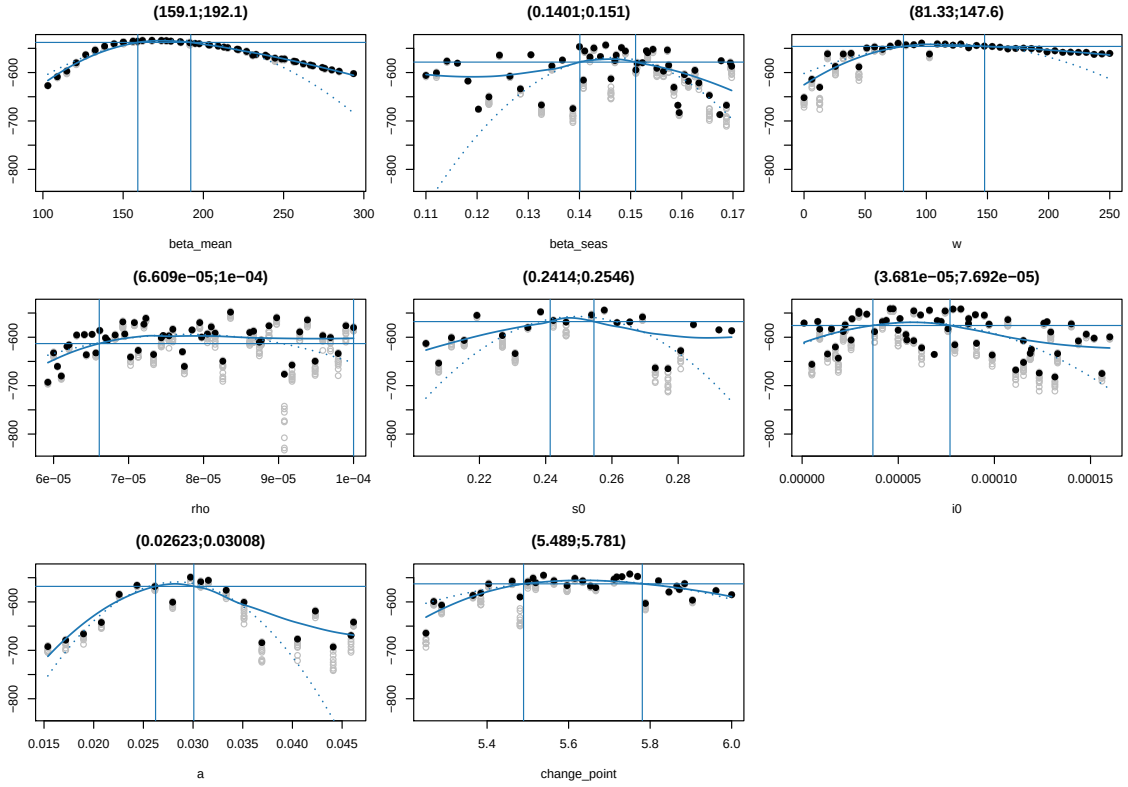

Fig. S60: Profile likelihoods for the parameters corresponding to the model extension SIR+A for serotype E18. The parameter change point is given in number of years after 2000.

Fig. S61.

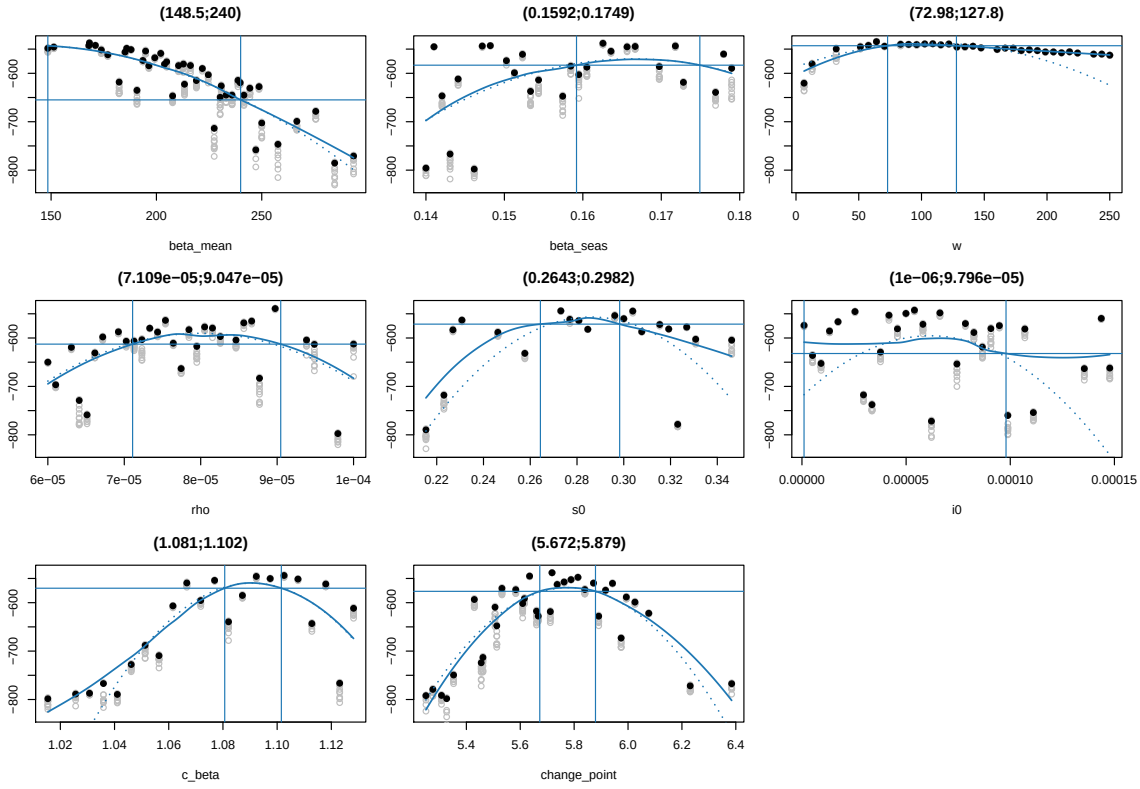

Fig. S61: Profile likelihoods for the parameters corresponding to the model extension SIR+T for serotype E18. The parameter change point is given in number of years after 2000.

Fig. S62.

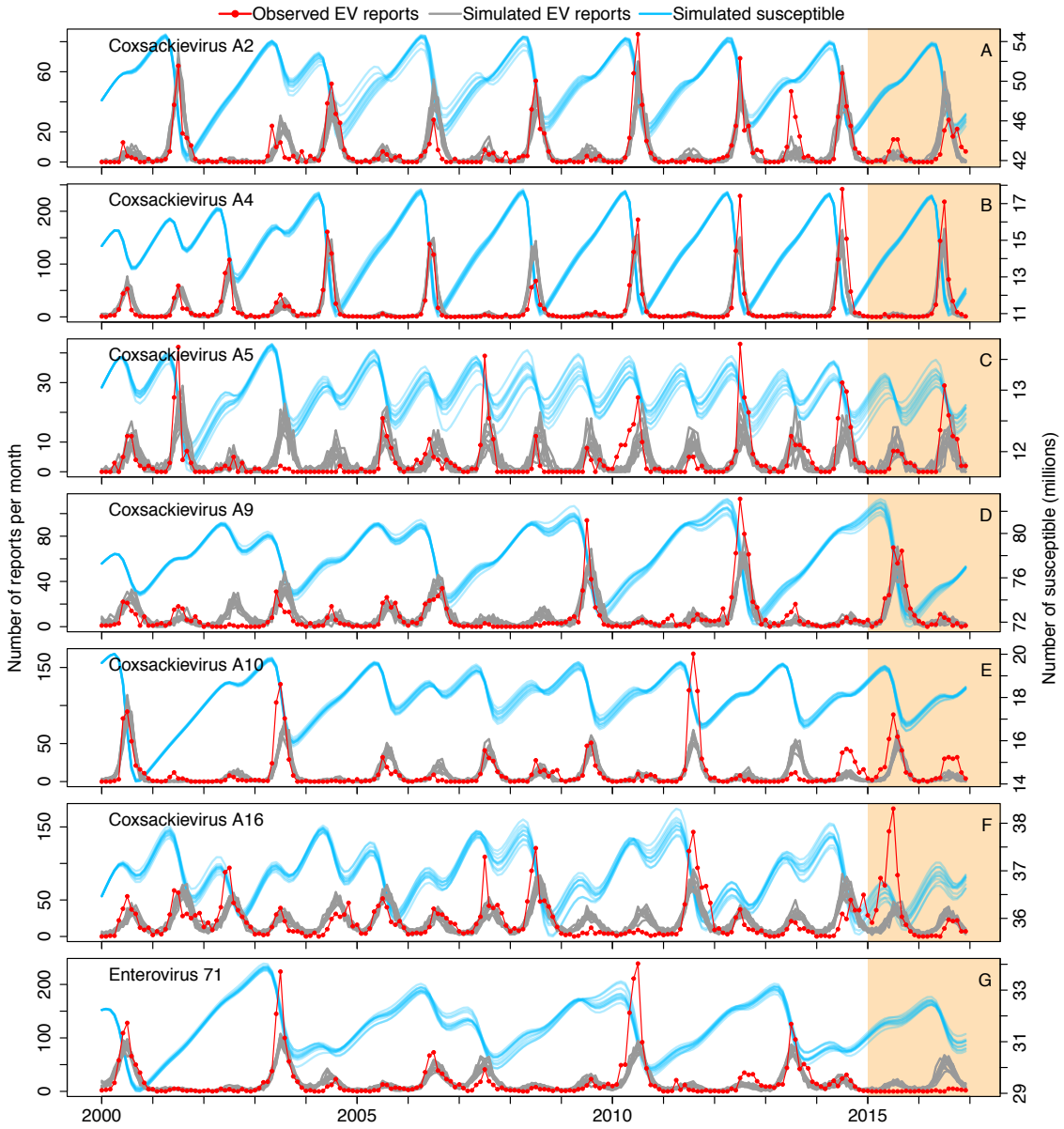

Fig. S62: Model with waning immunity (SIRS) fit to data for six Coxsackieviruses A and EV-A71. The reported number of monthly isolations (red line) and 10 best stochastic simulations of the model from initial conditions over 100 for the maximum likelihood estimates of the parameters (gray lines) are shown. The estimated number of susceptible individuals (blue) is shown in the right y-axis. The model was fitted to data for January 2000 to December 2014 (white background), and therefore, simulations for January 2015 to December 2016 (orange background) are out-of-sample predictions. Parameter values in Table S5.

Fig. S63.

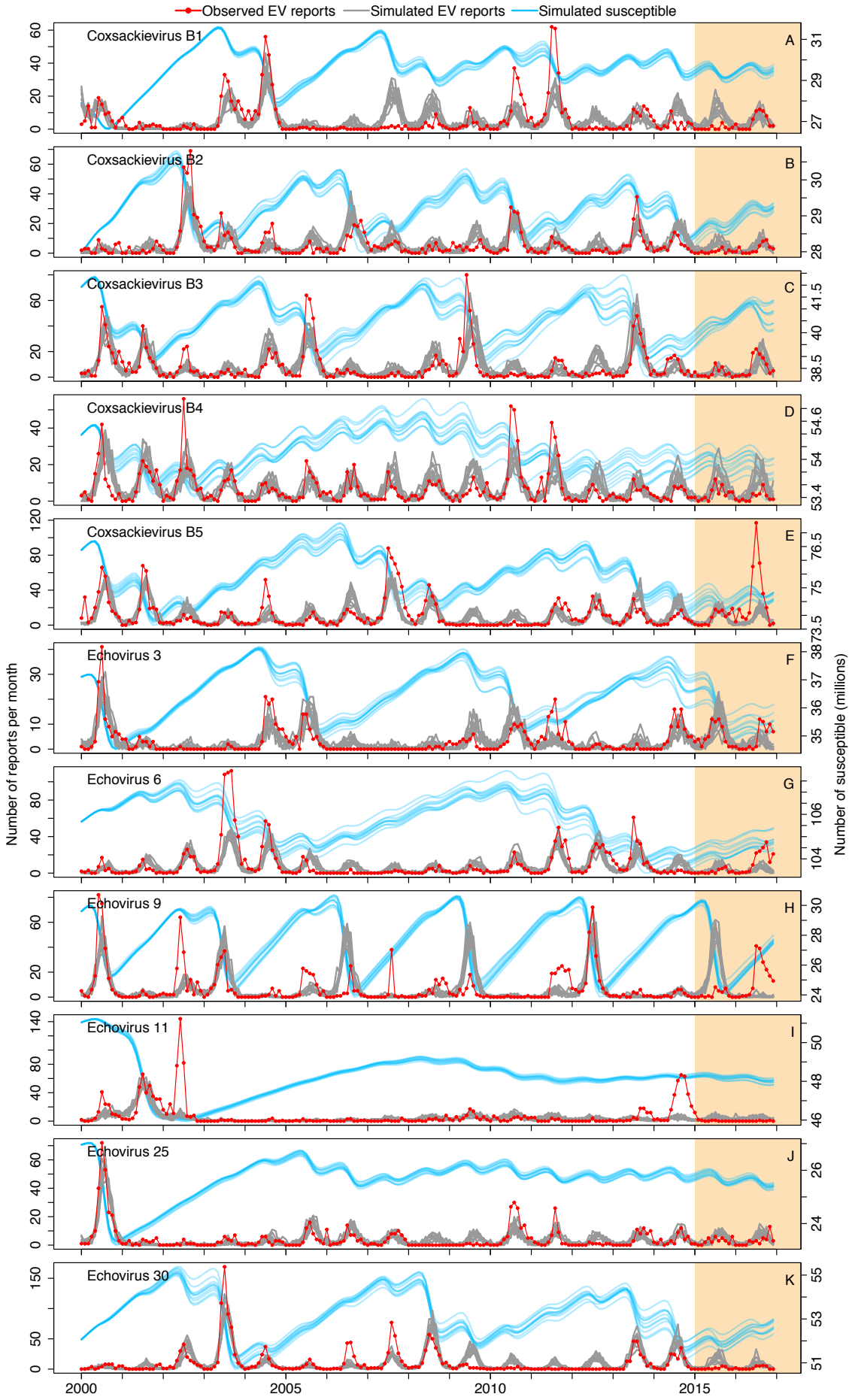

Fig. S63: Model with waning immunity (SIRS) fit to data for five Coxsackieviruses B and six Echoviruses. See details in Fig. S62. Parameter values in Table S5.

Table S1.

EV serotype		EV species	N. reports
CV-A6	Coxsackievirus A6	A	4178
CV-A16	Coxsackievirus A16	A	3766
EV-A71	Enterovirus 71	A	3607
CV-A4	Coxsackievirus A4	A	3140
E13	Echovirus 13	B	2178
CV-A10	Coxsackievirus A10	A	2009
CV-B5	Coxsackievirus B5	B	1997
E30	Echovirus 30	B	1812
E6	Echovirus 6	B	1652
CV-B3	Coxsackievirus B3	B	1484
CV-A9	Coxsackievirus A9	B	1444
E11	Echovirus 11	B	1408
CV-A2	Coxsackievirus A2	A	1403
CV-B4	Coxsackievirus B4	B	1274
E9	Echovirus 9	B	1267
E18	Echovirus 18	B	1255
CV-B2	Coxsackievirus B2	B	1076
CV-B1	Coxsackievirus B1	B	1020
E25	Echovirus 25	B	755
CV-A5	Coxsackievirus A5	A	720
E3	Echovirus 3	B	549
E7	Echovirus 7	B	523
CV-A8	Coxsackievirus A8	A	374
EV-D68	Enterovirus 68	D	280
E16	Echovirus 16	B	227
CV-A12	Coxsackievirus A12	A	148
E5	Echovirus 5	B	76
CV-A3	Coxsackievirus A3	A	71
E21	Echovirus 21	B	54
E14	Echovirus 14	B	41
CV-A24	Coxsackievirus A24	C	32
CV-A14	Coxsackievirus A14	A	31
E17	Echovirus 17	B	31
CV-A7	Coxsackievirus A7	A	29
CV-B6	Coxsackievirus B6	B	21
E19	Echovirus 19	B	21
CV-A21	Coxsackievirus A21	C	15
E4	Echovirus 4	B	12
E24	Echovirus 24	B	10
E12	Echovirus 12	B	8
CV-A1	Coxsackievirus A1	C	4
E1	Echovirus 1	B	4
E2	Echovirus 2	B	4
E27	Echovirus 27	B	4
E20	Echovirus 20	B	3
E33	Echovirus 33	B	2
NT	Unknown serotype		2645

Table S1: Total number of non-polio enterovirus isolations reported in Japan between January 2000 and December 2014 by serotype (descending order). All the serotypes with at least one reported isolation are shown. NT, not typed.

Table S2.

Serotype	β_m	β_s	ϕ	ω	ρ	s_0	i_0	R_0	log-lik
CV-A2	843	0.22	0.72	76	9.10E-05	0.0538	2.00E-06	16.2	-578
CV-A4	1706	0.25	0.70	92	1.94E-04	0.0254	1.48E-04	32.7	-745
CV-A5	835	0.19	0.68	51	4.50E-05	0.0559	3.50E-05	16	-550
CV-A6	1233	0.19	0.70	469	1.24E-04	0.0351	5.40E-05	23.6	-774
CV-A9	528	0.14	0.68	33	9.80E-05	0.0918	7.50E-05	10.1	-722
CV-A10	862	0.19	0.65	124	1.02E-04	0.0595	2.60E-05	16.5	-829
CV-A16	502	0.11	0.69	2	2.68E-04	0.0950	5.50E-05	9.6	-940
EV-A71	520	0.13	0.75	8	1.96E-04	0.0993	3.10E-05	10	-949
CV-B1	212	0.12	0.68	5	7.70E-05	0.2230	1.60E-04	4.1	-706
CV-B2	377	0.14	0.65	2	7.40E-05	0.1231	7.80E-05	7.2	-561
CV-B3	330	0.15	0.68	13	9.90E-05	0.1531	2.30E-05	6.3	-629
CV-B4	112	0.18	0.68	10	1.33E-04	0.4368	4.00E-05	2.1	-570
CV-B5	178	0.20	0.68	19	1.41E-04	0.2769	3.40E-05	3.4	-763
E3	240	0.16	0.68	11	4.30E-05	0.2046	1.15E-04	4.6	-388
E6	117	0.19	0.65	2	1.50E-04	0.4201	6.00E-06	2.2	-567
E9	787	0.13	0.72	23	7.30E-05	0.0662	2.80E-05	15.1	-726
E11	94	0.11	0.73	16	1.21E-04	0.5357	1.10E-05	1.8	-775
E18	578	0.16	0.71	3	5.60E-05	0.0849	2.90E-05	11.1	-189
E25	250	0.17	0.64	33	5.10E-05	0.2007	1.84E-04	4.8	-452
E30	210	0.21	0.71	15	1.24E-04	0.2258	3.00E-06	4	-779

Table S2: Model parameter estimates. Point estimates for each enterovirus serotype used for the simulations in Figs. 2 and 3 and Fig. S11 – Fig. S30. Parameter units for the average transmission rate, β_m, is year^{-1}.

Table S3.

Serotype	β_m	β_s	ω	ρ	s_0	i_0
CV-A2	797 – 917	0.21 – 0.27	26 – 81	9.70E-05 – 1.01E-04	0.0489 – 0.0561	5.00E-09[a] – 3.04E-06
CV-A4	1636 – 1801	0.22 – 0.28	96 – 126	1.80E-04 – 1.99E-04	0.0247 – 0.0263	8.57E-05 – 2.83E-04
CV-A5	680 – 849	0.20 – 0.27	20 – 80	4.50E-05 – 5.00E-05	0.0584 – 0.0734	1.00E-08[a] – 2.98E-05
CV-A6[b]	1045 – 1295	0.18 – 0.21	255 – 405	1.24E-04 – 1.33E-04	0.0336 – 0.0432	1.00E-06 – 7.06E-05
CV-A9	509 – 599	0.13 – 0.15	29 – 64	9.90E-05 – 1.06E-04	0.0802 – 0.0858	6.06E-05 – 8.40E-05
CV-A10	595 – 1000[a]	0.18 – 0.22	128 – 172	9.30E-05 – 1.01E-04	0.0634 – 0.0748	1.07E-05 – 6.73E-05
CV-A16	454 – 496	0.12 – 0.13	0 – 7	2.63E-04 – 2.70E-04	0.0953 – 0.101	4.20E-05 – 6.17E-05
EV-A71	496 – 520	0.13 – 0.15	1 – 11	NA – NA	0.0965 – 0.1021	3.63E-05 – 7.46E-05
CV-B1[c]	198 – 218	NA – NA	2 – 33	7.40E-05 – 8.40E-05	0.2229 – 0.2253	8.53E-05 – 1.38E-04
CV-B2	355 – 401	0.11 – 0.14	0 – 49	7.20E-05 – 7.70E-05	0.1147 – 0.1318	4.28E-05 – 9.67E-05
CV-B3[d]	317 – 352	0.13 – 0.16	4 – 33	9.90E-05 – 1.04E-04	0.1524 – 0.1552	2.17E-05 – 4.53E-05
CV-B4	101 – 166	0.15 – 0.18	0 – 74	1.12E-04 – 1.43E-04	0.2927 – 0.3933	3.23E-05 – 5.24E-05
CV-B5	181 – 216	0.16 – 0.18	NA – NA	1.53E-04 – 1.79E-04	NA – NA	5.00E-06[a] – 2.77E-04[a]
E3	235 – 268	0.16 – 0.19	7 – 22	3.80E-05 – 4.20E-05	0.1816 – 0.198	1.06E-04 – 2.03E-04
E6	120 – 137	0.15 – 0.20	NA – NA	1.32E-04 – 1.45E-04	0.3664 – 0.4214	2.60E-06 – 1.07E-05
E9	578 – 760	0.11 – 0.17	19 – 44	6.70E-05 – 7.60E-05	0.068 – 0.076	2.63E-05 – 5.69E-05
E11	90 – 106	NA – NA	NA – NA	1.09E-04 – 1.39E-04	NA – NA	NA – NA
E18[e]	175 – 600[a]	0.11 – 0.19[a]	0 – 59	5.50E-05 – 7.20E-05	0.1052 – 0.1706	1.00E-05[a] – 1.01E-04
E25	223 – 269	0.16 – 0.21	34 – 96	4.90E-05 – 5.30E-05	0.1638 – 0.2099	9.27E-05 – 5.02E-04
E30	194 – 248	0.2 – 0.22	14 – 28	1.19E-04 – 1.27E-04	0.1833 – 0.2426	1.79E-06 – 7.17E-06

Table S3: Approximate 99% confidence intervals of the parameters obtained with the profile log-likelihood. [a] Indicates above or below this value. [b] Confidence interval obtained by maximising the log-likelihood over the period Jan 2000 to Dec 2010 (instead of Jan 2000 to Dec 2014). [c] For this serotype, we fixed $\beta_m = 178$ and $\beta_s = 0.12$ to construct the profile likelihoods of ω, ρ, s_0 and i_0. [d] For this serotype, we fixed $\beta_m = 330$ to construct the profile likelihoods of β_s, ω, s_0 and i_0. [e] Confidence interval obtained by maximising the log-likelihood over the period Jan 2000 to Dec 2005 (instead of Jan 2000 to Dec 2014). NA indicates the profile could not be obtained: the maximisation of the log-likelihood for fixed values of the profiled parameter did not converge to a neighbourhood of the overall maximum log-likelihood. See the profile log-likelihoods in Fig. S35 – Fig. S54.

Table S4.

Serotype	Model	β_m	β_s	ϕ	ω	ρ	s_0	i_0	c_β	c_ρ	c_a	t_c	log-lik
CV-A6	SIR+P	1230	0.16	0.70	111	1.08E-04	0.0384	6.10E-06	–	5.10	–	2010.18	-1017
CV-A6	SIR+T	1476	0.15	0.70	428	1.05E-04	0.0308	4.99E-05	1.29	–	–	2010.58	-1423
CV-A6	SIR+A	2098	0.14	0.70	486	1.25E-04	0.0216	6.43E-05	–	–	0.0131	2011.45	-1447
E18	SIR+A	174	0.17	0.71	75	8.54E-05	0.2736	4.59E-05	–	–	0.0309	2005.64	-534
E18	SIR+T	170	0.16	0.71	101	8.31E-05	0.2788	5.30E-05	1.09	–	–	2005.72	-538
E18	SIR+P	274	0.16	0.71	10	5.42E-05	0.1749	5.88E-05	–	1.06	–	2006.24	-802

Table S4: Model parameter estimates for three extensions of the SIR model for Coxsackievirus A6 (CV-A6) and Echovirus 18 (E18) serotypes. These extensions include a change in transmissibility (SIR+T), pathogenicity (SIR+P), or antigenicity (SIR+A) at the time point t_c (estimated). For both serotypes, the models are ordered by decreasing log-likelihood.

Table S5.

Serotype	β_m	β_s	ϕ	ω	ρ	s_0	i_0	δ	δ^{-1}	R_0	log-lik
CV-A2	123	0.22	0.72	276	1.10E-05	0.3736	4.50E-05	8.99E-02	11.1	2.4	-587
CV-A4	388	0.26	0.70	510	4.40E-05	0.1134	3.51E-04	3.19E-02	31.4	7.4	-768
CV-A5	470	0.21	0.68	146	2.80E-05	0.1017	7.00E-06	5.13E-03	195.0	9	-564
CV-A9	79	0.14	0.68	4	1.60E-05	0.6065	6.97E-04	1.25E-01	8.0	1.5	-736
CV-A10	333	0.20	0.65	264	4.20E-05	0.1530	1.55E-04	1.65E-02	60.6	6.4	-897
CV-A16	168	0.12	0.69	1	9.20E-05	0.2858	1.41E-04	2.18E-02	45.8	3.2	-1047
EV-A71	196	0.11	0.75	8	8.20E-05	0.2534	2.92E-04	1.64E-02	61.1	3.8	-982
CV-B1	207	0.14	0.68	81	3.30E-05	0.2225	1.62E-03	1.21E-02	82.9	4	-723
CV-B2	212	0.14	0.65	14	4.50E-05	0.2193	7.50E-05	7.85E-03	127.4	4.1	-575
CV-B3	153	0.15	0.68	16	4.70E-05	0.3291	7.80E-05	1.48E-02	67.8	2.9	-642
CV-B4	114	0.16	0.68	15	1.15E-04	0.4281	5.50E-05	1.24E-03	809.2	2.2	-575
CV-B5	82	0.18	0.68	16	7.50E-05	0.6008	8.70E-05	2.14E-02	46.6	1.6	-811
E3	170	0.14	0.68	14	2.60E-05	0.2920	1.99E-04	5.91E-03	169.3	3.3	-395
E6	59	0.18	0.65	4	7.00E-05	0.8317	3.00E-05	4.84E-02	20.7	1.1	-680
E9	220	0.14	0.72	127	2.50E-05	0.2315	1.23E-04	2.41E-02	41.5	4.2	-755
E11	127	0.08	0.73	75	6.10E-05	0.4017	1.40E-05	9.10E-04	1099.3	2.4	-868
E25	238	0.16	0.64	65	4.90E-05	0.2122	1.65E-04	5.57E-04	1794.3	4.6	-453
E30	117	0.21	0.71	8	8.10E-05	0.4091	9.00E-06	1.27E-02	78.8	2.2	-839

Table S5: Parameter estimates for the model with waning immunity. Point estimates for each enterovirus serotype used for the simulations in Fig. S62 and Fig. S63. Parameter units for the average transmission rate, β_m, and the average rate of waning immunity, δ, is year^{-1}, and thus, duration of protective immunity, δ^{-1}, is given in years.